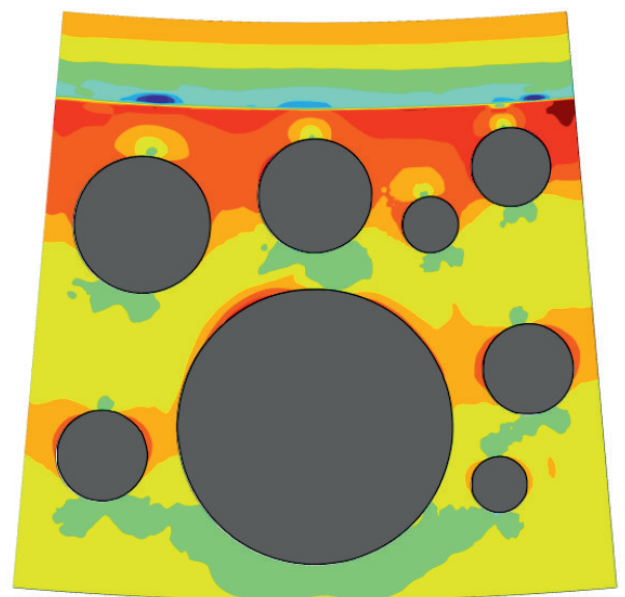
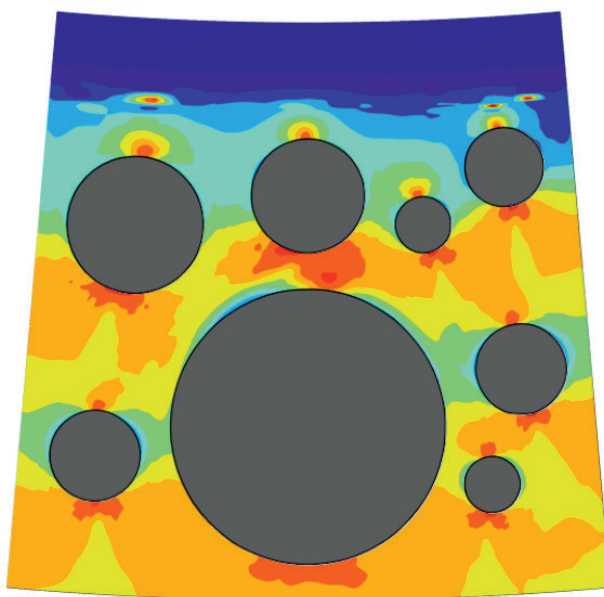




SFB 837  
Interaktionsmodelle für den  
maschinellen Tunnelbau

## Multi-physical simulations: transport and infiltration of suspensions in granular porous media

Alexander Schaufler



# Multi-physical simulations: transport and infiltration of suspensions in granular porous media

Dissertation  
zur  
Erlangung des Grades  
Doktor-Ingenieur

der  
Fakultät für Maschinenbau  
der Ruhr-Universität Bochum

**Alexander Schaufler**

aus Frunse

Bochum 2015



Dissertation eingereicht am: 22. Juli 2015

Tag der mündlichen Prüfung: 25. September 2015

Erster Referent: Prof. Dr.-Ing. Holger Steeb

Zweiter Referent: Prof. Dr.-Ing. Stefan Diebels

Dritter Referent: Prof. Dr.-Ing. Frank Wuttke

# Danksagung

Diese Arbeit entstand im Zeitraum April 2011 - Juli 2015 am Lehrstuhl für Kontinuumsmechanik an der Ruhr-Universität Bochum. In diesem Abschnitt möchte ich den zahlreichen Unterstützern dieser Arbeit danken.

Mein besonderer Dank gilt Prof. Dr.-Ing. Holger Steeb für die fortwährende Unterstützung, zahlreichen, stets positiven und konstruktiven wissenschaftlichen Diskussionen sowie das ein oder andere zusprechende Wort in schwierigen Passagen. Weiterhin bedanke ich mich für die motivierende Arbeitsweise und die wissenschaftliche Selbstverwirklichung, die ohne das mir entgegengebrachte Vertrauen nicht möglich gewesen wäre.

Ferner danke ich Prof. Dr.-Ing. Frank Wuttke und Prof. Dr.-Ing. Stefan Diebels für die Übernahme der Koreferate und das damit einhergehende wissenschaftliche Interesse an dieser Arbeit.

Ich danke der Deutschen Forschungsgemeinschaft für die finanzielle Unterstützung im Rahmen des Sonderforschungsbereiches 837 „Interaktionsmodelle im maschinellen Tunnelbau“ sowie den Mitarbeitern für die anregende Zusammenarbeit in diesem multidisziplinären Projekt. Ich bedanke mich bei Prof. Dr.-Ing. Tom Schanz für die interessanten Diskussionen.

Vielen weiteren Personen bin ich zu Dank verpflichtet. Insbesondere Dr.-Ing. Christian Becker für die Geduld und den Zuspruch in allen Lebenslagen und die zahlreichen Diskussionen. Dr.-Ing. Alexander Scheuermann danke ich für das Aufzeigen alternativer Blickwinkel und den konstruktiven und hilfreichen Dialog im Rahmen des Forschungsaustauschs mit „The University of Queensland, Australia“. Dr.-Ing. Carlo Vinci danke ich für die kollegiale Zusammenarbeit und die freundschaftliche Unterstützung insbesondere innerhalb der finalen Phase dieser Arbeit.

Weiterhin bedanke ich mich bei allen Mitarbeitern vom Lehrstuhl für Kontinuumsmechanik für eine angenehme Arbeitsatmosphäre innerhalb der letzten vier Jahre sowie deren Kollegialität und Hilfsbereitschaft.

Ich bedanke mich bei meiner Familie und meinen Freunden für die Unterstützung, die Motivation und das Verständnis. Insbesondere danke ich Arne Dittmer, M.Sc. für das Korrekturlesen dieser Arbeit.

Ein besonderer Dank gilt meiner Verlobten Dr. rer. nat. Larissa Schwertmann für die fortwährende Unterstützung, die liebevolle Ermutigung sowie das lebensfrohe Wesen.



# Abstract

In this work the numerical modelling of the annular gap grouting process in the field of mechanized tunnelling is investigated. The occurrence of the annular gap is a result of an overcut and the conicity of the tunnel boring machine. Hence, the outer diameter of the tunnel boring machine is larger than the diameter of the actual tunnel lining.

The aim of the annular gap grouting is a complete filling of the annular gap in order to achieve a stable and secure bedding of the tunnel lining. This is realized by prescribing a defined stress-state of the annular gap grouting mortar and the surrounding soil in the shortest possible time period, in order to minimize surface settlements. Based on the framework in the field of continuum mechanics, the Theory of Porous Media is used to describe the physics of this process. In detail, the infiltration process is investigated by the evaluation of the governing partial local balance equations.

Special attention is paid to the constitutive assumptions for the infiltration process and for the description of solid deformations. Infiltration is defined as the phase transition of suspended particles in the pore fluid to particles, which are attached to the solid skeleton. Due to the continuum mechanical approach, the micro structure of the considered volume is reduced to a finite number of constituents, which are described by their volume fractions with respect to the total volume. In order to represent the ongoing physics of the volume within the homogenized framework of the Theory of Porous Media on the micro scale, the field equations are coupled with a statistical analysis of the micro structure.

Furthermore, the consolidation of a porous medium (e.g. gap grouting mortar) in the backfilled volume is investigated. From the evaluation of the consolidation process the evolution of the material stiffness within the grouting process is characterized. The numerical approaches presented in this thesis, are applicable for the simulation of interface phenomena, e.g. the formation of a filter cake. Analysis and numerical investigation of the phenomena, which occur during the grouting process of the annular gap in granular soil, lead to a deeper understanding of the ongoing physics. Therefore, the presented numerical approaches establish the basis for a more accurate grouting process in the field of mechanized tunnelling.



# Kurzfassung

In dieser Dissertation wird die numerische Modellierung des Verfüllvorgangs eines Ringspaltes mit Ringspaltmörtel im Bereich des maschinellen Tunnelbaus untersucht. Die Entstehung des Ringspaltes ist auf einen Überschnitt sowie auf die Konizität der Tunnelbohrmaschine zurückzuführen. Demnach ist der Außendurchmesser der Tunnelbohrmaschine stets wenige Zentimeter größer als der tatsächliche Durchmesser des folgenden Tunnelausbaus.

Ziel der Ringspaltverpressung ist eine vollständige Verfüllung des Ringspaltes und eine sichere und stabile Bettung der Tunnelröhre. Dies wird durch die Einstellung eines definierten Spannungszustandes im Ringspalt sowie im daran anstehenden Boden in einer möglichst kurzen Zeitspanne erreicht, wodurch Oberflächensetzungen minimiert werden können. Ausgehend von dem Arbeitsbereich der Kontinuumsmechanik, wird zur Beschreibung der vorherrschenden Prozesse die Theorie Poröser Medien verwendet. Hierbei kann der Infiltrationsprozess durch die Auswertung partieller lokaler Bilanzgleichungen beschrieben werden. Besondere Aufmerksamkeit wird dabei auf die Konstitutivannahmen für den Infiltrationsprozess sowie die Beschreibung der Festkörperdeformationen gelegt. Als Infiltration versteht man dabei die Phasentransformation von dem fluidisierten Feinkorn der liquiden Phase zu einem Feinkorn, welches an dem Porenskelett anhaftet. Aufgrund der kontinuumsmechanischen Betrachtungsweise, wird die Mikrostruktur auf eine endliche Anzahl einzelner Konstituierenden reduziert, welche durch ihren Anteil am Gesamtvolumen beschrieben werden. Damit, trotz des Homogenisierungsvorgangs, das Verhalten des betrachteten Volumenelementes auf der Mikroskala dargestellt werden kann, werden die Feldgleichungen mit einer statistischen Auswertung der Mikrostruktur gekoppelt.

Darüber hinaus wird die Konsolidierung des porösen Mediums (z.B. Ringspaltmörtel) in dem verfüllten Volumen betrachtet. Aus der Auswertung des Konsolidationsprozesses kann die Evolution der Steifigkeit des Materials im Verlauf des Verfüllprozesses gewonnen werden. Die hier präsentierten Berechnungsmodelle sind damit für die Beschreibung von Grenzsichtphänomenen, wie die Entstehung eines Filterkuchens, geeignet. Die Erfassung und numerische Abbildung der natürlichen Prozesse, welche bei der Verfüllung von Ringspaltmörtel im Lockergestein auftreten, führt zu einem tiefgehenden Verständnis der ablaufenden physikalischen Phänomene. Dies kann für eine präzisere Steuerung des Verfüllvorgangs von Ringspaltmörtel im maschinellen Tunnelbau genutzt werden.



# Contents

<b>List of Figures</b>	<b>V</b>
<b>1 Introduction and Motivation</b>	<b>1</b>
1.1 Scope and outline . . . . .	2
<b>2 Mechanized tunnelling</b>	<b>5</b>
2.1 Development of mechanized tunnelling techniques . . . . .	5
2.2 Annular gap grouting . . . . .	8
2.2.1 Discontinuous annular gap grouting . . . . .	9
2.2.2 Continuous annular gap grouting . . . . .	10
2.2.3 Further technical facilities for annular gap grouting . . . . .	10
2.2.4 Grouting material . . . . .	12
2.2.5 State of the art . . . . .	13
<b>3 Theoretical background of modelling hydro-mechanical coupled processes</b>	<b>15</b>
3.1 Mixture Theory . . . . .	15
3.2 Theory of Porous Media . . . . .	16
3.2.1 Introductory definitions . . . . .	16
3.2.2 Kinematics in the Theory of Porous Media . . . . .	17
3.3 Balance equations . . . . .	21
3.3.1 Balance of mass . . . . .	22
3.3.2 Balance of momentum . . . . .	23
3.3.3 Balance of moment of momentum . . . . .	24
3.3.4 Balance of energy . . . . .	25
3.3.5 Balance of entropy . . . . .	26
3.4 Linearisation . . . . .	27
3.5 Constitutive modelling . . . . .	28
3.5.1 Concept of effective stress . . . . .	29
3.5.2 Linear elastic solid skeleton . . . . .	30
3.5.3 Plastic deformations of the solid skeleton . . . . .	30
3.5.4 Darcy's filter law . . . . .	34
3.6 Numerical realization . . . . .	35

<b>4</b>	<b>Infiltration processes in cohesionless soils</b>	<b>39</b>
4.1	Introduction . . . . .	39
4.2	Governing equations of infiltration processes . . . . .	41
4.2.1	Mass balances . . . . .	44
4.3	Constitutive equation for mass exchange . . . . .	47
4.4	Analysis of a 1-dim infiltration problem . . . . .	48
4.5	Summary . . . . .	52
<b>5</b>	<b>Transport and infiltration of suspensions through porous media</b>	<b>53</b>
5.1	Introduction . . . . .	54
5.2	CSD-Analysis . . . . .	55
5.2.1	State of the Art . . . . .	56
5.2.2	Statistical evaluation of the constriction size distribution . . . . .	57
5.2.3	Validation of statistical approach . . . . .	59
5.3	Multi-phase FEM approach to describe infiltration phenomena . . . . .	61
5.3.1	Governing equations of extended continuum model . . . . .	61
5.3.2	Initial Boundary Value Problem (IBVP) for Infiltration processes . . . . .	65
5.3.3	Analytical solution for a simplified hydraulic IBVP . . . . .	66
5.3.4	Example: comparison of analytical and numerical solution . . . . .	68
5.4	Evolution of morphologic properties . . . . .	68
5.4.1	Numerical realization . . . . .	68
5.4.2	Numerical example for evolution of morphological properties . . . . .	70
5.4.3	Numerical example of a 2-dim heterogeneous domain . . . . .	72
5.5	Discussion . . . . .	74
5.6	Summary . . . . .	78
<b>6</b>	<b>Hydro-mechanical simulations of the annular gap grouting process in mechanized tunnelling</b>	<b>79</b>
6.1	Introduction . . . . .	79
6.1.1	Suspension flow through porous media . . . . .	79
6.2	Continuum mechanical framework of modelling hydro-mechanical coupling in porous media . . . . .	83
6.2.1	Kinematics . . . . .	83
6.2.2	Balance equations . . . . .	84
6.2.3	Constitutive formulation . . . . .	85
6.2.4	Extension to soil-plasticity . . . . .	88
6.2.5	Boundary Value Problem considering infiltration and deformation of the solid skeleton . . . . .	89
6.2.6	Numerical implementation . . . . .	90
6.3	Validation of the numerical model . . . . .	91
6.3.1	Mechanical part: validation of the approach using Terzaghi's problem . . . . .	91
6.3.2	Hydraulic part: validation with a 0-dim example for infiltration . . . . .	93

---

6.3.3	Validation of the plastic formulation . . . . .	94
6.4	Numerical results . . . . .	98
6.4.1	Evolution of mechanical and hydraulic properties in a cross section of a tunnel lining . . . . .	98
6.5	Discussion . . . . .	103
6.6	Conclusion . . . . .	106
<b>7</b>	<b>Concluding remarks</b>	<b>107</b>
7.1	Discussion and conclusion . . . . .	107
	<b>Bibliography</b>	<b>111</b>
	<b>Curriculum Vitae</b>	<b>121</b>



# List of Figures

2.1	Longitudinal section of a Mix-shield TBM. . . . .	6
2.2	Earth Pressure Balance (EPB) shield TBM used in London. . . . .	8
2.3	Longitudinal section of the tail skin and the segmental lining. . . . .	10
3.1	Kinematics of a multi-phase continuum. . . . .	18
3.2	Yield surface according to Mohr-Coulomb and Drucker-Prager criterion. . . . .	33
4.1	Microscale and RVE of a fully-saturated soil and the corresponding four-phase continuum model. . . . .	41
4.2	Infiltration process: a) initial and boundary conditions for the investigated domain; b) illustration of the concentration profile for $t > t_0$ . . . . .	48
4.3	Contour plot describing the evolution of the porosity in space and time in the domain. . . . .	49
4.4	Distribution of the concentration $c_{eq}$ at equilibrium. . . . .	50
4.5	Formation of a filter cake. Left: external filter cake; right: internal filter cake . . . . .	51
5.1	Visualization of two possible pore constrictions. . . . .	56
5.2	Comparison of all possible constellations resulting from permutation of $f$ fractions (cf. Schuler [75]) with the number of physical unique constellations. . . . .	58
5.3	Comparison of the CSD using the proposed method with the CSD achieved by DEM simulations from Reboul et al. [68]. . . . .	60
5.4	Extended homogenization technique. . . . .	61
5.5	Illustration of the 0-dim IBVP and the used boundary and initial conditions. . . . .	69
5.6	Comparison of the numerical and analytical solution for a 0-dim infiltration IBVP. . . . .	70
5.7	Definition of the probability of infiltration considering geometrical restrictions. . . . .	71
5.8	Defined cases in order to perform benchmark calculations. For all cases filter stability of the solid is assumed. . . . .	72

5.9	Evolution of porosity due to different micro structures. the description of the single cases is given in Figure 5.8. . . . .	73
5.10	Evolution of the intrinsic permeability as a result of the 2-dim calculation for different times. . . . .	75
5.11	Visualization of the computed 2-dim IBVP. . . . .	76
5.12	Evolution of the morphology, here described by the GSD and CSD, induced by infiltration of a suspension in two different points of the domain in Figure 5.11. . . . .	77
6.1	Details of numerical implementation of plastic behaviour of the solid skeleton and its stiffening due to infiltration. . . . .	82
6.2	Fully saturated RVE representing a soil material, its homogenization within the TPM, as a four-constituent approach, and the two-constituent approach. . . . .	83
6.3	Illustration of the 1-dim IBVP and used boundary and initial conditions. . . . .	92
6.4	Comparison of the analytical and the numerical solution of Terzaghi's consolidation problem. . . . .	93
6.5	IBVP containing initial and boundary conditions for the simulation of 0-dim infiltration. . . . .	94
6.6	Numerical and analytical solution for the time depended evolution of porosity of the 0-dim infiltration approach. . . . .	95
6.7	Boundary Value Problem (expansion of a cylindrical tube) to compare the numerical approach with an analytical solution in case of ideal plastic yield function using Tresca criterion. . . . .	95
6.8	Distribution of the radial stress component $T_{rr}$ in case of different loading conditions for the numerical and the analytical approach. . . . .	97
6.9	Distribution of the circumferential stress component $T_{\theta\theta}$ in case of different loading conditions for the numerical and the analytical approach. . . . .	98
6.10	From the application to a numerical IBVP. Homogenization and boundary conditions for the IBVP. . . . .	99
6.11	Distribution of the intrinsic permeability for the last time step of the simulation along the $\mathbf{e}_1$ direction, cf. Figure 6.10. The definition of the corresponding cases is given in Table 6.3. . . . .	102
6.12	Distribution of the displacement of the porous skeleton at a point on the interface of the grout and solid domain for different cases defined in Table 6.3. . . . .	102
6.13	Evolution of the shear-modulus and the intrinsic permeability during backfilling of the annular gap in heterogeneous domain with impermeable inclusions. . . . .	104

# Chapter 1

## Introduction and Motivation

The modern society is characterized by the trend of an increasing population around the world. Additionally, the growth is overrepresented in some few chief cities around the world, the so-called metropolises, that are attracting inhabitants from the whole region by the advantages of the infrastructure of a modern city. However, this expansion leads to a high demand in extending the existing infrastructure to ensure a smooth everyday life of the population. One of the most elegant, because minimally invasive, ways to manage this is represented by the technique of mechanized tunnelling. The idea of the mechanized tunnelling technique is that the tunnel is created with a Tunnel Boring Machine (TBM), used to excavate a tunnel and to create the lining simultaneously. Theoretically, only two sites are demanded at the surface, one at the entrance of the TBM and one at the exit. Practically, the distance of the TBM is limited due to the supply of the TBM with resources like grouting material, tubings, and the transport of the excavated soil at the surface. However, the surface above the tunnel route does not have to be opened completely, which results in advantages for the every days life of the inhabitants in populated areas and additionally leads to the possibility for tunnelling projects in areas with an existing infrastructure at the ground surface. During the tunnelling process using the mechanized tunnelling technique in soft soil (e.g. sand, clay) an annular gap between the tunnel lining and the surrounding soil is created, which has to be instantaneously filled. For this, different types of grouting materials were developed. In literature many synonyms for the filling process are used. Without the claim to completeness those are: backfilling of the annular gap [65], tail void grouting [77], annular gap grouting [96], grouting of the shield tail gap [2].

It will be shown that many phenomena which occur during the grouting process, are not fully understood. Despite many successful tunnelling projects have been carried out in the past, some of which under very challenging conditions, a lot of potential within the grouting process is unused.

In order to gain insight in the ongoing physics of the grouting process of the annular gap in mechanized tunnelling, the dominating processes are identified and

simulated using newly developed numerical models. The development of a sophisticated multi-field formulation to describe the backfilling process will allow to study micro-scale phenomena. The dominating process, which leads to an evolution of the physical properties of a cement-free annular gap grouting mortar, is the infiltration of particles of the suspension into the solid skeleton of the mortar in the annular gap or the surrounding soil. An adequate numerical treatment of this phenomenon is crucial for the overall process. For this, the Theory of Porous Media will be used, which is a continuum modelling approach capturing multi-physical problems. The considered simulation domain is divided into volume fractions and the partial balance equations of individual constituents or combinations of constituents are used to derive field equations, which are solved numerically using the Finite Element Method (FEM). Hence, the field equations are transformed from their strong forms into weak forms, the simulation domain is discretized with respect to space and time and the resulting equations are solved using iterative tools like the Newton-Raphson algorithm. Due to the fact that microscopic effects are dominating the physics of the ongoing processes, the TPM is combined with a micro-structural investigation of the morphology of the granular porous medium. From standard geotechnical characterization methods, the so-called Grain Size Distributions (GSDs) of the considered soil and mortar are well-defined physical properties. Thus, the evolution of the morphology of the granular media is based on the GSD of the surrounding soil of the tunnel lining and the GSD of the backfilled annular gap grouting mortar. The physical quantity determining the physics with respect to morphology is the Constriction Size Distribution (CSD), which is calculated using statistical methods. The implementation of the statistical analysis of the micro structure within a multi-field continuum approach derived from the TPM allows an in-depth simulation of the hydraulic properties. For the evolution of mechanical properties the backfilling of annular gap will be interpreted as a consolidation process where additional localized stiffening may occur.

Note, that the term *infiltration* has a particular meaning in this thesis. If a volume which consists of a granular porous medium and is fully saturated with a pore fluid (e.g. a mixture of sandy-type soil and water) is considered, then *infiltration* describes the attachment of fine suspended particles which are penetrating with the pore fluid to the granular porous skeleton. In different scientific fields similar terms are denoting similar, but different processes. In hydrology the term *filtration* is used to describe the transport of a fluid (water) into soil, developing a partly-saturated vadose zone [64]. Therefore, in this work those processes are differentiated by the terms *infiltration* for the first, and *penetration* or *transport* for the latter case.

## 1.1 Scope and outline

This work is dedicated to create a deeper understanding of the grouting process in order to be able to simplify the grouting procedure and to ensure the fulfilment of all requirements of the backfilling process. The aim of this work is to develop numerical approaches for infiltration and transport phenomena applicable to geo-

technical problems, in particular capturing the ongoing processes of the backfilling of the annular gap during mechanized tunnelling operations.

For this, numerical modelling approaches are presented with different complexities. The main framework of the modelling approaches is given by the Theory of Porous Media (TPM), allowing to simulate the ongoing process with a multi-field and multi-phase continuum-based formulation. This different hierarchies of numerical approaches, presented in the following, allow to gain a better insight in the grouting process. This work is structured as follows:

- In Chapter 2 the mechanized tunnelling technique is introduced in general. After the discussion of necessities and the advantages and disadvantages of the mechanized tunnelling techniques, the chapter focusses on the annular gap backfilling process. The process itself as also the required technical facilities are described. Additionally, a literature overview about the grouting process and its numerical simulation is presented.
- Chapter 3 describes the TPM as the numerical framework of the modelling approach. First, general assumptions are given, which are used in this thesis. After this, the kinematics of a multi-phase material are discussed. Following, the global partial balance relations balancing mass, momentum, moment of momentum, energy, and entropy are introduced axiomatically. The partial local balance relations of multi-phase material are derived from the global relations.
- The equations obtained from the TPM are used to create a multi-field approach capturing infiltration and transport phenomena in Chapter 4. A constitutive assumption for the mass exchange is presented and 1-dim numerical examples are studied. The findings gain a better insight in infiltration phenomena, especially on the formation of the filter cake.
- The introduction of the concept of *species* within the multi-field formulation is presented in Chapter 5. This extension leads to the possibility of capturing the evolution of the microstructure of the porous domain within the continuum-based formulation. Furthermore, an analytical solution is presented for a special case of infiltration problems. Numerical examples are conducted in order to describe the evolution of hydraulic properties of a heterogeneous 2-dim domain.
- In Chapter 6 a hydro-mechanical coupling is established to simulate the evolution of deformations of the solid skeleton in addition to the hydraulic properties. Thus, stiffening of the porous skeleton and plastic deformations are considered. The mechanical extension of the infiltration modelling approach allows a more detailed simulation of settlements induced by the annular gap filling process. Furthermore, the phenomena of individual simulation features of the proposed model are discussed with respect to their importance for the backfilling process in mechanized tunnelling.

- Chapter 7 summarizes the results of this work. The different modelling approaches which are used in this thesis are linked and compared to each other. The impact of the created modelling approaches on the backfilling process is discussed and further possible working fields are highlighted.

Note that parts of this contribution are already published or will be published soon in international peer-reviewed journals. The results of Chapter 4 are published in the *Journal of Applied Mathematics and Mechanics* [71]. Chapter 5 is the basis of a publication that has been submitted to the *International Journal for Numerical and Analytical Methods in Geomechanics* and the results of Chapter 6 will be soon submitted to the international journal *Computers and Geotechnics*.

## Chapter 2

# Mechanized tunnelling

*In this chapter the mechanized tunnelling technique is discussed. The general processes during tunnelling are presented, with a focus on the annular gap grouting procedure. The necessity of gap grouting is discussed. After that the technical facilities for the grouting procedure are described. In the last part of the chapter an literature overview about numerical methods for annular gap grouting in mechanized tunnelling is given.*

### 2.1 Development of mechanized tunnelling techniques

There are several types of methods to create a tunnel. Conventional methods are summarized by the cut-and-cover method, in which a tunnel is created by opening the surface, creating the tunnel lining and closing the surface in a way that the load of the scheduled projects at the surface does not impair the created tunnel. Conventional tunnelling techniques therefore come along with a high disturbance of everyday life at the surface.

To prevent this, the mechanized tunnelling technique was developed. Here, the tunnel is created by a Tunnel Boring Machine (TBM). Several types of TBMs exist but the basic process is, however, similar for all TBMs. In case of Mix-shield machines (Figure 2.1) the structure is as follows: in the front of the machine the cutter head with a circular cross section is situated, which creates the tunnel by excavation of the soil. Therefore, the part directly behind the cutter head is divided into two chambers. The excavated soil enters the excavation chamber which is fully filled with a mixture of water and bentonite as support fluid in order to balance the earth pressure to prevent a collapse of the working face. The pressure in the excavation chamber has to be well controlled to compensate the pressure loss resulting from material flux of the excavated soil out of the chamber by a screw conveyor, and to be able to react on different stress conditions of the soil at any time. Thus, the excavation chamber is directly connected to the pressure chamber at the bottom of the TBM. Only half of the pressure chamber is filled with the support fluid, while the upper part is filled

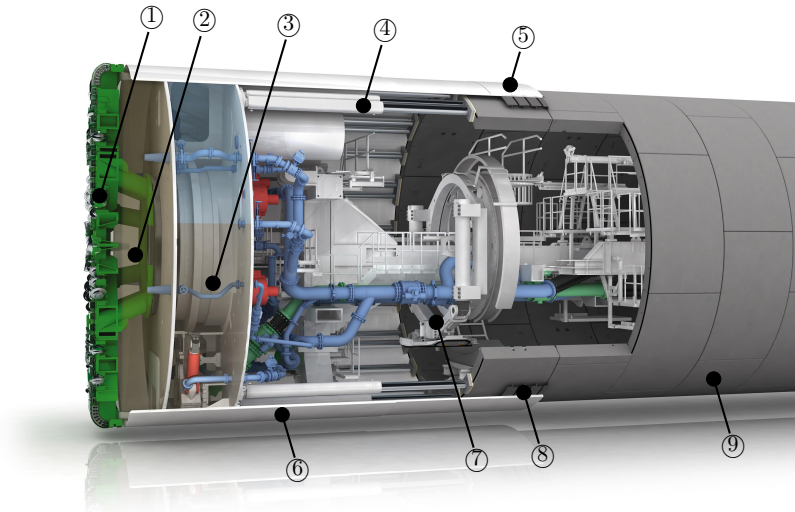


Figure 2.1: Longitudinal section of a Mix-shield TBM, with: ①: cutter head, ②: excavation chamber, ③: pressure chamber, ④: hydraulic jacks, ⑤: tail skin, ⑥: shield, ⑦: tubbing erector, ⑧: brush sealing, ⑨: tunnel lining. (Copyright: [www.herrenknecht.com](http://www.herrenknecht.com))

with gas, to adjust the pressure. The compressibility of the pressurized gas ensures a continuous face support without unwanted rapid changes in the supporting pressure. The excavated soil is continuously transported out of the excavation chamber, while the loss of the support fluid is replaced in order to keep a constant support pressure acting on the soil. The shield of the TBM covers the machine and supports the surrounding soil to prevent a collapse of it. In the back part of the machine the tunnel lining is created under the protection of the shield of the TBM. For this, single tubbing elements are placed by the erector in their final position and fixed to each other. Directly after the ring build the gap has to be filled completely with annular gap mortar from grout supply lines in the tail skin or through grout holes in the tubbings. The TBM-shield is sealed with wire brushes to prevent pore fluid of the soil or mortar from penetrating into the TBM. The advance of the TBM is driven by the hydraulic jacks which are supported by the last ring of the tunnel lining.

In Figure 2.2 a so-called Earth Pressure Balance (EPB) shield machine is shown. This is an especially economical way of mechanized tunnelling which can be applied in sandy-type granular sub-soil. The face support is realized using the excavated soil itself, which is preconditioned by mixing with a tenside foam [7].

In general advantages and disadvantages of mechanized tunnelling were summarized by Maindl *et al.* [58] as follows.

Advantages:

- high speed of excavation,
- profile accuracy,
- smallest possible disturbance of existing buildings at the surface,
- high security for staff,
- environmental friendly construction, low noise,
- high quality and economically tunnel lining.

Disadvantages:

- long planing phase, development and production of the TBM,
- long training periods for staff,
- consuming and costly site equipment, economic depreciation only for longer tunnels possible,
- risks resulting from variety in soil properties,
- restriction to a circular cross section of the lining,
- high effort in case of change of a cross section,
- forces of the jacks have to be encountered during design of the tunnel lining.

Despite the negative aspects, the mechanized tunnelling technology is often the key to extend an already existing infrastructure. The application of tunnelling of man-made tunnels is situated in all kind of transport system, i.e., roads, rail transport, transport of drinking water and sewage through pipes, *etc.*

As mentioned above, the main advantages of the mechanized tunnelling technique are obtained for projects in densely populated areas. There, one crucial fact for the realization of tunnelling projects is its acceptance among the affected population. Therefore, the visible impact of the tunnelling project has to be minimized. Apart from the visible site equipment outside the tunnel those are mainly the surface settlements induced by the tunnelling process above the tunnel lining. There are a plenty of reasons for tunnelling induced surface settlements, which sometimes even result in heaving. The main causes for surface displacements can be traced back to a poor pressure balance at the working face (e.g. too fast tunnel advance, wrong type of face support), which causes displacements of the surface directly in front of the TBM or a poor filling of the annular gap, which causes displacements directly above of the back part of the machine. This work is focussed on the numerical description of the annular gap grouting process.



Figure 2.2: Earth Pressure Balance (EPB) shield TBM used in London. The diameter of the cutter head is 4.7 m. (Copyright: [www.herrenknecht.com](http://www.herrenknecht.com))

## 2.2 Annular gap grouting

Due to technical restrictions, the cutting wheel of a TBM has to be a few cm larger than the tunnel lining, which is created directly after the excavation process. During the excavation procedure and the ring build, the surrounding soil is supported by the TBM to prevent settlements of the ground surface above the tunnel. The overcut results in a gap between the tunnel lining and the surrounding soil, the so-called annular gap. The annular gap has to be filled directly after finishing a lining segment, usually with a complex fluid, i.e. an annular gap grouting mortar. The aim of the grouting procedure is to recover the primary stress state of the surrounding soil and to establish a non-positive connection of the tunnel lining, in order to minimize settlements. Furthermore, a buoyancy of the tunnel lining has to be prevented.

During the grouting process two different cases can occur, which demand different numerical treatment to simulate the ongoing physical processes, namely a continuous and a discontinuous grouting. For a continuous grouting, the annular gap is already fully filled with grouting mortar. The continuous grouting can be used to de-water the grout mortar. In this case the de-watering process of the annular grouting mortar ensures the evolution of mechanical and hydraulic properties to fulfil the aims formulated above. This ensures a direct fully filled annular gap. The second strategy of gap grouting is using a discontinuous filling method. In this case the injection and the filling of the annular gap can not be neglected and thus, this process has to be modelled using a free surface to describe the boundary between the gas and the mortar phase. However, state of the art is the continuous grouting. Therefore, the following numerical approach is focussed on this case.

An important criterion to evaluate the quality of the annular gap grouting is the pressure distribution around the tunnel lining during and after the excavation

procedure. For this, pressure sensors have been applied to single tubbing segments on some reference tunnelling projects, thus the evolution of the pressure distribution during excavation and grouting can be analysed [35, 39, 54].

In general, a grouting mortar has to fulfil contrary requirements during different phases of the process. Before the actual grouting has started, the grouting mortar has to be transported using pipes. Therefore, a good flowability and pumpability of the mortar, coming along with a low shear-viscosity, are crucial properties. Directly after the filling process, stable bedding of the tunnel lining is necessary. For this, a fast increase in stiffness of the mortar is needed. As a requirement, a shear stiffness of the mortar, which corresponds at least to the shear stiffness of the surrounding soil, has to be achieved [91]. In this case, recovering of the primary stress state of the soil around tunnel lining can be achieved [2].

From a technical point of view, several possibilities of annular gap grouting techniques are possible. After the development of TBM's, mostly cement-contained grouting mortars have been used. This class of grouting mortar has certain advantages in stiffness evolution, which can be traced back to the hydration process. The disadvantage of cement-contained grouting mortars is obvious in case of a standstill of the TBM. The pipes of the grouting mortar can be clogged by the hydrated mortar itself. Therefore, costly maintenance of the system is required. Having this issue in mind, cement-free mortars were developed for the grouting process, which are characterized by the missing hydration of the material. This leads to a good workability and especially pump-ability for a larger duration of those materials [96, 97]. Due to the missing hydration, the evolution of shear stiffness of the grouting mortar is achieved by de-watering of the mortar, which can be interpreted as a consolidation process. To this purpose, the grouting takes place at a constant grouting pressure. After filling the annular gap completely, the grouting pressure is kept constant for a certain time. The pressure gradient, caused by the grouting process, induces a convective transport of the pore fluid of the mortar into the surrounding soil (de-watering). Hence, the pore space of the mortar is reduced and the particle contacts and the coordination number of each particle is increased. This leads to an increase of the shear stiffness of the grouting mortar. Therefore, a proper composition of the mortar leads to the desired shear stress after consolidation.

### 2.2.1 Discontinuous annular gap grouting

In case of discontinuous annular gap grouting, the ring is constructed at first, cf. Figure 2.3 (top). After one segment of the lining is fully built, the annular gap mortar is injected through tubes via grout holes in the tubbings of the lining. These holes contain a valve to retain the gap grouting material in the annular gap. The shield is sealed in the direction of the lining and also in the direction of the surrounding soil to keep the grouting material in the annular gap [96]. Due to the discontinuous process the surrounding soil of the tunnel lining remains without support for a short time.

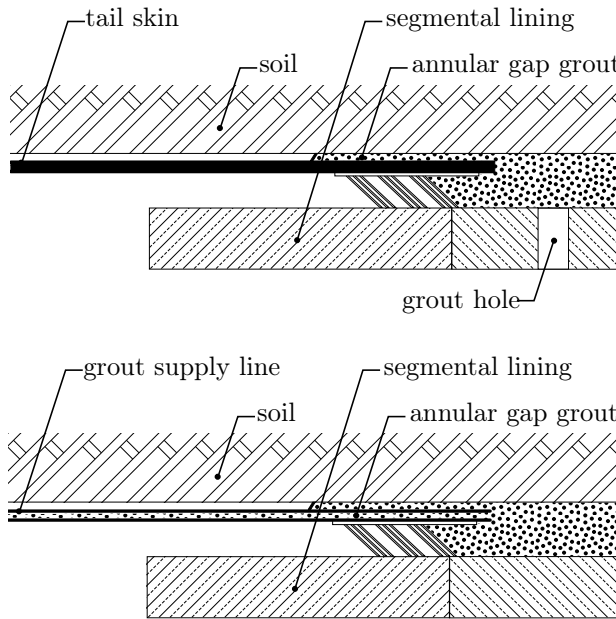


Figure 2.3: Longitudinal section of the tail skin and the segmental lining. Illustration of the grouting process using a discontinuous (top) and a continuous (bottom) technique (adapted from [96]).

## 2.2.2 Continuous annular gap grouting

To overcome the drawback of a temporary non-supported surrounding soil, the grouting can be realized continuously, cf. Figure 2.3 (bottom). This means that the ring build takes place protected by the TBM-shield. Directly after the completion of a lining segment, the grouting process is realized during the advance of the TBM. The grouting takes place through a grout supply line in the tail skin.

## 2.2.3 Further technical facilities for annular gap grouting

In addition to the grouting process itself, different technical facilities have to be described to reach an understanding of the overall process of the annular gap grouting. In order to prevent a fluid from entering the TBM, the tail skin of the TBM-shield is equipped with special sealings. Two different types of sealings are required. The main purpose of the sealing inside the tail skin is to retain the annular gap grouting mortar from entering the TBM-shield. In the beginning phase of mechanized tunnelling, different types of tissues, e.g. cleaning cloth, have been used. Recently, polymer and wire brush sealings were applied [58]. In case of polymer sealings, a polymer foam is used, which is fixed by a metal spring. For security reasons a further emergency sealing consisting of an inflatable material can be placed in front to avoid damages of the whole TBM in case of failure of the polymer sealing.

The safest way of sealing the gap between the lining and the tail skin is the wire brush. Thereby, up to four packages of wire brushes are fixed at the tail skin. The volume between single wire brush packages is filled with a grease-type high viscosity fluid. Through special supply channels for the fluid, the pressure in the volume between the wire brush packages is adjusted and the consumption of the fluid is equilibrated. By application of a fluid pressure on the grease, which is higher than the grouting pressure, the sealing is ensured. A failure of a part of the wire brush sealing can be registered by a higher grease consumption. As long as the grease pressure is reached, sealing even in case of a partial damage can be guaranteed, because the pressure gradient induces a flux of the grease and prevents mortar from entering the TBM. Additionally, a wear of the wire brushes is reduced by the use of grease. For an environmental friendly tunnelling process, the type of sealing fluid (grease) has to be chosen properly with focus on the environmental sustainability.

A second type of sealing is situated outside the tail skin, pointing towards the surrounding soil. If a fluid-based face support is used (cf. section 2.1), the outer sealing ensures a decoupling of support fluid and the annular gap grouting mortar. In case of tunnelling techniques without using a fluid for the face support (e.g. single and double shield TBM) the outer sealing prevents the annular gap grouting mortar from filling the steering gap. The outer sealing often consists of shingled spring sheet packages. However, ensuring a proper functionality is more challenging, compared to the sealing inside the tail skin. Depending on the geological situation, hollow spaces, larger than the actual annular gap might occur. Additionally, the porosity of the surrounding soil might lead to unwanted penetration of the grouting material in the direction of the excavation. However, the potential for damage and safety risk is much smaller in case of failure of the outer sealing, because the inner part of the TBM is not affected by the outer sealing.

For the injection of the annular gap grouting mortar in the annular gap, it is necessary to apply a pressure that depends on the mortar system and other settings but being always higher than the pore pressure of the surrounding soil. Mostly double piston pumps are used for this application. In case of 2-component mortars the use of progressive cavity pumps is also documented and for mortars containing only very fine particles peristaltic pumps were applied [96]. Injection is achieved using a separate pump for each grout supply line. A different pressure might be applied to each single grout supply line in order to take into account different geological properties or a varying pore pressure due to gravity. The pumping can be realized in a pressure based or volume based procedure. In case of a volume based grouting process, the theoretical volume which has to be filled is calculated. Then, the piston stroke is linked to the advance speed of the TBM. Following this procedure, hollow spaces in the surrounding soil are not considered. This might lead to a necessity of a secondary grouting, because a complete filling was not achieved by the first grouting. For the pressure driven grouting process, a minimum and maximum value for each piston pump is adjusted. The grouting process is evoked if the current pressure is smaller than the adjusted value and stopped if it reaches the maximum value. This process leads to a more

accurate grouting, if the pressure is adjusted properly. This is explained by the fact that the consumption of mortar is the result of the applied pressure gradient and not an *a priori* given value determined by theoretical calculations

Due to the large amount of mortar needed during the gap grouting process, the grout is prepared outside the tunnel. This means that the mortar needs to be transported after mixing and before grouting. For larger tunnel diameter, a continuous supply of annular gap grouting mortar via pipelines is used. This ensures permanent availability of annular gap grouting mortar at the TBM. During the advance of the tunnelling project the properties of freshly injected annular gap grouting mortar may change in time because the length of the pipeline and the resulting residence time of the annular gap grouting mortar within the pipeline increases. During disturbances, which might occur during the tunnelling progress, the annular gap grouting mortar remains in the supply lines. Depending on the type of used annular gap grouting mortar, this might lead to clogging of the supply pipe. This means that the clogged material has to be pressed out and the pipeline needs to be maintained, which is very costly.

For small tunnelling diameter, the required portion of annular gap grouting mortar can be transported to the TBM in discrete portions using special containers. The process has to be managed logistically, but clogging during disturbances even with cement-based annular gap grouting mortar is less of a problem.

#### 2.2.4 Grouting material

As previously described, the grouting material has to satisfy contrary requirements during the overall process. A proper choice of the grouting material is crucial for a stable bedding and the workability during the backfilling process. For mechanized tunnelling projects in granular soil, as described here, the following mortar systems are available: cement-based mortar, cement-free mortar, and two-component mortar. The cement-based grouting mortars are further subdivided in active and semi-active mortars, depending on the water to cement ratio, where the differentiation is not clearly defined. The basis formula of annular gap grouting mortar consist of different types of granular media like gravel, sand, and fly ash. Furthermore, a bentonite-slurry and additional water are used.

Cement-based mortars are widely used in the field of mechanized tunnelling. The idea is to fulfil the contrary requirements during the grouting process and the following life-time with the hydration process. For the construction phase the material has a very good workability. After a certain time, hydration ensures the required shear strength and therefore a stable bedding of the tunnel lining. Problems can occur due to buoyancy of the tunnel lining which might cause severe damages during the construction phase. This has to be accounted for by the formulation of the cement-based material. Furthermore, unwanted hydration, i.e. hydration during disturbances, leads to clogging of the supply pipes.

To overcome this issue, cement-free mortar systems were developed. Apart from the missing cement portion the composition is similar to the conventional cement-based mortar. The lack of cement has obvious advantages during the construction process. Even in case of long disturbances there is no clogging in the supply system of the TBM. Sedimentation occurs for very long disturbances, but cleaning of the system is much easier than in case of using cement-based mortars. The required shear strength of the material is achieved by dewatering of the cement-free mortar and not by hydration. The dewatering process requires a deep understanding of the physical phenomena and can not be established for very small permeabilities of the surrounding soil.

Two-component mortar systems do not require a certain permeability and are therefore a good choice for clay-type surrounding material. Two-component mortars consist of a similar composition as the active-mortar materials, but a liquid retarding agent is added in order to slow down the hydration. Therefore, the mixture is stable for 72 h [88]. Just before the grouting process, this mortar is mixed with sodium silicate, which leads to an immediate gelling of the material and later to hydration.

The present work is focussed on cement-free mortar and especially on the hydraulic and mechanical properties of the grouting mortar and the surrounding soil during and after the grouting process. Further application on active-mortar and two-component mortar is discussed in the last chapter.

### 2.2.5 State of the art

The practical aspects of the backfilling process of the annular gap were discussed in the previous part. This section is focussed on a literature review of publications related to the backfilling process.

Hashimoto *et al.* [39] describe the historical development of the grouting process, with a special focus on two-component grouting mortars. Thus, it is pointed out that continuous grouting reduces the settlements significantly. An overview about different grouting mortars which have been used in practical applications around the world is presented by Shirlaw *et al.* [77]. The authors highlight the importance of gap grouting in general and the opportunities of using locally sourced materials, instead of developing a fixed formula, for the grouting material. For this, a deep understanding of the rheological phenomena is crucial. General information about technical facilities, composition of grouting mortars, and process information in the framework of the backfilling process is summarized in a contribution of Thewes and Budach [96].

Talman and Bezuijen [90] conclude in their contribution about the grouting process at the Groene Hart Tunnel in the Netherlands, that the face support with a bentonite-slurry has an impact on the interface between the annular gap and the surrounding soil. The bentonite-slurry leads to clogging of the interface and therefore slows down the consolidation process of the annular gap grouting mortar. Furthermore, Bezuijen and Talmon [9] instrumented several tubbings of the segmental lining with pressure

sensors and conducted field measurements of the pressure of the annular gap grouting mortar during the grouting process itself and some time after it. The authors describe that the composition of the grouting material is crucial for the loading conditions of the tunnel lining directly behind the TBM. In a different work [8] pressure sensors were placed in a distance of 0.75 m radial to the tunnel lining before the tunnelling process. From this data, the derivation of the pressure gradient during tunnelling was observed.

The work of Thienert [97] is focussed on cement-free grouting materials. Driven by macroscopic experimental investigations it was found out, that in case of a correct formulation of the mortar, cement-free mortars are comparable to active mortars in terms of long-term stability and have even better physical properties regarding short-term stability. This finding was also supported by Wittke [106]. Laboratory experiments with the focus of the water desorption behaviour of mortars in general have been published by Carter *et al.* [20].

Numerical simulations of the overall tunnelling advance, considering the annular gap grouting, are proposed by Kasper and Meschke in [48]. For the simulation of the fully-saturated subsoil and the grouting material, a two-field finite element approach was used, with the result that a rapid evolution of the shear strength of the material leads to reduction of surface settlements. The grouting process is evaluated by a time-dependent mechanical parameter of the grouting material, which simulates the hydration process. This idea is traced back to investigations applied on shotcrete by Meschke [60] and Meschke *et al.* [61]. A numerical approach allowing real-time steering of the TBM, where also the grouting process is evaluated as described previously is presented by Ninić and Meschke [62]. A macroscopic numerical model focussing on the pressure evolution due to the grouting process was developed by Swoboda and Abu-Krishna [89]. Considering the grouting pressure, it is stated that the short time evolution of the settlements is mainly driven by the grouting pressure, whereas the long-term settlements are defined by the excess pore water pressure.

Concluding, many phenomena are experimentally and numerically well investigated in the broad field of mechanized tunnelling. However, most scientific research was performed on the macro scale, even though it is well known that the smallest particles are dominating transport properties of a granular mixture [69]. Those effects can only be understood by performing investigations on the micro scale. Therefore, micro scale and continuum models are derived and adapted in this work using an extended approach of the TPM. The field equations capturing ongoing physical processes are derived from balance equations for mass and momentum of individual constituents and their combinations. Additional micro-scale effects are simulated by consideration of statistical methods to describe the physics of granular porous media in combination with the TPM.

## Chapter 3

# Theoretical background of modelling hydro-mechanical coupled processes

*After the last chapter, which was focussed on relevant applications in the field of mechanized tunnelling, in this chapter, the theoretical framework for the simulation of infiltration phenomena is presented. First, a brief introduction about concepts of the Mixture Theory and the Theory of Porous Media is given. Subsequently, the kinematics within the Theory of Porous Media are discussed. In the last part of the chapter, the balance equations for a continuum description of a multi-phase material are presented.*

### 3.1 Mixture Theory

For the description of motion of multiple superimposed continua the *Mixture Theory* (MT) proposed by Truesdell is used [98, 99]. It is applied to describe motion of miscible mixtures. The basic idea of the MT is summarized by *Truesdell's metaphysical principles*:

- All properties of the mixture must be mathematical consequences of properties of the constituents.
- So as to describe the motion of a constituent, we may in imagination isolate it from the rest of the mixture, provided we allow properly for the actions of the other constituents upon it.
- The motion of the mixture is governed by the same equations as is a single body.

Note, that there are a plenty of Mixture Theories, which are independent of the one referred to in this contribution.

## 3.2 Theory of Porous Media

In order to obtain a description of the motion of immiscible mixtures, e.g. mixtures of fluids and solid constituents, or the mixture of a wetting and a non-wetting fluid, like water and oil, the TPM was invented. The idea of the TPM can be traced back to the MT. The TPM can be understood as an extension of the MT. In the TPM the concept of volume fractions is introduced. Despite the continuum-based homogenized formulation, a differentiation between single constituents is realized by accounting for the occupied volume of the constituents in the Representative Volume Element (RVE).

The TPM is developed to describe multi-phase problems on the continuum scale. In this part of the contribution the TPM is presented in order to develop a multi-phase model for infiltration processes of fully-saturated granular porous media. An overview about the historical development of the TPM is given by de Boer [24]. For further reading, literature of de Boer [13], Bowen [16, 17], Ehlers [28–30], and Steeb [82] are recommended.

### 3.2.1 Introductory definitions

Considering a continuum, which is a mixture of different constituents or phases, it is assumed that the constituents are perfectly homogeneously distributed within the volume. In other words, an averaging technique is applied on the volume leading to a model, which represents the physical mixture for simulation of certain processes. The mixture  $\varphi$  of the averaged phases in the volume is described as

$$\varphi = \bigcup_{\alpha} \varphi^{\alpha}, \quad (3.1)$$

with the phase  $\varphi^{\alpha}$  of a single constituent  $\alpha$ . The TPM evolves from the concept of volume fractions. Thereby, the definition

$$n^{\alpha} = \frac{dv^{\alpha}}{dv} \quad (3.2)$$

is used, with the volume fraction  $n^{\alpha}$ . The volume of the considered phase  $\varphi^{\alpha}$  is described by  $dv^{\alpha}$  and the total volume of the RVE as  $dv$ . The RVE is fully-saturated with different phases which might be present in any state of matter (solid, liquid, or gas). Therefore, the saturation condition is formulated as

$$\sum_{\alpha} n^{\alpha} = 1. \quad (3.3)$$

The main objective of this contribution is to analyse phase transition processes. In the following parts of the work, different subdivisions of the RVE into phases are carried out. Nevertheless, for geotechnical applications of the TPM, often the soil is considered as a solid skeleton. It is very familiar, that the soil does not fill the RVE

completely, but consists of hollow spaces, i.e. the pores, which are filled with other constituents, e.g. pore liquids or pore gases. Hence, for a physical interpretation of such problems the porosity  $\phi$  of an RVE is defined as

$$\phi = \frac{dv^f}{dv}, \quad (3.4)$$

with  $dv^f$  describing the volume of the sum of volumes of phases occupying the pore-space. In multi-phase approaches different densities can be used, depending on the current application. The partial density  $\rho^\alpha$  reads

$$\rho^\alpha = \frac{dm^\alpha}{dv}, \quad (3.5)$$

where the mass of an individual constituent  $\varphi^\alpha$  of a local volume element  $dv$  is denoted as  $dm^\alpha$ . The effective (or true) density  $\rho^{\alpha R}$  is expressed via

$$\rho^{\alpha R} = \frac{dm^\alpha}{dv^\alpha}. \quad (3.6)$$

The density of the mixture  $\rho$  is a special case of Eq. (3.5) if the volume and the mass  $dm$  of the mixture within the RVE is considered

$$\rho = \frac{dm}{dv}. \quad (3.7)$$

The partial and the effective densities are linked with each other by the volume fraction, with the relation

$$\rho^\alpha = n^\alpha \rho^{\alpha R}. \quad (3.8)$$

As it will be shown later, the derivation of multi-field models using the TPM often demand exchange of mass between individual constituents of the mixture. Therefore, production terms are defined. Thus, a similar link is also applied for the mass production  $\hat{\rho}^\alpha$  and the volume production  $\hat{n}^\alpha$

$$\hat{\rho}^\alpha = \hat{n}^\alpha \rho^{\alpha R}, \quad (3.9)$$

which allows to describe exchanges between single constituents of the mixture.

### 3.2.2 Kinematics in the Theory of Porous Media

For the formulation of the kinematics within the framework of the TPM the current and the initial configurations of the observed body are differentiated. Kinematical quantities describing the initial configuration are denoted with capital letters, whereas quantities of the current configuration are described with small letters.

Following the metaphysical principles of Truesdell, cf. section 3.1, the motion of a superimposed mixture can be described by the single motions of the constituents. The motion of each constituent follows an individual motion function, with the conse-

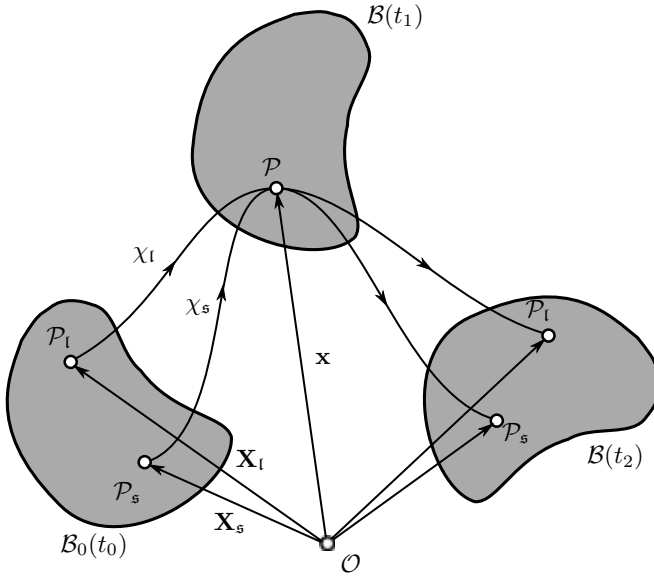


Figure 3.1: Kinematics of a two-phase mixture  $\alpha = \{s, l\}$ , with time  $t_0 < t_1 < t_2$ . The motion of each constituent  $\varphi^\alpha$  is described by an individual motion function  $\chi_\alpha$ , with  $\mathcal{P}_\alpha$  depicting the spatial position of the constituent  $\varphi^\alpha$  within the body of the mixture  $\mathcal{B}$ .

quence that at a current configuration for the time  $t$ , a spatial point  $\mathbf{x}$  can be occupied by all constituents  $\varphi^\alpha$  simultaneously whereas each constituent  $\varphi^\alpha$  occupies an individual material point  $\mathbf{X}$  in the reference configuration for the time  $t_0$ , cf. Figure 3.1. Using the Lagrangian description, the motion function  $\chi_\alpha$  of a certain constituent  $\varphi^\alpha$  reads

$$\mathbf{x} = \chi_\alpha(\mathbf{X}_\alpha, t). \quad (3.10)$$

It is postulated that the motion function is unique and uniquely invertible [13], which leads directly to the Eulerian description of the motion of a single phase

$$\mathbf{X}_\alpha = \chi_\alpha^{-1}(\mathbf{x}, t), \quad (3.11)$$

where the inverse of the motion function of the constituent  $\varphi^\alpha$  is denoted as  $\chi_\alpha^{-1}$ . As a consequence, also the velocity  $\mathbf{v}_\alpha$  and the acceleration  $\mathbf{a}_\alpha$  are unique for each constituent  $\varphi^\alpha$  and can be formulated using an Eulerian and a Lagrangian description. In the Eulerian case it can be written

$$\mathbf{v}_\alpha = \mathbf{x}'_\alpha(\mathbf{x}, t) \quad \text{and} \quad \mathbf{a}_\alpha = \mathbf{x}''_\alpha(\mathbf{x}, t), \quad (3.12)$$

where the superscript is denoting the order of the material derivative. In the Lagrangian case the velocity and the acceleration field are formulated as

$$\mathbf{v}_\alpha = \mathbf{x}'_\alpha(\mathbf{X}_\alpha, t) = \frac{\partial \chi_\alpha(\mathbf{X}_\alpha, t)}{\partial t} \quad \text{and} \quad \mathbf{a}_\alpha = \mathbf{x}''_\alpha(\mathbf{X}_\alpha, t) = \frac{\partial^2 \chi_\alpha(\mathbf{X}_\alpha, t)}{\partial t^2}. \quad (3.13)$$

The barycentric velocity, which describes the velocity of the mixture of the multi-phase material, can be written

$$\dot{\mathbf{x}} = \frac{1}{\rho} \sum_\alpha \rho^\alpha \mathbf{x}'_\alpha. \quad (3.14)$$

From a mathematical point of view Eq. (3.11) has a unique solution, i.e. the inverse of the motion function  $\chi_\alpha$  exists, if the necessary and sufficient condition for the Jacobian

$$J_\alpha = \det \mathbf{F}_\alpha > 0 \quad (3.15)$$

is fulfilled. The deformation gradient is depicted as  $\mathbf{F}_\alpha$  with

$$\mathbf{F}_\alpha = \frac{\partial \mathbf{x}}{\partial \mathbf{X}_\alpha} = \text{Grad}_\alpha \chi_\alpha(\mathbf{X}_\alpha, t) = \text{Grad}_\alpha \mathbf{x}. \quad (3.16)$$

Within Eq. (3.16) the abbreviation  $\text{Grad}_\alpha$ , which describes the partial derivative of a quantity with respect to the position vector  $X_\alpha$  in the reference configuration of the constituent  $\varphi^\alpha$ . For the inverse of the deformation gradient  $\mathbf{F}_\alpha^{-1}$  it can be stated

$$\mathbf{F}_\alpha^{-1} = \frac{\partial \mathbf{X}_\alpha}{\partial \mathbf{x}} = \text{grad} \chi_\alpha^{-1}(\mathbf{x}, t) = \text{grad} \mathbf{X}_\alpha. \quad (3.17)$$

The material time derivative  $[\Upsilon]'_\alpha$  of an arbitrary field quantity  $\Upsilon$  describes the rate at which the field quantity  $\Upsilon$  changes with respect to time as observed from the spatial position along a trajectory of a constituent  $\varphi^\alpha$

$$[\Upsilon]'_\alpha = \frac{\partial \Upsilon}{\partial t} + \text{grad} \Upsilon \cdot \mathbf{x}'_\alpha. \quad (3.18)$$

Physically, the first part of the equation describes the time derivative of the field quantity  $\Upsilon$ , observed locally at one spatial position. The second part is the convective term, taking into account the change in position of a constituent  $\varphi^\alpha$  which moves with the velocity  $\mathbf{v}_\alpha$ . The convective part of the material time derivative is non-linear. For a linear description this part is neglected [82].

Hence, the material time derivative of a field quantity  $\Upsilon$  with respect to the motion of the mixture is given as

$$\dot{\Upsilon} = \frac{\partial \Upsilon}{\partial t} + \text{grad} \Upsilon \cdot \dot{\mathbf{x}}. \quad (3.19)$$

In general, the definition of constituents is arbitrary, but obviously linked to the state of matter of a certain constituent. Since the TPM is often used for geotechnical

applications, it is convenient to differentiate between fluid phases, which in combination are denoted as the liquid phase  $\varphi^l$ . On the other hand, the solid phases are described by  $\varphi^s$ . Later it will be shown that for some applications the combination of solid and fluid phases is appropriate, e.g. to capture the behaviour of a suspension. However, with respect to numerical implementation, the solid phase is described with a Lagrangian formulation by the definition of the solid displacement

$$\mathbf{u}_s = \mathbf{x} - \mathbf{X}_s, \quad (3.20)$$

whereas for the liquid constituent an Eulerian approach is used, describing the motion of the liquid with the velocity  $\mathbf{v}_l$  relative to the velocity of the solid  $\mathbf{v}_s$ . Therefore, the seepage velocity  $\mathbf{w}$  is introduced as

$$\mathbf{w} = \mathbf{v}_l - \mathbf{v}_s. \quad (3.21)$$

Furthermore, the filter velocity or Darcy velocity is formulated as

$$\mathbf{q} = \phi (\mathbf{v}_l - \mathbf{v}_s), \quad (3.22)$$

with  $\mathbf{v}_s$  being the velocity of the solid,  $\mathbf{v}_l$  the velocity of the liquid, and  $\phi$  the porosity of the solid skeleton.

The spatial velocity gradient

$$\mathbf{L}_\alpha = \text{grad } \mathbf{v}_\alpha = (\mathbf{F}_\alpha)'_\alpha \cdot \mathbf{F}_\alpha^{-1}, \quad (3.23)$$

does not depend on the classification of the constituents in fluid or solid phases. The additive decomposition of the spatial velocity gradient  $\mathbf{L}_\alpha$  into a symmetric part  $\mathbf{D}_\alpha$  and a skew-symmetric part  $\mathbf{W}_\alpha$  reads

$$\mathbf{L}_\alpha = \mathbf{D}_\alpha + \mathbf{W}_\alpha, \quad \text{with} \quad \begin{cases} \mathbf{D}_\alpha = \frac{1}{2} (\mathbf{L}_\alpha + \mathbf{L}_\alpha^T), \\ \mathbf{W}_\alpha = \frac{1}{2} (\mathbf{L}_\alpha - \mathbf{L}_\alpha^T). \end{cases} \quad (3.24)$$

For constitutive modelling, the local deformations  $\mathbf{F}_\alpha$  are not appropriate, because they contain not only deformation of the material but rigid body motions, as well. This means a measure of deformations that is invariant with respect to rigid body motion is required. For this, the mapping of line elements within the body between the reference and the actual configuration is defined as

$$d\mathbf{x} = \mathbf{F}_\alpha \cdot d\mathbf{X}_\alpha. \quad (3.25)$$

Following, the lengths of the line elements  $l$  and  $L_\alpha$  are obtained from the absolute value of the line elements

$$l = |d\mathbf{x}| \quad \text{and} \quad L_\alpha = |d\mathbf{X}_\alpha|, \quad (3.26)$$

with the corresponding normalized line elements  $d\tilde{\mathbf{x}}$  and  $d\tilde{\mathbf{X}}_\alpha$ . Using these relations the stretch  $\lambda_\alpha$  is defined as

$$\lambda_\alpha d\tilde{\mathbf{x}} = \mathbf{F}_\alpha \cdot d\tilde{\mathbf{X}}_\alpha, \quad (3.27)$$

where  $\lambda_\alpha$  is expressed as  $\lambda_\alpha = l/L_\alpha$  with the restriction  $\lambda_\alpha > 0$ . Measures for the partial deformations are obtained by introducing the left Cauchy-Green deformation tensor  $\mathbf{B}_\alpha$  and the right Cauchy-Green deformation tensor  $\mathbf{C}_\alpha$

$$\mathbf{B}_\alpha = \mathbf{F}_\alpha \cdot \mathbf{F}_\alpha^T \quad \text{and} \quad \mathbf{C}_\alpha = \mathbf{F}_\alpha^T \cdot \mathbf{F}_\alpha. \quad (3.28)$$

Exploiting Eq. (3.25) the following relation can be obtained [82]

$$d\mathbf{x} \cdot d\mathbf{x} - d\mathbf{X}_\alpha \cdot d\mathbf{X}_\alpha = d\mathbf{X}_\alpha \cdot (2\mathbf{E}_\alpha) \cdot d\mathbf{X}_\alpha = d\mathbf{x} \cdot (2\mathbf{A}_\alpha) \cdot d\mathbf{x}, \quad (3.29)$$

defining the Green-Lagrange strain tensor  $\mathbf{E}_\alpha$  and the Almansi strain tensor  $\mathbf{A}_\alpha$ . Alternatively, both tensors can be also obtained by

$$\mathbf{E}_\alpha = \frac{1}{2}(\mathbf{C}_\alpha - \mathbf{I}) \quad \text{and} \quad \mathbf{A}_\alpha = \frac{1}{2}(\mathbf{I} - \mathbf{B}_\alpha^{-1}), \quad (3.30)$$

with the second order identity tensor  $\mathbf{I}$ .

### 3.3 Balance equations

In order to use the TPM for certain multi-physical applications, field equations have to be derived. In general, balance relations for single constituents or a combination of constituents are employed for this. The continuum-based balance relations, which are presented here, are traced back to the classical continuum formulation, taking only one constituent into account. Considering Truesdell's metaphysical principles, cf. section 3.1, it can be stated that an analogy between the balance relations of single constituents or the whole mixture of the multi-physical TPM and the classical one-field formulation of continuum theory exists, if coupling of single fields within the multi-phase approach is taken into account. This means, in order to describe the behaviour of a (multi-field) continuum, balance equations in the global or the local form are used. The global form characterizes an arbitrary body  $\mathcal{B}$ , whereas the local form specifies the behaviour of the material point  $\mathcal{P}$ , cf. Figure 3.1.

It has to be pointed out that balance equations are introduced in an axiomatic way. This chapter can not be understood as a complete description of the balance equations of the TPM, but as a basic overview of the balance equations, with a focus on the equations which are required for the modelling approach of infiltration phenomena presented later. Furthermore, the balance equations are introduced in the classical order balancing the following physical quantities: mass, momentum, moment of momentum, energy, and entropy.

### 3.3.1 Balance of mass

The mass balance of a single constituent in local form is derived balancing the change of the mass  $\mathcal{M}^\alpha = \int_{\mathcal{B}} \rho^\alpha dv$  of a constituent  $\varphi^\alpha$  with the mass exchange rate  $\hat{\mathcal{M}}^\alpha = \int_{\mathcal{B}} \hat{\rho}^\alpha dv$ , which describes the interaction of individual constituents

$$[\mathcal{M}^\alpha]'_\alpha = \hat{\mathcal{M}}^\alpha, \quad (3.31)$$

with the algebraic restriction

$$\sum_\alpha \hat{\mathcal{M}}^\alpha = 0. \quad (3.32)$$

The local form of the mass balance of a single constituent reads

$$(\rho^\alpha)'_\alpha + \rho^\alpha \operatorname{div} \mathbf{v}_\alpha = \hat{\rho}^\alpha, \quad (3.33)$$

or, using the product rule and the definition of the material time derivative, cf. Eq.(3.18), and the abbreviation  $\partial_t = \frac{\partial}{\partial t}$  it can be rewritten to read

$$\partial_t(\rho^\alpha) + \operatorname{div}(\rho^\alpha \mathbf{v}_\alpha) = \hat{\rho}^\alpha. \quad (3.34)$$

For practical applications it is convenient to include the concept of volume fractions within the local mass balance equation. For this, the definition of the partial density  $\rho^\alpha$  given in Eq. (3.8) and the definition of the mass production  $\hat{\rho}^\alpha$ , cf. Eq. (3.9), are used, obtaining

$$(n^\alpha \rho^{\alpha R})'_\alpha + n^\alpha \rho^{\alpha R} \operatorname{div} \mathbf{v}_\alpha = \hat{n}^\alpha \rho^{\alpha R}, \quad (3.35)$$

or analogue to Eq. (3.34)

$$\partial_t(n^\alpha \rho^{\alpha R}) + \operatorname{div}(n^\alpha \rho^{\alpha R} \mathbf{v}_\alpha) = \hat{n}^\alpha \rho^{\alpha R}. \quad (3.36)$$

In case of the mass balance of the mixture, interaction terms are not required. On the other hand the mass balance of the mixture can also be formulated with respect to the density and velocity of the mixture. Therefore, the mass balance consists of the rate of mass of the mixture  $\frac{d}{dt} [\mathcal{M}] = 0$ . Thus, the local form of the mass balance of the mixture is formulated as

$$\dot{\rho} + \rho \operatorname{div} \mathbf{v} = 0 \quad \text{or} \quad \partial_t(\rho) + \operatorname{div}(\rho \mathbf{v}) = 0. \quad (3.37)$$

For the development of a multi-phase model it is often convenient to sum up different local partial mass balances for individual constituents, according to Eq. (3.34). If a formulation with respect to phase velocities is desired, the local mass balance of the mixture can also be obtained by summing up all constituents of the mixture.

### 3.3.2 Balance of momentum

For the definition of the balance of momentum of a single constituent  $\varphi^\alpha$ , first the momentum  $\mathcal{L}^\alpha$ , the external and body forces  $\mathcal{F}^\alpha$  and the total momentum production  $\hat{\mathcal{S}}^\alpha$  are given as

$$\mathcal{L}^\alpha = \int_{\mathcal{B}} \rho^\alpha \mathbf{v}_\alpha dv, \quad (3.38)$$

$$\mathcal{F}^\alpha = \int_{\partial\mathcal{B}} \mathbf{t}^\alpha da + \int_{\mathcal{B}} \rho^\alpha \mathbf{b}^\alpha dv, \quad (3.39)$$

$$\hat{\mathcal{S}}^\alpha = \int_{\mathcal{B}} \hat{\mathbf{s}}^\alpha dv, \quad (3.40)$$

with the traction forces  $\mathbf{t}^\alpha$ , the body force of a constituent  $\mathbf{b}^\alpha$ , and the interaction forces  $\hat{\mathbf{s}}^\alpha$ . The global balance of momentum of a single constituent  $\varphi^\alpha$  reads

$$[\mathcal{L}^\alpha]'_\alpha = \mathcal{F}^\alpha + \hat{\mathcal{S}}^\alpha, \quad \text{with} \quad \sum_\alpha \hat{\mathcal{S}}^\alpha = \mathbf{0}. \quad (3.41)$$

To derive the local form of the balance of momentum of a constituent, the following theorems are introduced

$$\text{Cauchy-theorem :} \quad \mathbf{t}^\alpha = \mathbf{T}^\alpha \cdot \mathbf{n}, \quad (3.42)$$

$$\text{divergence-theorem :} \quad \int_{\mathcal{B}} \text{div}(\mathbf{\Upsilon}) dv = \int_{\partial\mathcal{B}} \mathbf{\Upsilon} \cdot \mathbf{n} da, \quad (3.43)$$

$$\text{Reynolds transport-theorem :} \quad \frac{d}{dt} \int_{\mathcal{B}} \mathbf{\Upsilon}^\alpha(\mathbf{x}, t) dv = \int_{\mathcal{B}} \frac{\partial \mathbf{\Upsilon}^\alpha}{\partial t} dv + \int_{\partial\mathcal{B}} \mathbf{\Upsilon}^\alpha \mathbf{v}_\alpha \cdot \mathbf{n} da, \quad (3.44)$$

with the Cauchy-stress tensor  $\mathbf{T}^\alpha$ , the outer normal vector  $\mathbf{n}$ , a continuously differentiable vector field  $\mathbf{\Upsilon}$ , and the field quantity of a constituent  $\mathbf{\Upsilon}^\alpha$ .

Furthermore, the local balance of the mass, cf. Eq. (3.34) and the relations in Eqs. (3.38 - 3.40) are inserted in Eq. (3.41). Thereby, the local form of the balance of momentum of a constituent is obtained as

$$\rho^\alpha \mathbf{a}_\alpha - \text{div} \mathbf{T}^\alpha = \rho^\alpha \mathbf{b}^\alpha + \hat{\mathbf{p}}^\alpha, \quad (3.45)$$

with the direct momentum production

$$\hat{\mathbf{p}}^\alpha = \hat{\mathbf{s}}^\alpha - \hat{\rho}^\alpha \mathbf{v}_\alpha. \quad (3.46)$$

For the local balance of momentum the algebraic constraint of vanishing interaction terms for the mixture

$$\sum_{\alpha} \hat{\mathbf{s}}^{\alpha} = \sum_{\alpha} \hat{\mathbf{p}}^{\alpha} + \sum_{\alpha} \hat{\rho}^{\alpha} \mathbf{v}_{\alpha} = \mathbf{0} \quad (3.47)$$

is also valid. Thus, the local balance of the mixture is given as

$$\rho \mathbf{a} - \operatorname{div} \mathbf{T} = \rho \mathbf{b}. \quad (3.48)$$

As it will be shown later, the choice, for which constituents or mixture the local balance of momentum is evaluated in a particular multi-phase model, determines the physical interpretation of the required boundary conditions.

### 3.3.3 Balance of moment of momentum

The partial balance of the moment of momentum of one constituent  $\varphi^{\alpha}$  balances change of the moment of momentum  $\mathcal{J}^{\alpha}$  with the moment of external forces  $\mathcal{M}^{\alpha}$  and the production of moment of momentum  $\hat{\mathcal{H}}^{\alpha}$ . Following, the global partial balance of moment of momentum reads

$$[\mathcal{J}^{\alpha}]'_{\alpha} = \mathcal{M}^{\alpha} + \hat{\mathcal{H}}^{\alpha}, \quad (3.49)$$

where the single terms can be denoted as

$$\mathcal{J}^{\alpha} = \int_{\mathcal{B}} (\mathbf{x} - \mathbf{x}_0) \times (\rho^{\alpha} \mathbf{v}_{\alpha}) \, dv, \quad (3.50)$$

$$\mathcal{M}^{\alpha} = \int_{\partial \mathcal{B}} (\mathbf{x} - \mathbf{x}_0) \times (\mathbf{t}^{\alpha}) \, da + \int_{\mathcal{B}} (\mathbf{x} - \mathbf{x}_0) \times (\rho^{\alpha} \mathbf{b}^{\alpha}) \, dv, \quad (3.51)$$

$$\hat{\mathcal{H}}^{\alpha} = \int_{\mathcal{B}} \hat{\mathbf{h}}^{\alpha} \, dv, \quad (3.52)$$

with the interaction moments between individual constituents  $\hat{\mathbf{h}}^{\alpha}$ . Corresponding to the balances presented before, the balance of moment of momentum is subject to the algebraic constraint

$$\sum_{\alpha} \hat{\mathcal{H}}^{\alpha} = \mathbf{0}, \quad (3.53)$$

which is used to equilibrate the production of moment of momentum within the mixture.

The local form of the balance of moment of momentum of one constituent  $\varphi^{\alpha}$  can be obtained considering the global form Eq. (3.49) by inserting the partial balance of mass Eq. (3.33) and the partial balance of momentum Eq. (3.45), and using the theorems given in Eqs. (3.42) - (3.44). Thus, it is written as

$$\mathbf{I} \times \mathbf{T}^{\alpha} = -\hat{\mathbf{m}}^{\alpha}, \quad (3.54)$$

where the direct moment of momentum production is depicted as  $\hat{\mathbf{m}}^\alpha$ , with the constraint for the mixture

$$\sum_{\alpha} \hat{\mathbf{m}}^\alpha = \mathbf{0}. \quad (3.55)$$

Assuming,  $\hat{\mathbf{m}}^\alpha = 0$ , i.e. no interaction of moment of momentum within single constituents, Eq. (3.54) leads to the statement of a symmetric partial Cauchy-stress tensor  $\mathbf{T}^\alpha$

$$\mathbf{I} \times \mathbf{T}^\alpha = \mathbf{0}, \quad \Rightarrow \quad \mathbf{T}^\alpha = (\mathbf{T}^\alpha)^T. \quad (3.56)$$

In general, the symmetry of the Cauchy-stress tensor  $\mathbf{T}^\alpha$  is a broadly used restriction, which is often not derived from the balance of moment of momentum, but introduced as the so-called Boltzmann axiom [55]. In the remainder of this contribution, symmetry of the Cauchy-stress tensor  $\mathbf{T}^\alpha$  is always assumed.

### 3.3.4 Balance of energy

The balances of mass, momentum and moment of momentum are sufficient for the description of mechanical processes. However, for the coupling of temperature fields of single constituents the energy balance has to be employed. The balance of energy corresponds to the first law of thermodynamics, describing whether an energy driven process will take place. Thus, the global partial energy balance of a single constituent  $\varphi^\alpha$  balances the change in the internal energy  $\mathcal{E}^\alpha$  and the kinetic energy  $\mathcal{K}^\alpha$  with the external mechanical power  $\mathcal{P}_{\text{ext}}^\alpha$ , the thermal power  $\mathcal{Q}^\alpha$ , and the total energy production  $\hat{\mathcal{E}}^\alpha$ . The global partial energy balance reads

$$[\mathcal{E}^\alpha + \mathcal{K}^\alpha]'_{\alpha} = \mathcal{P}_{\text{ext}}^\alpha + \mathcal{Q}^\alpha + \hat{\mathcal{E}}^\alpha. \quad (3.57)$$

The individual terms are defined as

$$\mathcal{E}^\alpha = \int_{\mathcal{B}} \rho^\alpha \varepsilon^\alpha \, dv, \quad (3.58)$$

$$\mathcal{K}^\alpha = \int_{\mathcal{B}} \frac{1}{2} \rho^\alpha \mathbf{v}_\alpha \cdot \mathbf{v}_\alpha \, dv, \quad (3.59)$$

$$\mathcal{P}_{\text{ext}}^\alpha = \int_{\partial \mathcal{B}} \mathbf{t}^\alpha \cdot \mathbf{v}_\alpha \, da + \int_{\mathcal{B}} \rho^\alpha \mathbf{b}^\alpha \cdot \mathbf{v}_\alpha \, dv, \quad (3.60)$$

$$\mathcal{Q}^\alpha = \int_{\partial \mathcal{B}} q^\alpha \, da + \int_{\mathcal{B}} \rho^\alpha r^\alpha \, dv \quad (3.61)$$

$$\hat{\mathcal{E}}^\alpha = \int_{\mathcal{B}} \hat{e}^\alpha \, dv, \quad (3.62)$$

with the specific internal energy  $\varepsilon^\alpha$ , the partial heat flux  $q^\alpha$ , the partial energy source  $r^\alpha$ , and the energy supply  $\hat{e}^\alpha$  caused by the other constituents. For the definition of

the heat flux  $q^\alpha$ , Stokes' heat flux theorem

$$q^\alpha = \mathbf{q}^\alpha \cdot \mathbf{n}, \quad (3.63)$$

is used with the heat flux vector  $\mathbf{q}^\alpha$ . The sign convention of the scalar heat flux  $q^\alpha$  is determined by the outward unit vector  $\mathbf{n}$ . Note, that different conventions are used for the same framework throughout the literature.

In order to obtain the local partial balance of energy, Eqs. (3.58 - 3.62) are inserted in Eq. (3.57). With the local partial balance of momentum, cf. Eq. (3.45), it can be written

$$\rho^\alpha (\varepsilon^\alpha)'_\alpha = \mathbf{T}^\alpha : \mathbf{D}_\alpha - \operatorname{div} \mathbf{q}^\alpha + \rho^\alpha r^\alpha + \hat{\varepsilon}^\alpha + \hat{\mathbf{p}}^\alpha \cdot \mathbf{v}_\alpha + \hat{\rho}^\alpha (\varepsilon^\alpha + \frac{1}{2} \mathbf{v}_\alpha \cdot \mathbf{v}_\alpha). \quad (3.64)$$

### 3.3.5 Balance of entropy

In contrast to all other balances presented so far, the balance of entropy is not a conservation law. It is also called the second law of thermodynamics and describes whether a reaction which is consistent to the other balances takes place in nature. The partial balance of entropy of an individual constituent  $\varphi^\alpha$  balances the change of entropy  $\mathcal{S}^\alpha$  with the rate of entropy  $\mathcal{H}^\alpha$  and the total entropy production  $\hat{\mathcal{R}}^\alpha$ . Following the same structure as used so far, the global partial balance of entropy reads

$$[\mathcal{S}^\alpha]'_\alpha = \mathcal{H}^\alpha + \hat{\mathcal{R}}^\alpha. \quad (3.65)$$

The individual terms are given as

$$\mathcal{S}^\alpha = \int_{\mathcal{B}} \rho^\alpha \eta^\alpha \, dv, \quad (3.66)$$

$$\mathcal{H}^\alpha = \int_{\partial \mathcal{B}} \varphi_\eta^\alpha \cdot \mathbf{n} \, da + \int_{\mathcal{B}} \rho^\alpha s_\eta^\alpha \, dv, \quad (3.67)$$

$$\hat{\mathcal{R}}^\alpha = \int_{\mathcal{B}} \hat{\eta}^\alpha \, dv, \quad (3.68)$$

with the specific entropy  $\eta^\alpha$ , the Cauchy entropy flux  $\varphi_\eta^\alpha$ , the influx of entropy  $s_\eta^\alpha$ , and the total entropy production  $\hat{\eta}^\alpha$  describing the entropy exchange between individual constituents.

The local form of the partial balance of entropy reads

$$\rho^\alpha (\eta^\alpha)'_\alpha + \operatorname{div} \varphi_\eta^\alpha - \rho^\alpha s_\eta^\alpha = \hat{\zeta}^\alpha. \quad (3.69)$$

Denoting  $\hat{\zeta}^\alpha$  as the direct entropy production, which can be related to the total entropy production  $\hat{\eta}^\alpha$

$$\hat{\eta}^\alpha = \hat{\zeta}^\alpha + \eta^\alpha \hat{\rho}^\alpha. \quad (3.70)$$

Following de Boer [13] the fulfilment of the local form of the partial balance of entropy leads to sufficient, but too restricted, results. Therefore, the condition for the entropy production for the mixture is introduced as

$$\sum_{\alpha} \hat{\eta}^{\alpha} \geq 0. \quad (3.71)$$

This definition is achieved, in similar manner to the balance equations, axiomatically [82].

### 3.4 Linearisation

In general, Initial Boundary Value Problems (IBVP's) developed with the TPM that consider a multi-field formulation result in non-linear system of equations. For the numerical solution of the IBVP, the field equations are linearised, to achieve a linear system of equations. Therefore, the Gateaux or directional derivative is used, e.g. Ehlers and Bluhm [30], Steeb [82]. For a vectorial quantity  $\Upsilon$  the Gateaux derivative  $\mathcal{D}$ , with respect to a perturbation  $\Delta \mathbf{X}$  is given as

$$\mathcal{D}\Upsilon(\mathbf{X})[\Delta \mathbf{X}] = \left. \frac{d}{d\beta} (\Upsilon(\mathbf{X}_0 + \beta \Delta \mathbf{X})) \right|_{\beta=0}. \quad (3.72)$$

In this case,  $\mathbf{X}_0$  is the position vector of the reference configuration. Therewith, a linearised vectorial quantity is defined as

$$\text{lin}(\Upsilon) = \Upsilon_0 + \mathcal{D}\Upsilon. \quad (3.73)$$

As an example the Green-Lagrange strain tensor  $\mathbf{E}_s$  of a solid constituent  $\varphi^s$  is linearised, using the concept of linearisation, to obtain the strain measurement  $\varepsilon_s$  valid for small deformations. Thus, it is written

$$\text{lin}(\mathbf{E}_s) = \mathbf{E}_{s,0} + \mathcal{D}\mathbf{E}_s. \quad (3.74)$$

With the deformation of the solid  $\mathbf{u}_s = \mathbf{x} - \mathbf{X}_s$ , the deformation gradient of the solid  $\mathbf{F}_s$  and it's inverse  $\mathbf{F}_s^{-1}$  can be rewritten to

$$\mathbf{F}_s = \frac{\mathbf{x}}{\mathbf{X}_s} = \mathbf{I} + \text{Grad}_s \mathbf{u}_s, \quad (3.75)$$

$$\mathbf{F}_s^{-1} = \frac{\mathbf{X}_s}{\mathbf{x}} = \mathbf{I} - \text{grad} \mathbf{u}_s. \quad (3.76)$$

Thus, the Green-Lagrange strain tensor reads

$$\begin{aligned}\mathbf{E}_s &= \frac{1}{2} (\mathbf{F}_s^T \cdot \mathbf{F}_s - \mathbf{I}) \\ &= \frac{1}{2} \left( \text{Grad}_s \mathbf{u}_s + \text{Grad}_s^T \mathbf{u}_s + \text{Grad}_s^T \mathbf{u}_s \text{Grad}_s \mathbf{u}_s \right).\end{aligned}\quad (3.77)$$

Applying the definition of the directional derivative in Eq. (3.72) to Eq. (3.77), it is obtained

$$\begin{aligned}\text{lin}(\mathbf{E}_s) &= \frac{1}{2} \left( \text{Grad}_s \mathbf{u}_{s,0} + \text{Grad}_s^T \mathbf{u}_{s,0} + \text{Grad}_s^T \mathbf{u}_{s,0} \text{Grad}_s \mathbf{u}_{s,0} \right. \\ &\quad \left. + \frac{d}{d\beta} \left[ \text{Grad}_s (\mathbf{u}_{s,0} + \beta \Delta \mathbf{u}_s) + \text{Grad}_s^T (\mathbf{u}_{s,0} + \beta \Delta \mathbf{u}_s) \right. \right. \\ &\quad \left. \left. + \text{Grad}_s^T (\mathbf{u}_{s,0} + \beta \Delta \mathbf{u}_s) \text{Grad}_s (\mathbf{u}_{s,0} + \beta \Delta \mathbf{u}_s) \right]_{\beta=0} \right).\end{aligned}\quad (3.78)$$

Assuming small deformations,  $\Delta \mathbf{u}_s = \mathbf{u}_s$ , and an undeformed reference configuration,  $\mathbf{u}_{s,0} = \mathbf{0}$ , the linearised solid strain  $\varepsilon_s$  is obtained as

$$\varepsilon_s := \text{lin}(\mathbf{E}_s(\mathbf{u}_{s,0} = \mathbf{0})) = \frac{1}{2} \left( \text{Grad}_s \mathbf{u}_s + \text{Grad}_s^T \mathbf{u}_s \right).\quad (3.79)$$

Following Steeb *et al.* [87], it is pointed out that the linearised material time derivative of a quantity  $\Upsilon$  is identical to the partial derivative

$$\text{lin}([\Upsilon]'_\alpha) = \frac{\partial \Upsilon}{\partial t} = \partial_t(\Upsilon).\quad (3.80)$$

Thus, the non-linear convection part of the material time derivative, cf. Eq. (3.18), is neglected after the linearisation.

### 3.5 Constitutive modelling

In the last section the balance equations in the framework of the TPM were presented. The partial local equations balancing mass, moment, moment of momentum, and energy for individual constituents are used to obtain the field equations for the description of the behaviour of a body. However, the balance of entropy is used to evaluate whether a process, which is in accordance with the aforementioned balance equations, will take place in nature or not. For a numerical realization of a particular process constitutive equations are required that describe the material properties, which are not captured by the balance equations. Making use of the balance of entropy we can find a priori restrictions for the constitutive equations in order to achieve a thermodynamically-consistent numerical model.

### 3.5.1 Concept of effective stress

Considering a fully saturated biphasic porous medium consisting of a porous skeleton, represented by the constituent  $\varphi^s$ , and a pore fluid with the constituent  $\varphi^f$  and following de Boer [13], the Cauchy stress of the mixture can be additively decomposed to

$$\mathbf{T} = \mathbf{T}^s + \mathbf{T}^f, \quad (3.81)$$

with the Cauchy stress of the solid skeleton  $\mathbf{T}^s$  and the Cauchy stress of the fluid constituent  $\mathbf{T}^f$ . Furthermore, the stress of the solid skeleton  $\mathbf{T}^s$  is the result of the weighted liquid pressure and the extra stress. The extra stress has to be formulated as a constitutive equation, relating the extra stresses to the strain of the solid skeleton. In particular for geotechnical applications the extra stress is depicted as effective stress. According to a history review about the development of effective stresses by de Boer and Ehlers [25], the concept of effective stresses can be traced back to Fillunger and Terzaghi [93]. The Cauchy stress of the solid constituent can be written as

$$\mathbf{T}^s = \mathbf{T}_E^s - n^s p \mathbf{I}, \quad (3.82)$$

where  $p$  represents the fluid pressure and  $\mathbf{T}_E^s$  is the solid extra stress. The Cauchy stress of the fluid constituent reads

$$\mathbf{T}^f = -(1 - n^s) p \mathbf{I}. \quad (3.83)$$

As mentioned earlier the extra stress of the solid is prescribed by a constitutive relation. Using an elastic material behaviour the extra stress of the solid constituent is given as

$$\mathbf{T}_E^s = \tilde{\mathbf{T}}_E^s + (1 - \alpha_{\text{BW}}) p \mathbf{I}, \quad (3.84)$$

with  $\tilde{\mathbf{T}}_E^s$  depicting the stress of the solid skeleton and the latter part describing the deformation of the grains of the granular porous skeleton. The parameter  $\alpha_{\text{BW}} = 1 - \frac{K}{K^s}$  is the so-called Biot-Willis parameter [11], accounting for the stress resulting from the deformation of the solid grains, where  $K$  and  $K^s$  are the bulk modulus of the dry solid skeleton and the bulk modulus of the solid grains, respectively. Combining Eqs.(3.81-3.84) it is obtained

$$\mathbf{T} = \tilde{\mathbf{T}}_E^s - \alpha_{\text{BW}} p \mathbf{I}. \quad (3.85)$$

The Cauchy stress of the mixture is further simplified to

$$\mathbf{T} = \mathbf{T}_E^s - p \mathbf{I}, \quad (3.86)$$

if incompressibility of the solid grains, i.e.  $K^s \rightarrow \infty$ , is assumed. This leads to  $\alpha_{\text{BW}} = 1$  and  $\tilde{\mathbf{T}}_E^s = \mathbf{T}_E^s$ , cf. Steeb and Renner [84].

### 3.5.2 Linear elastic solid skeleton

Linear elasticity is the most simple way to describe the mechanical properties of the solid skeleton. To obtain the well-known linear elastic equation for the solid skeleton, the standard procedure for evaluation of the balance equations by Coleman and Noll [21] is employed. Following Steeb and Diebels [80] or de Boer [13], the free Helmholtz energy, which describes the required energy to reach equilibrium of a system, can be written as

$$\Psi^s(\varepsilon_s) = \frac{1}{2} \lambda \text{tr}(\varepsilon_s)^2 + \mu \text{tr}(\varepsilon_s^2), \quad \text{with} \quad \mathbf{T}_E^s = \frac{\partial \Psi^s}{\partial \varepsilon_s}, \quad (3.87)$$

with the Lamé parameters  $\lambda$  and  $\mu$  and the linearised strain of the solid constituent  $\varepsilon_s$ . In this case the constitutive equation for the extra stress of the solid skeleton is

$$\mathbf{T}_E^s = \lambda \text{tr}(\varepsilon_s) \mathbf{I} + 2\mu \varepsilon_s. \quad (3.88)$$

### 3.5.3 Plastic deformations of the solid skeleton

The constitutive theory of plasticity allows to describe, in addition to linear elastic deformations, also plastic deformations, i.e. permanent deformations that occur when the solid skeleton of the material body does not fully recover after a cycle of loading and unloading, but remains irreversibly deformed. This means that, in contrast to the linear elastic framework, a unique mapping between the strain and the stress of a solid skeleton is not existing. The strain state of the solid skeleton depends, in addition to the current loading, on its history.

The theory of plasticity is very well developed and represented in literature (e.g. Simo and Hughes [79], Hill [40], Schröder [74], Betten [6], and Bertram [5]) and will be not discussed intensively in this contribution. The framework of modelling plastic deformations of multi-phase materials was e.g. described by Bluhm *et al.* [12] and de Boer [13].

In order to describe the material behaviour of a one-phase isotropic material e.g. steel, it is often assumed that small deformations are linear elastic (reversible) whereas large deformations lead to plastic effects. This differentiation is not a priori given for granular porous materials with a very small cohesion, as described in this contribution. For those materials, also small deformations might lead to plastic effects. Thus, here the framework of small deformations is combined with a plastic formulation.

For application of an elasto-plastic material behaviour usually an additive decomposition of the strain of the solid constituent is performed

$$\varepsilon_s = \varepsilon_s^{\text{el}} + \varepsilon_s^{\text{pl}}, \quad (3.89)$$

where  $\varepsilon_s^{\text{el}}$  describes the elastic and  $\varepsilon_s^{\text{pl}}$  the plastic part of the strain of the solid constituent  $\varphi^s$ . The same concept is applied to the rates of the corresponding strains

$$\dot{\varepsilon}_s = \dot{\varepsilon}_s^{\text{el}} + \dot{\varepsilon}_s^{\text{pl}}. \quad (3.90)$$

The constitutive law of linear elastic deformation of the solid skeleton reads

$$\mathbf{T}_E^s = \overset{4}{\mathbf{C}} : \varepsilon_s^{\text{el}}, \quad (3.91)$$

with  $\overset{4}{\mathbf{C}}$  being the elastic fourth order stiffness tensor.

The additive decomposition of the strain tensor (Eq. (3.89)) shows how deformations are interpreted within the framework of plasticity. If a uni-axial load, which is small enough, is applied on a material body, its solid skeleton deforms first in a reversible elastic way. After a certain limit, the so-called yielding point, the material behaviour changes and permanent plastic deformations arise. Transferring the concept of the yielding point into three dimensions, the plastic behaviour is characterized by the yielding function, which is a convex surface if plotted in principal stress space, cf. Figure 3.2. Deformations, which are within the yield surface, are elastic. As soon as the stress state of a material body reaches the yield surface, it starts yielding, which means that stress state beyond the yield surface is not physical.

If a cyclic loading is applied inducing plastic deformations, the physics of the deformed material might change. In case of granular porous media, the coordination number increases and the relative density decreases due to plastic deformations. This means the material behaviour will also change after each cycle where plastic deformations will be reached. To account for this phenomenon a so-called hardening rule is defined, which can be traced back to the process of isotropic or kinematic hardening.

For a physical interpretation of the material behaviour, a failure surface is introduced, similar to the yield surface, as a surface in principal stress space, which is initially larger than the yield surface. Failure of the observed material due to plastic deformation occurs if the yield surface reaches the failure surface. If the position of the yield surface is changed between single load cycles, by a rigid motion of the yield surface inducing a hardening (or softening) of the material, the process is called kinematic hardening. In case of isotropic hardening, the yield surface is growing whereas its shape is remaining. However, this contribution is focussed on transient and not on cyclic processes. Therefore, hardening phenomena are not investigated in the following.

Here, an associated flow rule is used, which means the function of the yield surface  $F$  is identical to the plastic potential  $Q$  ( $Q = F$ ). With this assumption, the plastic part of the strain rate

$$\dot{\varepsilon}_s^{\text{pl}} = \dot{\lambda} \frac{\partial F}{\partial \mathbf{T}_E^s} \quad (3.92)$$

is related to  $\lambda$ ,  $F$ , and  $\mathbf{T}_E^s$ . The plastic multiplier  $\lambda$  is determined applying the Karush-Kuhn-Tucker conditions [52], which is a set of inequality equations

$$F \leq 0, \quad (3.93)$$

$$\dot{\lambda} \geq 0, \quad (3.94)$$

$$F\lambda = 0, \quad (3.95)$$

that have to be fulfilled. The increment of the plastic multiplier  $\dot{\lambda}$  is calculated from the consistency condition

$$\dot{F} \dot{\lambda} = 0, \quad (3.96)$$

which itself is a result of the Karush-Kuhn-Tucker conditions [79]. Whereas the stress increment  $\dot{\mathbf{T}}_E^s$  is written as

$$\dot{\mathbf{T}}_E^s = \overset{4}{\mathbf{C}} : \dot{\epsilon}_s - \dot{\lambda} \overset{4}{\mathbf{C}} : \frac{\partial F}{\partial \mathbf{T}_E^s}. \quad (3.97)$$

Combining the consistency Eq. (3.96) with the definition of the strain increment, we obtain an expression for the increment of the plastic multiplier  $\dot{\lambda}$ , which reads

$$\dot{\lambda} = \frac{\left( \frac{\partial F}{\partial \mathbf{T}_E^s} \right)^T : \overset{4}{\mathbf{C}} : \dot{\epsilon}_s}{\left( \frac{\partial F}{\partial \mathbf{T}_E^s} \right)^T : \overset{4}{\mathbf{C}} : \frac{\partial F}{\partial \mathbf{T}_E^s}}. \quad (3.98)$$

In order to achieve a constitutive relation of elasto-plastic material behaviour, which has a similar structure like the elastic constitutive law in Eq. (3.91), Eq. (3.98) is inserted in Eq. (3.97), which leads to

$$\dot{\mathbf{T}}_E^s = \left( \overset{4}{\mathbf{C}} - \frac{\overset{4}{\mathbf{C}} : \frac{\partial F}{\partial \mathbf{T}_E^s} \otimes \left( \frac{\partial F}{\partial \mathbf{T}_E^s} \right)^T : \overset{4}{\mathbf{C}}}{\left( \frac{\partial F}{\partial \mathbf{T}_E^s} \right)^T : \overset{4}{\mathbf{C}} : \frac{\partial F}{\partial \mathbf{T}_E^s}} \right) : \dot{\epsilon}_s. \quad (3.99)$$

Following the similarity to the elastic constitutive law, cf. Eq. (3.91), the elasto-plastic stiffness tangent  $\overset{4}{\mathbf{C}}^{\text{ep}}$  is written as

$$\overset{4}{\mathbf{C}}^{\text{ep}} = \overset{4}{\mathbf{C}} - \frac{\overset{4}{\mathbf{C}} : \frac{\partial F}{\partial \mathbf{T}_E^s} \otimes \left( \frac{\partial F}{\partial \mathbf{T}_E^s} \right)^T : \overset{4}{\mathbf{C}}}{\left( \frac{\partial F}{\partial \mathbf{T}_E^s} \right)^T : \overset{4}{\mathbf{C}} : \frac{\partial F}{\partial \mathbf{T}_E^s}}. \quad (3.100)$$

In the framework of mechanized tunnelling materials, the application of the proposed model is adapted to the usability of cement-free mortars and is therefore restricted to sandy materials. Therefore, a Drucker-Prager soil plasticity model is used. For the numerical modelling of soil plasticity a yield surface is defined. In case of the Drucker-Prager criterion [27] the definition of the yield surface  $F$  reads

$$F = \sqrt{J_2} + \alpha_{\text{DP}} I_1 - k_{\text{DP}}, \quad (3.101)$$

with the negative second deviatoric stress invariant  $J_2$ , the first invariant  $I_1$  of the Cauchy extra stress tensor  $\mathbf{T}_E^s$ , and the material parameters  $\alpha_{\text{DP}}$  and  $k_{\text{DP}}$ . The

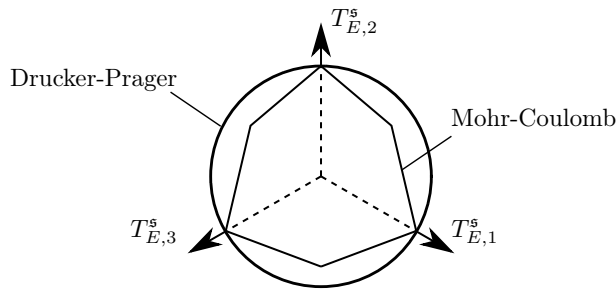


Figure 3.2: Yield surface according to Mohr-Coulomb and Drucker-Prager criterion, illustrated in the plane created by the principal-extra stresses  $T_{E,1}^s$ ,  $T_{E,2}^s$ ,  $T_{E,3}^s$  (adapted from [108]).

invariants are defined as

$$I_1 = \text{tr}(\mathbf{T}_E^s), \quad (3.102)$$

$$J_2 = \frac{1}{2} [\text{dev}(\mathbf{T}_E^s) : \text{dev}(\mathbf{T}_E^s)]. \quad (3.103)$$

For a physical interpretation, the material parameters of the Drucker-Prager criterion are matched to the ones of the Mohr-Coulomb criterion [53]. For the general case it can be written according to Yu [108] as

$$\alpha_{\text{DP}} = \frac{2 \sin \phi_{\text{MC}}}{\sqrt{3} (3 - \sin \phi_{\text{MC}})}, \quad (3.104)$$

$$k_{\text{DP}} = \frac{6 c_{\text{MC}} \cos \phi_{\text{MC}}}{\sqrt{3} (3 - \sin \phi_{\text{MC}})}. \quad (3.105)$$

Assuming plane-strain, the conversion reads

$$\alpha_{\text{DP}} = \frac{\tan \phi_{\text{MC}}}{\sqrt{9 + 12 \tan^2 \phi_{\text{MC}}}}, \quad (3.106)$$

$$k_{\text{DP}} = \frac{3 c_{\text{MC}}}{\sqrt{9 + 12 \tan^2 \phi_{\text{MC}}}}, \quad (3.107)$$

with the cohesion  $c_{\text{MC}}$  and the angle of internal friction  $\phi_{\text{MC}}$ . The criterion of Drucker-Prager leads to a cone-shaped yield surface, if plotted in the principal stress space, cf. Figure 3.2. However, the yield surface collapses to the one of the von Mises criterion [104], with a cylindrical-shaped yield-function in case that the material parameter  $\alpha_{\text{DP}}$  is zero.

### 3.5.4 Darcy's filter law

For the derivation of Darcy's filter law the local partial balance of momentum, cf. Eq.(3.45), of a fluid constituent  $\varphi^f$  is used, which leads to

$$\rho^{fR} \mathbf{a}_f - \operatorname{div} \mathbf{T}^f = \rho^{fR} \mathbf{b}^f + \hat{\mathbf{p}}^f, \quad (3.108)$$

with the Cauchy-stress of the fluid  $\mathbf{T}^f$  and the direct momentum production of the fluid  $\hat{\mathbf{p}}^f$ . For geotechnical applications it is convenient to assume laminar flow, where inertia plays a minor role, i.e.  $\mathbf{a}_f \approx \mathbf{0}$ . The balance of momentum in Eq. (3.108) reduces to

$$-\operatorname{div} \mathbf{T}^f = \rho^{fR} \mathbf{b}^f + \hat{\mathbf{p}}^f. \quad (3.109)$$

According to Ehlers and Bluhm [30] the direct momentum production and the Cauchy stress of the fluid are rewritten as

$$\hat{\mathbf{p}}^f = p \operatorname{grad} \phi + \hat{\mathbf{p}}_E^f, \quad (3.110)$$

$$\mathbf{T}^f = -\phi p \mathbf{I} + \mathbf{T}_E^f, \quad (3.111)$$

with the extra part of the direct momentum production  $\hat{\mathbf{p}}_E^f$  and the extra part of the Cauchy stress of the fluid  $\mathbf{T}_E^f$ .

Following Ehlers and Bluhm [30], the impact of the latter terms is determined by the characteristic length of the considered application. In configurations with a small characteristic length, the Cauchy-stress of the fluid  $\mathbf{T}_E^f$  can be neglected, whereas in problems with large characteristic lengths (e.g. pipe flow) the direct momentum production of the fluid  $\hat{\mathbf{p}}^f$  plays a minor role. In granular porous media we deal with small characteristic lengths (pore size). Thus, a vanishing extra stress of the fluid,  $\mathbf{T}_E^f = \mathbf{0}$ , is assumed.

As discussed in section 3.5.1, the extra quantities have to be determined by constitutive relations. Again, we follow Ehlers and Bluhm [30], interpreting the direct momentum production as a volume average of the local interaction forces resulting from friction between the solid skeleton and the pore fluid. Therefore, the extra quantity of the fluid momentum production reads

$$\hat{\mathbf{p}}_E^f = -\frac{\phi^2 \eta^{fR}}{k^s} \mathbf{w}_f, \quad (3.112)$$

where the intrinsic permeability of the solid constituent is denoted as  $k^s$  and  $\eta^{fR}$  represents the effective dynamic viscosity of the fluid constituent. Inserting Eq. (3.112) and Eq. (3.110) in Eq. (3.109) and using the definition of the filter velocity in Eq. (3.22) it is obtained

$$\mathbf{q} = -\frac{k^s}{\eta^{fR}} \left( \operatorname{grad} p - \frac{\rho^{fR} \mathbf{b}^f}{\phi} \right), \quad (3.113)$$

or neglecting body forces

$$\mathbf{q} = -\frac{k^s}{\eta^{jR}} \text{grad } p, \quad (3.114)$$

which represents the well-known semi-analytical formulation for the fluid velocity or filter velocity derived by Darcy [46].

## 3.6 Numerical realization

The derivation of a multi-phase model using the balance equations of the TPM and capturing transient effects results generally in non-linear coupled Partial Differential Equations (PDE's). The problem description by means of these PDEs is called strong form because the solution of this system of equations requires that the equations have to be fulfilled at each point of the considered domain. The equations mostly can not be solved analytically. Therefore, numerical methods are used in order to obtain an approximated solution of the governing field equations. In this contribution the numerical solution is gained by the Finite Element Method (FEM). The FEM was developed for structural problems and later extended to multi-field simulations. It has reached crucial importance in many engineering fields and, thus, it is the main topic of different textbooks. To mention only few, there are contributions of Klein [51], Link [56], Jung and Langer [47], Merkel and Öchser [59], Hughes [42], and Steinke [59].

For a short overview, the numerical approach is derived for the solution of the poroelastic model of Biot [10], which can be also found in publications of Zheng *et al.* [109] and Cui *et al.* [23]. Using the TPM, a two phase domain represented by the constituents  $\varphi^\alpha$ , with  $\alpha = \{\mathfrak{s}, \mathfrak{f}\}$  are considered. The set of poroelastic equations is derived from the partial local balance equations. In particular, the partial local balance of mass, cf. Eq. (3.37) is used for both constituents  $\alpha = \{\mathfrak{s}, \mathfrak{f}\}$  and subsequently summed up in order to obtain the balance equation for the mixture. Additionally, the local balance of momentum of the mixture, cf. Eq. (3.48), assuming rigid grains is used. Thus, the poroelastic equations in their strong form read

$$\text{div } \mathbf{T} = \mathbf{0}, \quad (3.115)$$

$$\text{div } \mathbf{q} + \text{div } \mathbf{v}_s = 0. \quad (3.116)$$

For the numerical approximation of the field equations, first weak forms are derived from the strong form formulation, cf. Eq. (3.115, 3.116). Hence, the strong form of a field equation is multiplied with a test function and integrated in space. In case of the strong form represented by the balance of momentum of the mixture, cf. Eq. (3.115), it is obtained

$$\int_{\mathcal{B}} \text{div}(\mathbf{T}) : \delta \mathbf{u} \, d\mathcal{B} = 0. \quad (3.117)$$

Using the identity

$$\int_{\mathcal{B}} \operatorname{div}(\mathbf{T} \cdot \delta \mathbf{u}) \, d\mathcal{B} = \int_{\mathcal{B}} \operatorname{div}(\mathbf{T}) \cdot \delta \mathbf{u} \, d\mathcal{B} + \int_{\mathcal{B}} \mathbf{T} : \operatorname{grad}(\delta \mathbf{u}) \, d\mathcal{B}, \quad (3.118)$$

and the relation for the linearised strain  $\operatorname{grad}(\delta \mathbf{u}) = \delta \varepsilon$  the weak form in Eq. (3.117) is rewritten as

$$0 = \int_{\mathcal{B}} \operatorname{div}(\mathbf{T}) \cdot \delta \mathbf{u} \, d\mathcal{B} = \int_{\mathcal{B}} \operatorname{div}(\mathbf{T} \cdot \delta \mathbf{u}) \, d\mathcal{B} - \int_{\mathcal{B}} \mathbf{T} : \delta \varepsilon \, d\mathcal{B}. \quad (3.119)$$

Next, the theorem of Cauchy, cf. Eq. (3.42), and the divergence-theorem, cf. Eq. (3.43), are applied, leading to

$$\int_{\mathcal{B}} \mathbf{T} : \delta \varepsilon \, d\mathcal{B} = \int_{\Gamma_u} \operatorname{div}(\mathbf{t} \cdot \delta \mathbf{u}) \, d\Gamma_u. \quad (3.120)$$

In Eq. (3.120) the weak form of the local balance of momentum of the mixture is given. The term on the left hand side has to be fulfilled weakly within the considered domain  $\mathcal{B}$ . The term on the right hand side (rhs) of the equation has to be fulfilled on the surface boundary  $\Gamma_u$  of the domain. This is representing the Neumann boundary condition. If the Neumann or Dirichlet boundary condition is applied separately within a commercial finite element software, then the rhs of Eq. (3.120) is not considered for the implementation of the weak form.

In a way similar to the balance of momentum of the solid phase, also the local balance of mass of the mixture, cf. Eq. (3.116) is transferred into the weak form by multiplication with a test function and integrating in space. Thus, it can be written

$$\int_{\mathcal{B}} \delta p \, \mathbf{q} \, d\mathcal{B} + \int_{\mathcal{B}} \delta p \operatorname{div} \mathbf{v}_s \, d\mathcal{B} = 0. \quad (3.121)$$

Using the identity

$$\int_{\mathcal{B}} \operatorname{div}(\delta p \, \mathbf{q}) \, d\mathcal{B} = \int_{\mathcal{B}} \delta p \operatorname{div} \mathbf{q} \, d\mathcal{B} + \int_{\mathcal{B}} \operatorname{grad} \delta p \cdot \mathbf{q} \, d\mathcal{B}, \quad (3.122)$$

and the relation  $\operatorname{grad} \delta p = \delta \operatorname{grad} p$ , Eq. (3.121) becomes

$$\int_{\mathcal{B}} \operatorname{div}(\delta p \, \mathbf{q}) \, d\mathcal{B} - \int_{\mathcal{B}} \delta \operatorname{grad} p \cdot \mathbf{q} \, d\mathcal{B} + \int_{\mathcal{B}} \delta p \operatorname{div} \mathbf{v}_s \, d\mathcal{B} = 0. \quad (3.123)$$

Again, the divergence-theorem, cf. Eq. (3.43), is applied for the first term of Eq. (3.123), and additionally, the relation  $\mathbf{v}_s = \partial_t \mathbf{u}_s$  is used, which leads to

$$\int_{\mathcal{B}} \delta \operatorname{grad} p \cdot \mathbf{q} \, d\mathcal{B} - \int_{\mathcal{B}} \delta p \operatorname{div}(\partial_t \mathbf{u}_s) \, d\mathcal{B} = \int_{\Gamma_q} (\delta p q) \cdot \mathbf{n} \, d\Gamma_q, \quad (3.124)$$

with the surface boundary  $\Gamma_q$ . The Eq. (3.124) represents the weak form of the local mass balance of the mixture. With similar argumentation, as in case of the weak form of the balance of momentum of the mixture, the rhs has to be fulfilled on the boundary surface  $\Gamma_q$  and thus can be replaced by boundary conditions within a commercial finite element software.

Furthermore, Darcy's law, cf. Eq. (3.114), the concept of effective stresses, cf. Eq. (3.86) and the linear elastic constitutive assumption, cf. Eq. (3.88) is applied. To close the problem described by Eqs.(3.120, 3.124), initial and boundary conditions are prescribed. In case of the poroelastic approach the initial conditions are

$$p = p_0, \quad \mathbf{u}_s = \mathbf{u}_{s,0}, \quad \forall \mathbf{x} \in \mathcal{B}_0 \times t. \quad (3.125)$$

The initial conditions are valid for the reference configuration of the considered body  $\mathcal{B}_0$ . For each considered field, boundary conditions have to be chosen to close the system of equations and, therefore, to be able to compute a solution. The boundary conditions are defined on the surface boundary  $\partial\mathcal{B}$ , which is composed of the Neumann boundary  $\Gamma_N$  and the Dirichlet boundary  $\Gamma_D$ , with the constraints  $\partial\mathcal{B} = \Gamma_N \cup \Gamma_D$  and  $\Gamma_N \cap \Gamma_D = \emptyset$ . The boundary conditions are defined as

$$q = \mathbf{q} \cdot \mathbf{n} = \bar{q}, \quad \forall \mathbf{x} \in \Gamma_N^p \times t, \quad \mathbf{T} \cdot \mathbf{n} = \bar{\mathbf{t}}, \quad \forall \mathbf{x} \in \Gamma_N^{\mathbf{u}_s} \times t, \quad (3.126)$$

$$p = \bar{p}, \quad \forall \mathbf{x} \in \Gamma_D^p \times t, \quad \mathbf{u}_s = \bar{\mathbf{u}}_s, \quad \forall \mathbf{x} \in \Gamma_D^{\mathbf{u}_s} \times t. \quad (3.127)$$

After the derivation of the weak equations, cf. Eqs.(3.120, 3.124), the solution of the IBVP is obtained by solving the equations numerically, e.g, by means of the FEM. Therefore, the considered domain  $\mathcal{B}$  is discretised in space and time. In case of PDE's representing the field equations, the obtained system of equations cannot be solved using direct methods. Instead an iterative Newton-Raphson algorithm is used.



## Chapter 4

# Infiltration processes in cohesionless soils

*In this chapter, a thermodynamically consistent four-phase continuum model in the framework of the mixture theory is presented describing infiltration processes of suspensions in cohesionless granular material. The chapter focuses on the distinct form of the constitutive relation for the volume production term of the fluidized particles and its consequences on the infiltration process. To this end, a constitutive equation describing infiltration phenomena is proposed, which includes only one material parameter. We study numerically a boundary value problem, which is characterized by a homogeneous field of the hydraulic gradient in the reference configuration at time  $t_0 = 0$ . Infiltration affects the distribution of the hydraulic properties and illustrates the consequences of the proposed constitutive equation for specific parameter choices. Furthermore, it is shown how the material parameter can be estimated without explicit numerical calculations.*

### 4.1 Introduction

Infiltration processes are characterized by seepage flow of a complex fluid through a porous medium and a possible deposition process of the fines of the suspension. Complex fluids are mixtures of a liquid -mostly water- and small particles (fines) moving with the fluid. According to the necessities of the investigated infiltration process the velocity of the fines may be assumed identical to the fluid velocity.

The deposition of fines in the pore space of the porous medium results in considerable changes of the material properties of the porous medium. On the one hand, mechanical properties are changed. The structural stiffness is increased due to a reduction of pore space and additional material strength coming from the deposited fines - being part of the skeleton after deposition. On the other hand, hydraulic prop-

erties like the hydraulic conductivity and the effective viscosity of the particle-laden fluid are modified. Macroscopically, the reduced pore space leads to lower permeabilities as well as to a change of effective viscosities due to the phase change of the former fluidized fines.

Deposition is triggered/controlled in two ways: Hydraulic reasons trigger the process whereas geometrical properties on the microscale control the process. The geometrical requirements for a decomposition process can readily be taken e.g. from Terzaghi's filter laws [94] indicating that some of the fines of the particle-laden fluid cannot pass the constriction sizes of the porous medium. Once these requirements are met, larger deposition rates are achieved by a higher hydraulic gradient. Additionally taking sedimentation effects into account - which is not the case in the proposed model - also gravity forces in conjunction with a rather low hydraulic gradient increase the deposition rate.

Depending on the initial conditions of the porous medium and the complex fluid (pore constriction size distribution on the microscopical scale of the porous material, hydraulic gradient) there are basically two kinds of infiltration processes which should be distinguished. A steady going infiltration, where deposition of fines takes place rather slowly due to an initially big pore space and a rather low hydraulic gradient and secondly a rapid infiltration, which is caused by a high hydraulic gradient and initially small constriction sizes leading to a highly localized clogging effect. Clogging effects during infiltration are very well known in various applications. Mainly, we distinguish between so-called external and internal filter cakes due to clogging phenomena, cf. Figure 4.5.

Besides various possible applications for the proposed model, such as hardening of soils in mines or land improvements, the authors' main focus is on the field of mechanized tunneling. Due to technical reasons during a typical excavation process of a tunnel lining, a gap is opening between the lining and the surrounding soil. This gap contributes significantly to a change in the mechanical parameters of loose soil, which leads to unwanted subsidence at the surface. Hence, it is desirable to close the gap created by the system of tubing. To this end the so-called backfilled grout mortar is injected. During the tunneling process distinct material properties of the backfilled grout mortar are needed. First, the mortar should have a good flowability to ensure mechanical processing and transporting of the mortar through the pipelines. As soon as the mortar is in its final position, a rapid hardening is required, which allows to reproduce the primary stress state of the surrounding soil, so that surface subsidence are minimized. The respective strength can be achieved by additives, which cause a hardening process of the mortar. A cheaper and environmentally more friendly approach is to dispense largely with cement portions and to drain the mortar via a high-pressure injection process instead. During this procedure a consolidation process of the mortar takes place, which causes a transport of the mortar's pore fluid into the surrounding soil, so that the mortar is transformed into a solid, gap-filling structure.

## 4.2 Governing equations of infiltration processes

Fig. 4.1 sketches the characteristic microstructure of a fluid-saturated granular medium, which we investigate in the current contribution. The principal material properties are caused by the complex pore fluid which itself is a mixture of a pore liquid and fine-grained particles. Due to drag forces, the complex fluid, i.e. the suspension, could be transported through the porous skeleton or, if the constriction sizes of the pore spaces are too small, the fines are blocked in the pore constriction sizes. Obviously, this local blocking leads to an evolution of the hydromechanical properties of the material. In this contribution, we propose a macroscopic model which is able to predict the evolution of the intrinsic permeability and porosity of the skeleton and therefore could be used for predicting numerically infiltration processes.

In contrast to extensively-discussed poroelastic models describing the hydraulic and mechanical behaviour of soils, cf. Biot [10], Coussy [22], we desire the hydraulic infiltration model by the thermodynamically-consistent Theory of Porous Media (TPM) [10, 16, 17, 24, 30], which could be regarded as an extension of the mixture theory, cf. Truesdell [99].

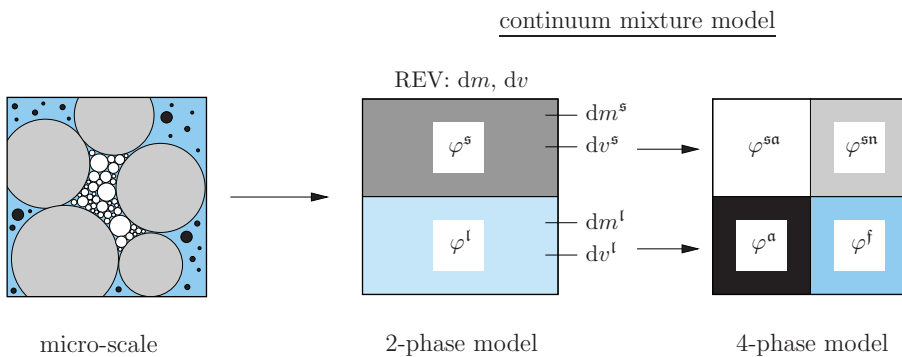


Figure 4.1: Microscale and RVE of a fully-saturated soil and the corresponding four-phase continuum model, from [71, 82].

Since the fluid is a suspension, two constituents have been introduced to describe its hydraulic behaviour in further detail. These are the pore fluid represented by  $\varphi^f$  and the dissolved particles represented by  $\varphi^a$ . The evolution of the fabric of the solid skeleton is modelled by a stable fabric  $\varphi^{sn}$  and the fines  $\varphi^{sa}$ , which are blocked in the pore space. Thus, a liquid-solid phase transition process is taken into account. Related to the current conditions fines can either behave fluid-like (described by constituent  $\varphi^a$ ) or solid-like, (described by constituent  $\varphi^{sa}$ ). This phase transition process will be taken into account in the present model by a mass/volume production term in the corresponding partial mass/volume balances of the constituents  $\varphi^a$  and  $\varphi^{sa}$ , cf. Eq. (4.10). Altogether, we observe four participating constituents  $\varphi^\alpha$  with  $\alpha = \{f, a, sn, sa\}$ , cf Fig. 4.1.

The macroscopic modelling idea i.e. the split in stable and unstable constituents, traces back to ideas of Vardoulakis [101] and Steeb & Diebels [80] describing the evolution of the fabric in the context of internal erosion. Nevertheless, the specific constitutive relation, which are the driving forces for the evolution of the fabric, has not been investigated for infiltration phenomena. If the concentration of the fines is low and if the density contrast between the fines and the pore fluid is not too high, we observe that the velocity of the fines  $\mathbf{v}_a$  and of the pore fluid  $\mathbf{v}_f$  is almost identical, i.e.  $\mathbf{v}_a = \mathbf{v}_f$ .

In a certain Representative Volume Element (RVE) with the volume  $dv$ , cf. Fig. 4.1, the volume fractions of the single constituents  $\varphi^\alpha$  are defined as

$$n^\alpha = \frac{dv^\alpha}{dv}. \quad (4.1)$$

The partial density  $\rho^\alpha$  is defined as the ratio between the mass  $dm^\alpha$  of the phase  $\varphi^\alpha$  with respect to the total volume  $dv$  of the RVE, which leads to a relation between partial densities  $\rho^\alpha$  and effective densities  $\rho^{\alpha R}$ , the latter one being the ratio between  $dm^\alpha$  and the actual volume of the phase  $dv^\alpha$

$$\rho^\alpha = \frac{dm^\alpha}{dv} = \frac{dm^\alpha}{dv^\alpha} \frac{dv^\alpha}{dv} = \rho^{\alpha R} n^\alpha. \quad (4.2)$$

As the 4-phase model is an extension of a previously discussed 3-phase model for application in internal erosion, cf. [80], we briefly sketch the modelling framework. Due to the so-called saturation condition

$$\sum_{\alpha} n^\alpha = 1 \quad \rightsquigarrow \quad n^\alpha \leq 1 \quad \rightsquigarrow \quad \rho^\alpha \leq \rho^{\alpha R}, \quad (4.3)$$

the value of the partial density is always smaller than the value of the effective one.

The main part of the proposed model is the mass balance of the four phases. In the general introduction of this contribution, cf. section 3.3.1 the partial local mass balance was already discussed. In this part the definition is shortly repeated and afterwards used for the derivation of a particular multi-field approach. Following Ehlers & Bluhm [30], de Boer [24] and Steeb [82], the local form of the partial balance of mass is given as

$$(\rho^\alpha)'_{\alpha} + \rho^\alpha \operatorname{div} \mathbf{v}_\alpha = \hat{\rho}^\alpha, \quad (4.4)$$

whereas a constraint for the mixture mass production  $\sum_{\alpha} \hat{\rho}^\alpha = 0$  for thermodynamically closed systems guarantees that there is no mass production in the total mixture  $\varphi = \bigcup_{\alpha} \varphi^\alpha$ , being the assembly of all single phases. Since the partial density is given in a spatial description, the material time derivative  $(\rho^\alpha)'_{\alpha}$  is expressed by the local

and the convective parts

$$(\rho^\alpha)'_\alpha = \frac{\partial \rho^\alpha}{\partial t} + \text{grad } \rho^\alpha \cdot \mathbf{v}_\alpha = \partial_t (\rho^\alpha) + \text{grad } \rho^\alpha \cdot \mathbf{v}_\alpha. \quad (4.5)$$

Furthermore, we assume that the constituents  $\varphi^\alpha$ ,  $\varphi^{\text{sn}}$  the fluid constituent  $\varphi^{\text{f}}$  and the solid skeleton  $\varphi^{\text{sn}}$  are materially incompressible. Note that the evolution of the porosity  $\phi = 1 - n^{\text{s}}$  in a certain RVE is then described through the deposition process of fines  $n^{\text{sa}}$ , i.e.  $\phi = 1 - n^{\text{s}} = 1 - n^{\text{sn}} - n^{\text{sa}}$ . Note, that the partial density of the solid skeleton is also not a constant parameter as it depends on the porosity, i.e.  $\rho^{\text{s}} = (1 - \phi) \rho^{\text{sR}}$ . Therewith we can reformulate the mass balance into

$$\partial_t (\rho^\alpha) + \text{div}(\rho^\alpha \mathbf{v}_\alpha) = \hat{\rho}^\alpha. \quad (4.6)$$

Applying the definition of the partial density Eq. (4.2) and constant effective densities  $\rho^{\alpha R} = \rho_0^{\alpha R}$ , we obtain

$$\partial_t (n^\alpha \rho^{\alpha R}) + \text{div}(n^\alpha \rho^{\alpha R} \mathbf{v}_\alpha) = \hat{\rho}^\alpha = \hat{n}^\alpha \rho^{\alpha R}. \quad (4.7)$$

Note, that the partial density exchange rate  $\hat{\rho}^\alpha$  is split into a part depending on the effective density and a volume-driven exchange rate  $\hat{n}^\alpha$ . If the effective density is constant, which will be the case for a material incompressible constituent  $\varphi^{\alpha R}$ , the partial balance of mass is reduced to a partial volume balance

$$\partial_t (n^\alpha) + \text{div}(n^\alpha \mathbf{v}_\alpha) = \hat{n}^\alpha. \quad (4.8)$$

In the second part of this chapter we will mainly discuss the influence of the constitutively determined rate of volumetric mass exchange  $\hat{n}^\alpha$  [1/s] in more detail. Before we formulate the specific mass balances we discuss some of the assumptions, which we introduce to simplify the hydromechanically-driven infiltration process. Obviously, the attached fines and the primary fabric move with the same solid velocity  $\mathbf{v}_s = \mathbf{v}_{\text{sn}} = \mathbf{v}_{\text{sa}}$ . Furthermore, we state that there is no relative movement between fluid and fluidized particles, which can be written as  $\mathbf{v}_l = \mathbf{v}_a = \mathbf{v}_f$ . Hence, we introduce the relative fluid velocity with respect to the solid phase, i.e. the seepage velocity  $\mathbf{w}_f$ , for the purpose of materially objective constitutive equations  $\mathbf{w}_f = \mathbf{w}_a = \mathbf{v}_f - \mathbf{v}_s$ . In a next step, we introduce new field variables that are more suitable for physical interpretations. Thus, we introduce the porosity field  $\phi(\mathbf{x}, t)$ , the amount of attached fines  $a(\mathbf{x}, t)$  which is related to the solid phase, and the volumetric concentration

$c(\mathbf{x}, t)$  of the fluidized fines in the liquid suspension.

$$\begin{aligned}
 \phi &= n^f + n^a, \\
 n^s &= n^{sn} + n^{sa} = 1 - \phi, \\
 a &= \frac{n^{sa}}{n^s}, \\
 c &= \frac{n^a}{\phi}.
 \end{aligned} \tag{4.9}$$

### 4.2.1 Mass balances

As already mentioned in the previous sections, the transformation of state of the fluidized fines into an attached particle is modelled via the rate of mass exchange  $\hat{n}^\alpha$  between the phases  $\varphi^{sa}$  and  $\varphi^a$ . The production of attached fines is equal to the reduction of fluidized particles in the RVE. In the present chapter, we focus on the hydraulic influence of this infiltration processes. An evolution of mechanical properties like the stiffness of the porous skeleton is out of the scope. Thus, the deformation process of the skeleton will be neglected ( $\mathbf{u}_s = \mathbf{v}_s = \mathbf{0}$ ) leading to

$$\hat{n}^a = -\hat{n}^{sa} =: -\hat{n}^s. \tag{4.10}$$

The governing equations of the infiltration process are stated in the following. We start with the balance of mass of the mixture which is the sum of all partial mass balances Eq. (4.8). Transforming it using the definitions given above and the saturation constraint Eq. (4.3)

$$\partial_t \underbrace{(n^f + n^a + n^{sn} + n^{sa})}_1 + \sum_\alpha \operatorname{div}(n^\alpha \mathbf{v}_\alpha) = \sum_\alpha \underbrace{\hat{n}^\alpha}_0, \tag{4.11}$$

leads finally to

$$\operatorname{div} \mathbf{v}_s + \operatorname{div} \mathbf{q} = 0. \tag{4.12}$$

Note, that the vanishing right hand side in Eq. (4.11) is a result of vanishing mass productions  $\hat{\rho}^f$  and  $\hat{\rho}^{sn}$  and identical effective densities  $\rho^{\alpha R}$  of the phases  $\varphi^{sa}$  and  $\varphi^a$ . In the balance of mass of the mixture, the so-called filter velocity  $\mathbf{q} = \phi \mathbf{w}_f$ , has been introduced. The volume balance of porosity, i.e. of the liquid suspension  $\varphi^l$  is obtained by summing up the volume balance of the pore liquid  $\varphi^f$  and the volume balance of the fluidized fines  $\varphi^a$

$$\partial_t \phi + \operatorname{div} \mathbf{q} = \hat{n}^a. \tag{4.13}$$

Summing up the balance of volume of the primary fabric  $\varphi^{\text{sn}}$  and the balance of attached fines  $\varphi^{\text{sa}}$ , we obtain an evolution equation for the porosity

$$\partial_t \phi = \hat{n}^{\text{a}}. \quad (4.14)$$

The balance of volume of the attached fines  $\varphi^{\text{sa}}$  is similarly collapsing to an evolution equation for the amount of fines  $a(\mathbf{x}, t)$

$$\partial_t(a\phi) - \partial_t(a) = \hat{n}^{\text{a}}. \quad (4.15)$$

Later we will show, that both ordinary differential equations Eq. (4.14),(4.15) can be solved locally. The balance of volume of the fluidized fines  $\varphi^{\text{a}}$  in the suspension reads

$$\partial_t(c\phi) + \text{div}(c\mathbf{q}) = \hat{n}^{\text{a}}. \quad (4.16)$$

Summing up all local partial mass balance of the constituents  $\varphi^\alpha$  with  $\alpha = \{\mathbf{f}, \mathbf{a}, \mathbf{sa}, \mathbf{sn}\}$  we obtain the continuity equation of the mixture  $\varphi$

$$\text{div } \mathbf{q} = 0. \quad (4.17)$$

Note, we are able to reduce the set of microscale quantities from four to three ( $\phi, a, c$ ). The integration of the mass balance of the rigid primary fabric leads to

$$n^{\text{sn}} = n_0^{\text{sn}} (1 - \text{div } \mathbf{u}_s) = n_0^{\text{sn}}, \quad (4.18)$$

in which the partial volume  $n^{\text{sn}}$  can be expressed using the porosity  $\phi$  and the amount of attached fines  $a$

$$n^{\text{sn}} = (1 - \phi)(1 - a), \quad \text{and} \quad n_0^{\text{sn}} = (1 - \phi_0)(1 - a_0), \quad (4.19)$$

leading to

$$\phi = 1 - \frac{(1 - a_0)(1 - \phi_0)}{(1 - a)}, \quad (4.20)$$

which can be used to eliminate one dependent variable from the set of equations

$$a = a(\phi) = \frac{a_0(1 - \phi_0) + \phi_0 - \phi}{(1 - \phi)}. \quad (4.21)$$

The quasi-static balance of momentum of the fluid without volume forces, the balance of mass of the fluid and constitutive assumptions reveal the well-known Darcy relationship between the gradient of the fluid pressure and the filter velocity, cf. Ehlers & Bluhm [30]. Here  $\eta^{\text{LR}}$  is the effective dynamic viscosity of the particle-laden suspension depending on the amount of fluidized particles  $c(\mathbf{x}, t)$ .

$$\mathbf{q} = -\frac{k^s(\phi)}{\eta^{fR}(c)} \text{grad } p. \quad (4.22)$$

$k^s(\phi)$  is the intrinsic permeability of the porous fabric depending on the porosity  $\phi(\mathbf{x}, t)$ . For the considered case of cohesionless granular media, the intrinsic permeability  $k^s$  [m<sup>2</sup>] could be related to the grain size distribution function of the particle ensemble. Here, we calculate the permeability at the initial state  $k_0^s = k^s(\mathbf{x}, t_0)$  with the Kozeny-Carman equation, cf. Carrier [18]. The evolution of permeability  $k^s(\mathbf{x}, t)$  is related to the evolution of the porosity  $\phi(\mathbf{x}, t)$

$$k^s(\phi) = k_0^s \left[ \frac{\phi^3}{(1-\phi)^2} \right] \left[ \frac{(1-\phi_0)^2}{\phi_0^3} \right] \quad \text{and} \quad k_0^s = \frac{1}{C_1} \frac{\phi_0^3}{(1-\phi_0)^2} D_{eq}^2. \quad (4.23)$$

$C_1$  is the so-called Kozeny-Carman constant, cf. Irmay [46] or Ergun [34].  $D_{eq}$  is the equivalent particle diameter of the granular material. Einstein [33] proposed the evolution of the effective dynamic viscosity of a suspension. From an initial dynamic viscosity of a liquid  $\eta^{fR}$ , it could be calculated as a function of concentration

$$\eta^{fR}(c) = \eta^{fR} \left( 1 + \frac{5}{2} c \right). \quad (4.24)$$

It has to be noted that Eq. (4.24) has initially been proposed for dilute suspensions. For more sophisticated viscosity corrections, e.g. for dense suspensions, we refer to [26].

Thus, the following set of equations is remaining and is formulating the Initially Boundary Value Problem (IBVP) of infiltration:

$$\text{div} \left[ \frac{k^s(\phi)}{\eta^f(c)} \text{grad } p \right] = 0, \quad \forall \mathbf{x} \in \mathcal{B} \times t \quad (4.25)$$

$$\partial_t(c\phi) + \text{div} \left[ c \frac{k^s(\phi)}{\eta^f(c)} \text{grad } p \right] = \hat{n}^a, \quad \forall \mathbf{x} \in \mathcal{B} \times t \quad (4.26)$$

with boundary conditions for the flux  $\mathbf{q}$  and the flux of suspended particles  $c^*$  at the Neumann boundary  $\Gamma_N$  as well as the pressure  $p$  and the concentration of the suspended particles  $c$  at the Dirichlet boundary  $\Gamma_D$

$$q = \mathbf{q} \cdot \mathbf{n} = \bar{q}, \quad \forall \mathbf{x} \in \Gamma_N^p \times t, \quad c^* = c\bar{q}, \quad \forall \mathbf{x} \in \Gamma_N^c \times t, \quad (4.27)$$

$$p = \bar{p}, \quad \forall \mathbf{x} \in \Gamma_D^p \times t, \quad c = \bar{c}, \quad \forall \mathbf{x} \in \Gamma_N^c \times t. \quad (4.28)$$

Also the following initial conditions are used

$$p = p_0, \quad c = c_0, \quad \phi = \phi_0, \quad \forall \mathbf{x} \in \mathcal{B}_0 \times t. \quad (4.29)$$

The coupled nonlinear IBVP could be solved by numerical methods. Here, we use Galerkin-type finite element schemes, described by Steeb [83]. The primary variables are  $\mathcal{P} = \{p, c\}$ . The IBVP is completed, in combination with the evolution equation  $\partial_t \phi = \hat{n}^a$  and Eq. (4.21) for  $a(\mathbf{x}, t)$  and an appropriate constitutive equation for the rate of mass/volume production  $\hat{n}^a$ . The form of the latter equation will be focussed in the next section.

### 4.3 Constitutive equation for mass exchange

To close the IBVP, it is necessary to find a formulation for the volume exchange term, the so-called production term  $\hat{n}^a$ . The structure of the term is already known from previous publications, cf. [80, 82, 101]. In the context of the mathematical formulation of general internal remodelling phenomena described within the mixture theory by a mass production term, Steeb and Diebels [80] pointed out, that a thermodynamically consistent form of the constitutive equation for mass production reads

$$\hat{n}^a \propto |\mathbf{q}|. \quad (4.30)$$

Physically this expression is also evident. The higher the flow in a RVE, the more particles per time unit will pass the RVE. Hence, the probability of infiltration of individual particles or swarms of particles is higher. If we consider the limiting case of a vanishing velocity ( $\mathbf{q} = 0$ ), then also the value of the production term disappears. This fact can not be motivated physically, because for such a case of a vanishing fluid velocity one could observe sedimentation of fluidized particles. At least this model focuses on infiltration phenomena and sedimentation is not taken into account. However, it is readily possible to consider a relative movement of fines  $w_a \neq w_f$  and an additional expression in the production term to describe these phenomena.

As already described, the probability of infiltration increases with an increasing number of particles, which pass through the RVE per time unit. This may be a result from a higher flow rate or of a higher concentration of fluidized particles in the fluid. Following the above argumentation, the probability of infiltration increases with increasing concentration of fines  $c$ . Therefore, the production term may be written as  $\hat{n}^a \propto c |\mathbf{q}|$ . In this case for  $c = 0$ ,  $\hat{n}^a = 0$  is obtained. This relationship illustrates that infiltration can only take place if there are fluidized particles in the considered area.

To complete the expression for the production term a second parameter  $k$  is added. This parameter is a scalar value, which has to be determined by experimental investigations. Finally the complete production term can be written as

$$\hat{n}^a = -k c |\mathbf{q}|. \quad (4.31)$$

In the following section a numerical example will be analysed to illustrate the complete set of equations. Subsequently, the recently introduced parameter  $k$  will be discussed on the basis of the results of the numerical example.

## 4.4 Analysis of a 1-dim infiltration problem

The numerical solution of the IBVP will be explained in a 1-dim setting. The investigated volume is fully saturated with the four previously described phases  $\varphi^\alpha$ . Dirichlet boundary conditions for the pressure  $\bar{p}$  are chosen for the boundaries at  $x = 0$  m and  $x = L$ . This is done in a way, that a pressure gradient arises which initiates a fluid flow from the left to the right. In addition, a time-constant Dirichlet boundary condition for concentration  $c(x = 0)$ , i.e.  $\bar{c} = 0.1$  is prescribed. Within the domain an initial condition is used for the concentration, setting  $c_0(x) = 0.001$ . Thus, the porous medium is already saturated initially with a suspension. All four constituents are therefore present. The consequence of the present initial and boundary conditions is a concentration influx leading to concentration front passing through the domain from left to right. The boundary and initial conditions as described above are summarized in Fig. 4.2a). The time-scale of the simulation covers the duration of the concentration front propagation through the whole domain.

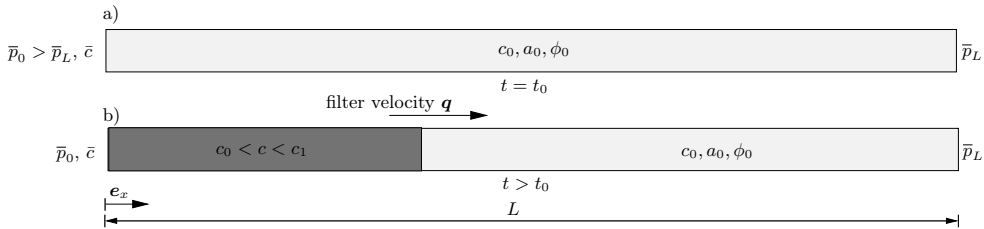


Figure 4.2: Infiltration process: a) initial and boundary conditions for the investigated domain; b) illustration of the concentration profile for  $t > t_0$ .

According to Fig. 4.3 the porosity  $\phi(x, t)$  is changing in space and time. Hence, parallel to the convective transport, an infiltration process takes place leading to a decrease of fluidized particles. This also indicates the smooth, gradual character of the infiltration process. The values describing the concentration  $c$  and the filter velocity of the fluid  $\mathbf{q}$  are at their maximum in the begin of the process. Although the Darcy velocity  $\mathbf{q}$  is influenced by the increase in viscosity, Eq. (4.24), and a decrease in permeability, Eq. (4.23), the latter physical phenomenon is dominating.

In contrast to classical seepage flow in porous media, the filter velocity  $\mathbf{q}$  of the front depends on the effective velocity which is a function of the concentration of fines. Furthermore, the permeability is also not constant in the domain and depends on the amount of infiltrated and deposited particles. Within the flow-through fine grained material is deposited. Furthermore, it is observed that the transport processes are

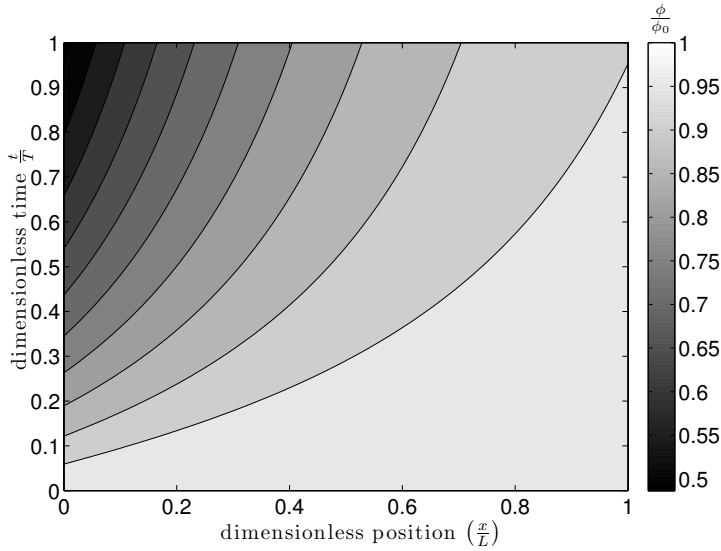


Figure 4.3: Contour plot describing the evolution of the porosity in space and time in the domain.

essentially driven by convection. Diffusion processes play only a minor role. This is concluded from the moving front (steep gradient of concentration).

Next, we discuss the evolution of concentration in detail. It has to be noted, that in the case  $t_{eq} > t_0$  an equilibrium concentration  $c_{eq}$  is reached. Microscopically, this process can be explained as follows: The concentration in a certain control volume is not changed while the local deposition is ongoing and the local permeability  $k^s$  is decreasing. The transport of the fine particle fraction of the domain causes a sudden change of the concentration in the transition zone. This sudden decrease of the concentration disappears as soon as the transition zone has passed the whole domain and arrived at the right boundary. If the infiltration process is considered beyond the

Length of domain	$L$	20	m
Pressure at boundary $x = 0$	$\bar{p}_0$	6.38	kPa
Pressure at boundary $x = L$	$\bar{p}_L$	0	Pa
Concentration at boundary $x = 0$	$\bar{c}$	0.1	
Effective dynamic viscosity	$\eta^{fR}$	1	mPa s
Initial porosity	$\phi_0$	0.32	
Initial intrinsic permeability	$k_0^s$	$8.57 \times 10^{-10}$	$\text{m}^2$
calculation time	$t$	$1 \times 10^5$	s

Table 4.1: Material properties and used boundary conditions.

flow-through of the transition zone, an equilibrium concentration setting is observed in the whole domain. In particular, the chosen parameter  $k$  in the evolution equation of the volume exchange term, has an influence on the time-independent equilibrium concentration. In Fig. 4.4 equilibrium concentrations of fines in the suspension for different values of  $k$  are illustrated, whereas the remaining simulation details are unchanged. It is observed that for sufficiently small values of  $k$  ( $10^{-4} < k < 0.02$ ) the concentration profile across the domain shows an approximately linear behaviour. As a result, the concentration change is constant between two time steps in the same location for small  $k$ . The scatter plot of the concentration distribution can be represented by a linear function. These resulting functions, describing the distribution of concentration  $c_{eq}$  in the domain are shown in Fig. 4.4 b). The conclusion is, that as

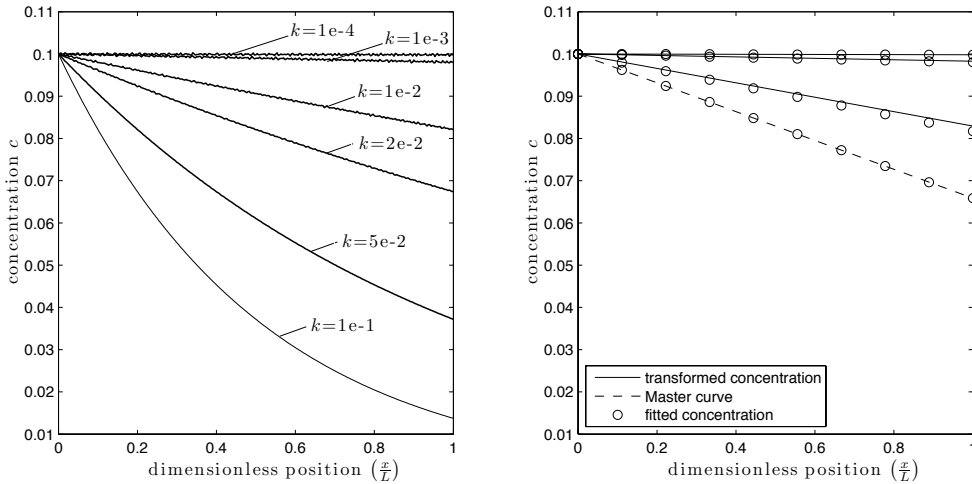


Figure 4.4: Distribution of the concentration  $c_{eq}$  at equilibrium, left: calculated concentration distribution, right: fitted and transformed concentration distribution.

long as values of  $k$  are considered, which lead to a linear distribution of equilibrium concentration, the results for different parameters of  $k$  can be converted into each other. When a distribution of equilibrium concentration is known for a certain factor  $k_M$ , it is possible to derive the distribution of concentration for another value of  $k$ . This means a master curve for the distribution of equilibrium concentration can be determined. Accordingly, the transformation follows the equation

$$c_{eq} \left( \frac{x}{L} \right) = m_M \frac{k}{k_M} \frac{x}{L} + \bar{c}. \quad (4.32)$$

In Eq. (4.32),  $m_M$  describes the slope of the concentration distribution, arising when  $k_M$  is used. The resulting concentration distribution is valid for one value of  $k$ .  $\bar{c}$  is the previously mentioned boundary condition for the concentration. Therefore, the graph

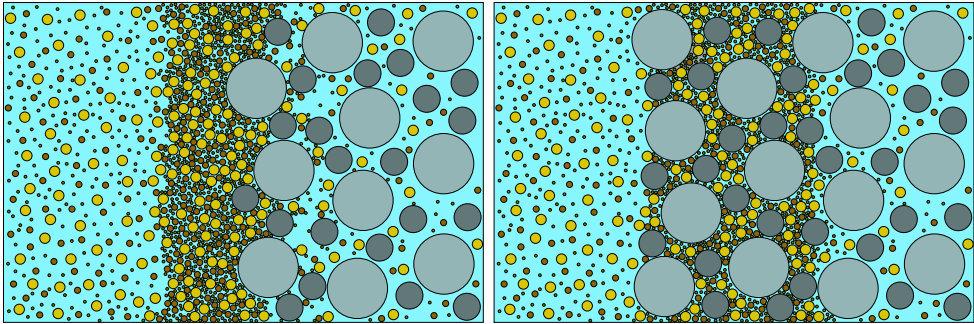


Figure 4.5: Formation of a filter cake. Left: external filter cake; right: internal filter cake.

for  $k_M = 0.02$  illustrates the master curve. This leads to a slope of  $m_M = -0.03415$  and  $\bar{c} = 0.1$ . The resulting distribution of concentration using these values and Eq. (4.32) are shown in Fig. 4.4 as solid lines. This fits very well with the calculated concentration gradients.

For larger values of  $k$  it is not sufficient to reduce the transformation of the concentration distribution to a pure rotation. This results from the non-linearity of the gradient of concentration.

Considering the results of the presented analyses, it is point out, that the proposed model is well-suited for the simulation of a filter cake formation. A filter cake is a localized layer of highly reduced permeability. For an explanation of this term a 1-dim domain is divided into two parts. In the left part of the domain the volume fraction of the solid skeleton is assumed to be zero  $n^{\text{sn}} = 0$ . The right part is represented by a four-phase mixture in accordance to the parameters used in the analysis. If an IBVP is solved with the previously described boundary conditions, two different types of filter cakes might occur. First, it is possible that an external filter cake is formed, cf. Fig. 4.5. Thereby the constriction sizes of the pore channels are smaller than the average diameter of the fluidized fines. Hence, the fines are not able to penetrate significantly in the second part of the domain. Instead the fines are deposited on the border in between the both parts. As a result, more particles accumulate at the interface, so that a layer with reduced permeability can be observed.

In contrast, the formation of an internal filter cake occurs cf. Fig. 4.5, if fines penetrate over a certain distance into the second part of the domain. The infiltration causes a local increase in the flow rate  $\mathbf{q}$  and a reduction of the permeability  $k^{\text{s}}$ . Hence, the production term  $\hat{n}^{\text{a}}$  is increased locally. As a result, a high amount of fines is infiltrated locally. It has to be pointed out, that the proposed model is applicable to cases of internal filter cakes only. To capture the occurrence of an external filter cake geometrical consideration concerning the analysis of the constriction size distribution are necessary.

## 4.5 Summary

In the preceding sections the governing differential equations of internal erosion processes of cohesionless soils were formulated based on the mass and momentum balances of the present phases. In addition material incompressibility was assumed. Within this framework, a four-phase model for infiltration processes was presented.

Furthermore, the IBVP was extended by a production term to simulate the infiltration of fines from the suspension to the solid fraction. The form of the introduced production term  $\hat{n}^a$  can be understood as a constitutive formulation. The production term is thermodynamically consistent and contains a material parameter  $k$ , which has to be validated by physical experiments. However, for a given combination of a filter material and a suspension, the appropriate values of  $k$  have to be determined by conducting infiltration experiments. For small values of  $k$  (representing linear profiles of the equilibrium concentration  $c_{eq}$ ) a master curve was found, which could be used to avoid experimental set-ups for respective soil materials. In particular, for larger values of  $k$ , resulting in a nonlinear concentration distribution, further theoretical, numerical and experimental investigations are necessary. In the future, additional investigations will be carried out with the aim to take the pore network into account and to describe its effects on the rearrangement phenomena in porous media. This will lead to an even more sophisticated description of the microscopical infiltration process.

## Chapter 5

# Transport and infiltration of suspensions through porous media

*In this chapter we develop and discuss a modelling approach to describe the transport of a suspension through granular porous media. Furthermore, a link between the coarse-grained Theory of Porous Media (TPM) and pore scale phenomena is presented, allowing to describe events on the pore-scale, e.g. the attachment of fines from the suspension to the porous medium (infiltration). For this, a statistical evaluation of the Constriction Size Distribution (CSD) of the granular porous skeleton was performed. By the comparison of the probability of occurrence of the value of a pore constriction with the probability of occurrence of particles which are larger than the pore constriction the amount of attached particles is identified. This leads to an evolution of the hydraulic properties of the considered domain, driven by the infiltration process. This allows to describe the evolution of the morphology of an ensemble of particles in a larger-scale continuum multi-phase approach and a related simulation model. Additionally, the evolution of the Grain Size Distribution (GSD) of the solid skeleton and the suspended particles in the carrier fluid is accounted for. Furthermore, an efficient way is presented to account for the evolution of the CSD in each time step and integration point numerically within a Galerkin finite element scheme. Therewith, the evolution of hydraulic properties of benchmark problems and more advanced 2-dim structures is studied. Additional, an analytical solution for a simplified 0-dim problem is derived and presented.*

## 5.1 Introduction

Granular porous media are widely spread and can often be found in geomechanics as well as in many technical applications. If a transport process of a suspension, i.e. a mixture of a fluid and fine particles through a porous skeleton is observed, many complex questions, such as the fluid/solid interaction of the system, arise. The present contribution is focused on so-called infiltration processes. In these, fine particles, which are dissolved in the fluid and transported through a granular porous medium, are deposited in the pore space of the primary fabric and attached to the skeleton. This leads to a significant evolution of effective hydraulic properties of the considered porous medium. Besides the creation of simulation models, also the development of an insight in the ongoing physical processes in such heterogeneous materials are of great importance.

Examples for technical applications of those processes are found in stability calculations of embankment dams [36, 43, 45]. The origins of the present contribution are located in the modelling of annular gap grouting processes in the field of mechanized tunnelling [96]. In this work a hydro-mechanical coupled approach is discussed, allowing to model transient processes and capturing the evolution of hydraulic properties. The fluid-structure interaction is realized with coupled partial differential equations using the homogenized, continuum-based TPM. The thermodynamically-consistent TPM extends the classical mixture theory [98] by the concept of volume fractions, cf. [22, 24, 28, 30].

One of the most famous simple relations to describe the morphological restriction for particle transport was introduced by Terzaghi [93] and is well known as Terzaghi's filter criterion. It relates one diameter of the soil to one diameter of the suspension in the carrier fluid

$$\frac{D_{15}}{d_{85}} \leq 4 - 5, \quad (5.1)$$

and predicts thereby filter stability. In Eq. (5.1) the diameter of the 15% fraction of the filtering soil is denoted as  $D_{15}$  and the diameter of 85% fraction of the particles dissolved in the suspension described as  $d_{85}$ .

Although the fraction of the smallest particles is often under-represented in terms of volume/mass, which are the classical quantities representing the composition of the mixture in the TPM, it is obvious, that in systems consisting of graded material the fraction of the smallest particles is dominating the physical effects [69]. In the present multi-phase approach, the effect of fines on the evolution of macro-scale hydraulic properties is taken into account by a novel multi-scale procedure implemented in a finite element simulation model. This is accounted for by enrichment of the continuum-based approach with micro-structural, statistical considerations.

The idea of the TPM is to divide the continuum to different, process relevant volume fractions and to describe their behaviour by first physical principles. In this contribution only hydraulic effects are captured. In addition to the balance of momentum of the suspension supplemented with a constitutive equation for the effective

drag, only balance equations for the mass of different fractions are considered. We assume that the carrier fluid of the suspension is a pore liquid (e.g. water). Thus, the effective or true density  $\rho^{\alpha R} := dm^\alpha/dv^\alpha$  is constant throughout the physical process, i.e.

$$\rho^{\alpha R}(t) = \rho^{\alpha R}(t_0) =: \rho_0^{\alpha R} = \text{const.} \quad (5.2)$$

Thus, as we discuss later in more detail, the considered balances of mass are collapsing to volume balances, cf. [81].

For the presented approach we complement the concept of volume fractions by the constituent inherent concept of species [3, 4]. Therefore, single volume fractions are subdivided into species, in a way, similar to the concept of volume fractions, that the sum of all species represents the behaviour of the corresponding volume fractions, cf. Figure 5.4.

The basis for the proposed continuum-approach is located in the simulation of internal soil erosion phenomena of hydraulic works as published by [14, 36] or sand production in the framework of oil petroleum industry, cf. [15, 63, 81, 101].

In this article first the evaluation of the transport properties depending on the micro structure is described. In the following the continuum-based modeling is derived and the Initial Boundary Value Problem (IBVP) is presented. Afterwards benchmark examples are introduced and discussed, including an analytical solution for a special case of the here presented problem. In the last part a 2-dim simulation consisting of sub-domains with different initial hydraulic properties is shown.

## 5.2 CSD-Analysis

For the development of criteria to determine the stability of granular packings with regard to erosion and/or infiltration, the concept of constriction sizes has to be defined. The constriction size  $A_{cs}$  is understood as the smallest area of a flow path connecting two pore spaces. It is always smaller than the connected pores themselves. For the transport of particles through a porous network the largest circular area which can be inscribed in a pore constriction is of special interest. This is the effective constriction size  $A_{cs}^R$ , cf. Figure 5.1, which is represented by the corresponding diameter  $d_{cs}$  of the effective circular pore constriction. If all pore constrictions of a certain volume in a granular material are characterized, a graph analogue to the Grain Size Distribution (GSD) is created. For this, the probability of occurrence of a certain effective pore constriction  $P_{cs}$  is plotted against its effective size using the diameter  $d_{cs}$  of the circular constriction. Although the distributions of grain size and constriction size are usually plotted in the same graph it has to be pointed out, that in the first case the physical diameter of the grain is plotted, whereas in the second case the diameter of the effective pore constriction, i.e. the largest diameter of a particle which could be passed through the pore, is depicted.

This leads to the concept of the Constriction Size Distribution (CSD) which is only applicable with the assumption of spherical particles. Other methods for the

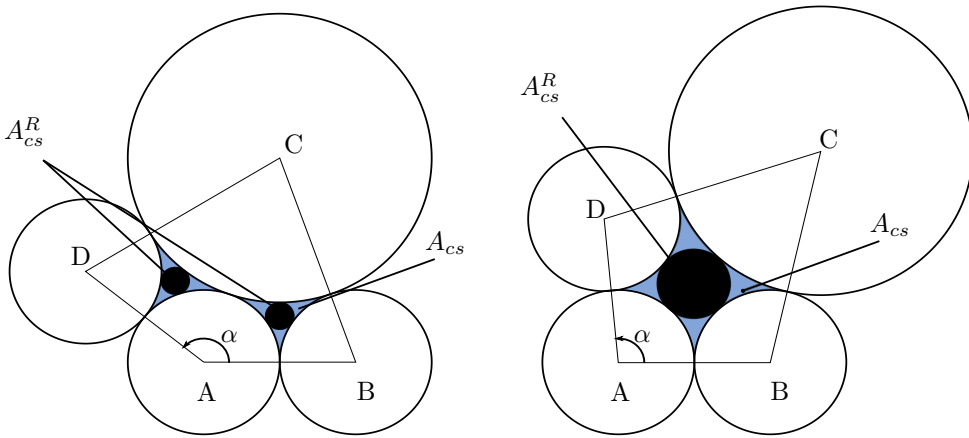


Figure 5.1: Visualization of two possible pore constrictions, the area of a pore constriction  $A_{cs}$  (blue), and the area of an effective pore constriction  $A_{cs}^R$  (black). Left: densest pore constellation. Right: loosest pore constellation.

characterization of the CSD exist, in which this assumption is avoided. Methods to mention are all imaging techniques, e.g. X-ray micro Computed Tomography ( $\mu$ CT) or Nuclear Magnetic Resonance (NMR) [37, 41], in which the whole pore space is characterized. The determination of the CSD has to be extracted from the 3-dim images of the pore network in a post processing step. The application of imaging techniques results in very accurate results. On the other hand those characterization methods are very time-consuming. Especially for the characterization of granular packings where the morphology is evolving in time. Such characterization experiments are only possible under high expenditure and have an academical use only.

Furthermore, approaches which are based on a numerically created packing of particles exist. There, numerical particle methods e.g. DEM [68] are used to generate a packing with given GSD and porosity  $\phi$ . From the numerically created pore network, the CSD is evaluated in a post-processing step, similar to image-based techniques. It has to be mentioned, that the numerical setup of the packing is again time consuming and difficult to use in investigations with evolving pore spaces based on clogging or suffosion phenomena.

### 5.2.1 State of the Art

For the characterization of the morphology of a granular packing, which is evolving in time due to rearrangement effects of fine particles, a fast approach has to be used. In this work we therefore combine a statistical approach for determining the CSD at the material point with a coarse-grained continuum-mixture model. The basic idea of the statistical approach traces back to a publication of Silveira in 1965 [78]. In order to calculate the CSD of a granular packing, first the GSD has to be discretized in  $f$  single

fractions. Silveira assumed that a constellation forming a pore constriction is always created by three particles. Consequently all possible combinations of particles of the fractions are considered and the constriction size is calculated for each of them. The single constrictions are accumulated to a distribution curve, analogue to the GSD. In the following years the approach provided by Silveira was improved in several details. Ziems [111] introduced the idea of calculating the probability of occurrence of a certain constriction not related to the mass but to the number distribution of the packing. Together with the assumption of a constant density of all particle fractions, this leads to a significantly higher impact of the fines in the system compared to the mass distribution. A grain packing algorithm restricted to consolidated soil using effective properties is given in [76]. Laboratory experiments measuring the CSD of a granular material were published by Wu *et al.* [107]. Reboul *et al.* [66] proposed two different approaches for gap-graded and continuously graded granular material.

Furthermore, Witt [105] could show by experimental investigations that a constellation can not be only formed by 3 particles, but also by 4 particles, cf. Figure 5.1, right. There are also constellations with more than 4 particles, but their probability of occurrence is much smaller than the one of 3 or 4-particles constellations. However, the proposed method is able to represent 4-particle constellations. Note, that in case of densest compaction, the 4 particle constellation collapses to two 3-particle constellations, cf. Figure 5.1, left. Therefore, those are automatically captured with this approach.

A summary of different techniques to evolve the CSD of a granular material and their historical derivation can also be found in [57, 103].

## 5.2.2 Statistical evaluation of the constriction size distribution

For the evaluation of the CSD of a granular packing in a statistical manner, the GSD of the solid and its relative density  $D$  is used. Those variables are very common and usually part of standard geomechanical testing procedures. The relative density is referred to the porosity  $\phi$  of the solid or, as in this work, to the area of pore constriction  $A_{cs}$ , cf. Figure 5.1

$$D = \frac{\max(A_{cs}) - A_{cs}}{\max(A_{cs}) - \min(A_{cs})}. \quad (5.3)$$

In this equation  $\max(A_{cs})$  describes the largest pore constriction of a certain GSD, i.e. the constriction size belonging to the largest particle species in the loosest state of compaction ( $D = D_0 = 0$ ). Accordingly,  $\min(A_{cs})$  represents the smallest constriction size of the system belonging to the smallest particle species in the densest state of compaction ( $D = D_1 = 1$ ). Furthermore, a number distribution (ND) is calculated

from the GSD assuming spherical particles with a constant density

$$q_{i,ND} = \frac{q_{i,m}}{d_i^3} \cdot \sum_{j=1}^f \frac{q_{j,m}}{d_j^3}. \quad (5.4)$$

Here,  $q_{i,ND}$  represents the relative number of particles,  $q_{i,m}$  the relative mass of particles, and  $d_i$  the diameter of particles for the grading  $i$ . The variable  $f$  describes the number of fractions. In the next step the constellations are assembled by considering all possible permutations of the different particle fractions. This step leads to  $f^4$  constellations [75].

Having a closer look at the received constellations, it is realized that a large number is geometrically identical. The calculation time of the chosen statistical approach is reduced significantly if those constellations are identified. Two constellations are geometrically identical if both constellations can be matched to each other by applying a pure rotation of the constellation or exchanging the position of particles located opposite to each other. Before deleting identical constellations, their probability of occurrence has to be added to the identified counterpart constellation. In Figure 5.2 the number of constellations considering all possible permutations with the number of only physically necessary constellations is compared. It is concluded, that the number of relevant constellations is drastically smaller than the number of all permutations. Therefore, the identification of double constellation leads to a much more efficient calculation process.

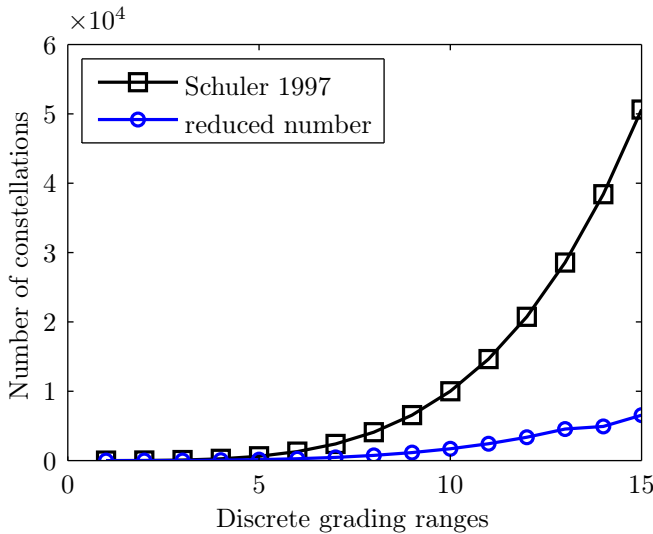


Figure 5.2: Comparison of all possible constellations resulting from permutation of  $f$  fractions (cf. Schuler [75]) with the number of physical unique constellations.

After assembling all constellations, the constriction size is evaluated for each remaining constellation by geometrical considerations. Further details are given in [73]. However, the output consists of a matrix including of all possible constriction sizes  $d_{cs,i}$  and their probability of occurrence  $P_{cs}$ , where the latter quantity is directly computed from the input GSD as

$$P_{cs}(A_{cs}^R) = \prod_{i=1}^4 q_{i,ND}(d). \quad (5.5)$$

### 5.2.3 Validation of statistical approach

To check the validity of the proposed approach a benchmark solution created by DEM from Reboul et al. [68] was investigated. The corresponding GSD and the CSD calculated on the basis of the particle position of the DEM approach are plotted in Figure 5.3. This result is used as a benchmark to match the data with the proposed statistical model. In many publications, the free parameter to match the statistical derived CSD are the relative density  $D$ , cf. Eq. (5.3) [67], or the porosity  $\phi$  which is directly related to the state of compaction  $D$ , cf. [38]. In Figure 5.3 the CSD for the densest packing ( $D = 1$ ) and for the loosest packing ( $D = 0$ ) is shown. At least two points of the benchmark CSD are computed analytically, the smallest constriction size, which corresponds to the constellation of 4 particles from the smallest discrete grading range in maximum compaction, and also the biggest constriction size, consisting of 4 particles from the biggest discrete grading range in the loosest compaction state. This condition is fulfilled for the proposed approach. Furthermore, it is stated that all possible CSD curves have to be between both fictive derived curves for densest and loosest compaction, cf. highlighted area in Figure 5.3. The benchmark results can not be matched by recalculating the CSD simply changing the relative density  $D$ . In this case, none of the limits is fulfilled. Therefore, a new method was developed to match the statistical and the benchmark result, including both limit points.

For this, the CSD for  $D = D_0 = 0$  and the CSD for  $D = D_1 = 1$  are calculated at the beginning. The output data consist of two vectors, one containing the diameter of the effective constriction size  $d_{cs,i}$  and the second one containing the corresponding probability of occurrence  $P_{cs,i}(d_{cs})$ . A weighted average of both curves is then created

$$d_{cs,ave} = g(\zeta) d_{cs,D_1} + (1 - g(\zeta)) d_{cs,D_0}. \quad (5.6)$$

In the simplest case, which is valid for a middle dense compaction state, the corresponding weighting function is given

$$g(\zeta) = \zeta \quad \forall \zeta \in [0; 1]. \quad (5.7)$$

This averaging method and linear function was used to calculate the fitted CSD which is also depicted in Figure 5.3. For this special case of GSD in middle compaction state the received results fit very well to the benchmark approach.

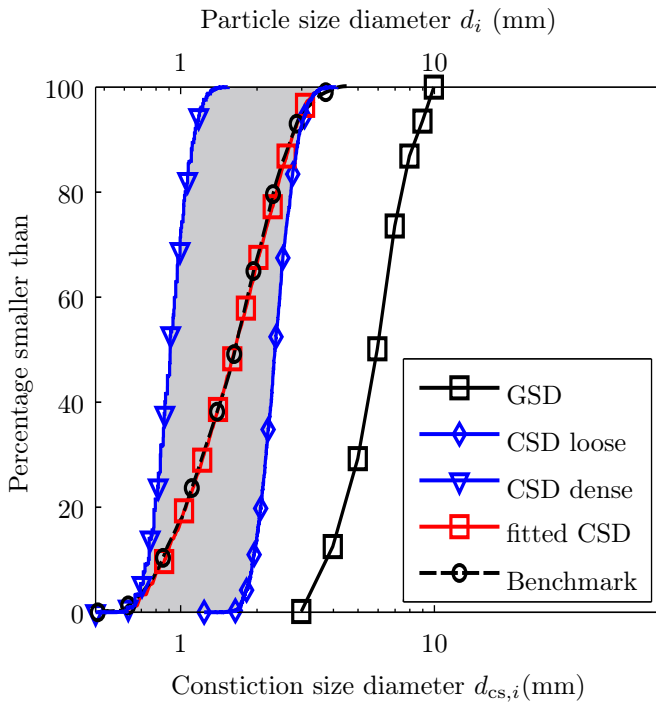


Figure 5.3: Comparison of the CSD using the proposed method with the CSD achieved by DEM simulations from Reboul et al. [68].

However, also more complex weighting functions, considering additional fitting parameter, can be used. Therefore, a two parameter logistical (sigmoid) function in the form of

$$g(\zeta) = \frac{1}{B - A} (\text{sig}(\zeta) - A), \quad \text{with} \quad (5.8)$$

$$\text{sig}(\zeta) = \frac{1}{L + \exp(-\zeta K)}, \quad \forall \zeta \in [0; 1], \quad (5.9)$$

$$A = \text{sig}(0) = \frac{1}{L + 1}, \quad (5.10)$$

$$B = \text{sig}(1) = \frac{1}{L + \exp(-K)}, \quad (5.11)$$

is proposed. Here,  $L$  and  $K$  are understood as free fitting parameters.

## 5.3 Multi-phase FEM approach to describe infiltration phenomena

### 5.3.1 Governing equations of extended continuum model

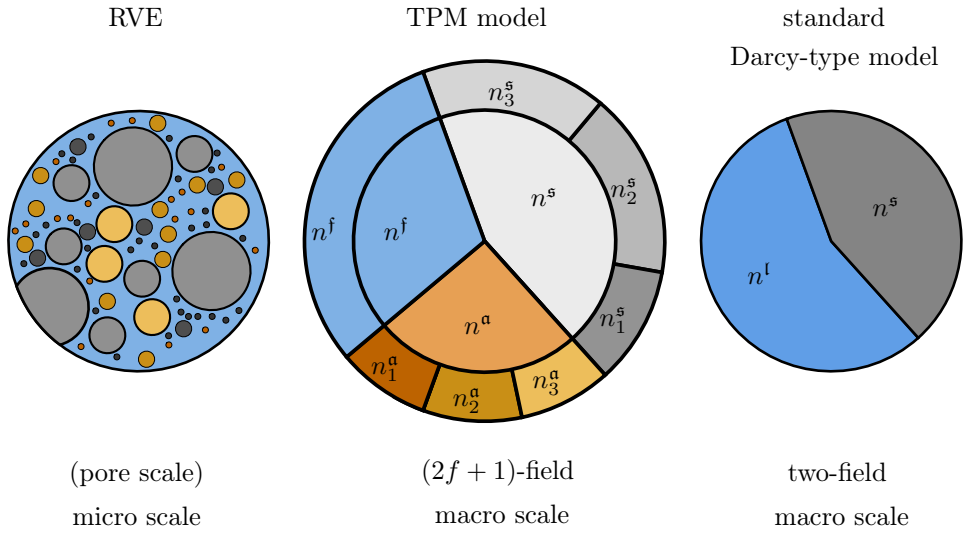


Figure 5.4: Extended homogenization technique. Left: mesoscopic RVE, right: a two field homogenization of the RVE taking only the liquid and the solid phase into account. Mid: illustration of the 3-phase approach and its extension to  $2f + 1$  phases.

In the second part of the derivation of the numerical model, we use the TPM, which is understood as an extension of the MT by the concept of volume fractions. The work presented here is an extension of a previous publication [71]. For the continuum-based formulation volume fractions  $n^\alpha$  are defined from macro-scale quantities, with  $n^\alpha = dv^\alpha/dv$ . The volume of the whole RVE is described by  $dv$  and the volume of a single constituent  $\varphi^\alpha$  is expressed as  $dv^\alpha$ .

The continuum approach proposed in this contribution has three different homogenization levels, cf. Figure 5.4. For the evolution of the effective dynamic viscosity  $\eta^{fR}(\mathbf{x}, t)$ , a two field approach is used. Thus, it has to be distinguished between the solid phase  $\varphi^s$  consisting of all solid particles forming the solid skeleton and the liquid phase  $\varphi^l$  describing the suspension, i.e. the mixture of the pore fluid and the dissolved particles. This is visualized in Figure 5.4, right.

In the next step, we can introduce the three phase homogenization, which extends the two phase approach by the differentiation between solid constituents  $\varphi^a$  in the suspension and carrier fluid  $\varphi^f$ , with  $n^l = n^f + n^a$ .

In order to describe microscopic effects a further level of homogenization is used. Therein, the definition of *species*  $\varphi_i^\alpha$ , which are denoted with an additional subscript, is introduced. The concept of species is invented by a further subdivision of single

volume fractions of the three phase homogenization. Precisely, the volume fraction of the solid  $\varphi^s$  and the volume fraction of the suspended particles  $\varphi^a$  are divided into  $f$  species, which leads to the  $(2f + 1)$ -field illustrated in Figure 5.4, middle. Physically, the species are described by the discrete grading ranges, which are a result of standard sieving test in soil mechanics.

Originally the hydraulic behaviour of the mixture was described by the volume balances of its constituents. Therefore, the reformulation

$$c = \frac{n^a}{\phi} \quad (5.12)$$

was used. To capture phenomena on the scale of single discrete particle grading ranges the volume balances of the dissolved particles  $\varphi^a$  and the solid skeleton have to be divided into  $f$  species. Therefore, the fraction of solid particles  $n^s$  is split into  $f$  species  $n_i^s$ , with  $i = 1, \dots, f$ . The original behaviour of this constituent is computed by the sum

$$n^s = \sum_{i=1}^f n_i^s. \quad (5.13)$$

Thus, the variable of the concentration of fines  $c$  is split to describe the concentration of fluidized fines in each species

$$c_i = \frac{n_i^a}{\phi}, \quad \text{with} \quad c = \sum_{i=1}^f c_i. \quad (5.14)$$

Considering the framework of the TPM, mass balances of individual constituents are used to derive the field-equations. Hence, the mass balance of a constituent  $\varphi^\alpha$  is written as

$$\partial_t(n^\alpha \rho^{\alpha R}) + \text{div}(n^\alpha \rho^{\alpha R} \mathbf{v}_\alpha) = \hat{\rho}^\alpha = \hat{n}^\alpha \rho^{\alpha R}, \quad (5.15)$$

with the so-called production term  $\hat{n}^\alpha$  of a constituent  $\varphi^\alpha$ . In general, in the local mass balance of one individual constituent the production term is triggering the mass exchange within individual constituents of the mixture. In this contribution, infiltration is considered which means that mass exchange only occurs between the constituent of suspended particles  $\varphi^a$  and the constituent of the solid skeleton  $\varphi^s$ . Taking into account the constraint of mass exchange for the whole mixture

$$\sum_{\alpha} \hat{n}^\alpha = 0, \quad (5.16)$$

the production terms can be related to each other as  $\hat{n}^s = -\hat{n}^a$ .

Again, the local partial mass balances which were derived in section 3.3.1 are used to create a numerical multi-field model. Assuming incompressibility of the solid grains  $\rho^{\alpha R} = \rho_0^{\alpha R} = \text{const.}$  and identical effective densities of the suspended particles and the solid skeleton  $\rho^{aR} = \rho^{sR}$  the partial local mass balances collapse to partial local

volume balances, which read

$$\partial_t(n^\alpha) + \operatorname{div}(n^\alpha \mathbf{v}_\alpha) = \hat{n}^\alpha. \quad (5.17)$$

In this contribution the volume fractions  $n^\alpha$  are subdivided into species  $n_i^\alpha$ , with the constraint

$$\sum_\alpha n_i^\alpha = n^\alpha. \quad (5.18)$$

Therefore, also the local partial volume balances are subdivided to obtain a balance equation for individual species, which is written as

$$\partial_t(n_i^\alpha) + \operatorname{div}(n_i^\alpha \mathbf{v}_i^\alpha) = \hat{n}_i^\alpha. \quad (5.19)$$

It has to be noted that the index of the velocity changes from subscript to superscript in this case, to keep a consistent notation.

First, the set of equations of the solid constituent  $\varphi^s$  with the volume fraction of the species  $n_i^s$  are derived from the volume balance of the solid particles

$$\partial_t(n_i^s) + \operatorname{div}(n_i^s \mathbf{v}_i^s) = \hat{n}_i^s. \quad (5.20)$$

In this case, the solid constituent  $\varphi^s$  as also the corresponding species are assumed to be rigid, therefore its velocity vanishes ( $\mathbf{v}_s = \mathbf{v}_i^s = \mathbf{0}$ ). This leads to an evolution equation for the species

$$\partial_t(n_i^s) = \hat{n}_i^s. \quad (5.21)$$

Note, that here the primary variable of the equations is changed from the porosity  $\phi$  to the solid species  $n_i^s$  compared to previous publications, e. g. [71]. This is necessary because a split of the porosity  $\phi$  leads to a non-closed set of equations.

In the next step, the set of equations of the dissolved species is written as

$$\partial_t n_i^a + \operatorname{div}(n_i^a \mathbf{v}_i^a) = \hat{n}_i^a. \quad (5.22)$$

Using the definition of the partial concentration  $c_i$  given in Eq. (5.14) and neglecting relative velocity between the fluid and the fluidized particle constituent as also the corresponding species ( $\mathbf{v}_a = \mathbf{v}_f = \mathbf{v}_i^a$ ), the partial volume balance of species  $i$  of the dissolved particles reads

$$\partial_t(c_i \phi) + \operatorname{div}(c_i \mathbf{q}) = \hat{n}_i^a, \quad (5.23)$$

with the so-called filter or Darcy velocity  $\mathbf{q}$ .

Hence, the mass exchange is only possible within the constituents  $\varphi_i^s$  and  $\varphi_i^a$  and of the same species  $i$ , the mass exchange terms are related to each other  $\hat{n}_i^s = -\hat{n}_i^a$ . Analogue to Eq. (5.13) and Eq. (5.14), we can rewrite the total value for the mass exchange term

$$\hat{n}^a = \sum_{i=1}^f \hat{n}_i^a. \quad (5.24)$$

Note, that in case of consideration of only one species, the extended approach reduces to the original proposed four phase approach, cf. [73]. In this case, geometrical consideration of the morphology of the considered material and its CSD is not useful, because physically this means, that both particles forming the skeleton and the particles suspended in the fluid are mono-disperse and of the same size. Since the constriction size of a mono-disperse packing is always smaller than the particle itself, clogging would happen immediately without transport. According to Steeb and Diebels [80] the production term has to be proportional to the absolute value of the filter velocity, in order to achieve a thermodynamic-consistent mass exchange within the constituents and species

$$\hat{n}_i^a \propto |\mathbf{q}|. \quad (5.25)$$

However, the assumption of the mass exchange term neglecting consideration of the morphology reads

$$\hat{n}_i^a = -c_i \phi |\mathbf{q}|. \quad (5.26)$$

Furthermore, Darcy's law [30] is obtained as the result of the balance of momentum and used to relate the pressure  $p$  to the filter velocity  $\mathbf{q}$

$$\mathbf{q} = -\frac{k^s}{\eta^{iR}} \text{grad } p. \quad (5.27)$$

Assuming a rigid porous skeleton ( $\mathbf{v}_s = 0$ ) the filter velocity is calculated from the seepage velocity of the fluid phase  $\mathbf{v}_f$  to  $\mathbf{q} = \phi \mathbf{v}_f$ . Here,  $k^s(\mathbf{x}, t)$  is the isotropic intrinsic permeability of the porous skeleton and  $\eta^{iR}(\mathbf{x}, t)$  the effective dynamic viscosity of the suspension. Both properties vary in space and time during the observation of an infiltration process and therefore have to be recalculated for each time step and integration point.

For the calculation of the intrinsic permeability of the porous skeleton  $k^s$ , the equation of Kozeny Carman, cf. Carrier [18]

$$k^s = \frac{1}{C_{KC}} \frac{1}{S_0^2} \left[ \frac{\phi^3}{(1 - \phi^2)} \right] \quad (5.28)$$

was applied. This is a semi-analytical approach relating the evolution of the intrinsic permeability to the evolution of the porosity  $\phi$ . The value of the Kozeny-Carman constant  $C_{KC}$  is documented to be in the range  $4.8 \pm 0.3$  but is usually set to 5, the specific surface area per unit volume  $S_0$  (in  $1/\text{cm}$ ) is computed straightforward. For a granular packing of spherical particles with the effective particle diameter  $d^R$  it reads

$$S_0 = \frac{6}{d^R}, \quad \text{with} \quad d^R = \frac{1}{\sum_{i=1}^f \frac{n_i^s/n^s}{d_i}}. \quad (5.29)$$

In this contribution the intrinsic permeability is not a fixed value, but is evolving within the infiltration process. Therefore, it has to be pointed out, that not only

the porosity  $\phi$  in Eq. (5.29), but also the effective particle diameter  $d^R$  is evolving within the infiltration process. The equation of Kozeny-Carman is broadly used in the framework of granular/porous media. Nevertheless, it has to be pointed out, that this method has its restriction. It works best for mono-disperse or narrow graded spherical particles and moderate porosity. The GSD is reduced to one scalar parameter, the effective particle diameter  $d^R$ , which is a very strong assumption. Conceptually it is also not very obvious to relate the intrinsic permeability to the pore space.

If the initial dynamic viscosity of the liquid phase  $\eta^{lR}$  is known, the evolution of the effective dynamic viscosity of a suspension  $\eta^{fR}$  is described using the equation

$$\eta^{fR} = \eta^{lR} \left( 1 + \frac{2.5 c}{2(1 - \kappa c)} \right)^2, \quad (5.30)$$

proposed by Eilers [31, 32]. Here, the material parameter  $\kappa$  takes the heterogeneity of the grading of the particles in the suspension into account. In case of mono-disperse particles  $\kappa = 1.28$  is documented. For broadly graded particles  $\kappa = 1.35$  and for narrow graded particle distributions  $\kappa = 1.30$  should be used. However, for the calculations in this contribution  $\kappa = 1.30$  was chosen. Note, that this equation is valid for dilute and dense suspensions. For dilute suspensions ( $c < 0.05$ ) it leads to the same results as the equation proposed by Einstein [33]

$$\eta^{fR} = \eta^{lR} (1 + 2.5 c). \quad (5.31)$$

The densest packing of mono-disperse spherical particles leads to a pore space of  $\phi = 0.26$ , which corresponds to  $c = 0.74$  considering the suspension only. However, a denser packing of mono-disperse spherical particles is non-physical, therefore effective dynamic viscosity  $\eta^{fR}$  in Eq. (5.30) goes to infinity in this case.

### 5.3.2 Initial Boundary Value Problem (IBVP) for Infiltration processes

Considering the volume balance of the mixture [71], cf. Eq. (5.32), the IBVP is created by combination of all previously described equations

$$\operatorname{div} \left[ -\frac{k^s}{\eta^{fR}} \operatorname{grad} p \right] = 0, \quad \forall \mathbf{x} \in \mathcal{B} \times t, \quad (5.32)$$

$$\partial_t (c_i \phi) - \operatorname{div} \left[ c_i \frac{k^s}{\eta^{fR}} \operatorname{grad} p \right] = \hat{n}_i^a, \quad \forall \mathbf{x} \in \mathcal{B} \times t, \quad (5.33)$$

$$\partial_t (n_i^s) = -\hat{n}_i^a, \quad \forall \mathbf{x} \in \mathcal{B} \times t, \quad (5.34)$$

where  $\mathcal{B}$  represents the spatial domain and  $t$  the time. To close the system, boundary conditions for the filter-velocity  $\mathbf{q}$  (cf. Eq. (5.27)) and the flux of suspended particle species  $c_i^*$  at the Neumann boundary  $\Gamma_N$  as well as the pressure  $p$  and the concentrations of the particle species  $c_i$  at the Dirichlet boundary  $\Gamma_D$ , with  $\Gamma_N \cap \Gamma_D = \partial\mathcal{B}$  and

$\Gamma_N \cup \Gamma_D = 0$  are prescribed as

$$q = \mathbf{q} \cdot \mathbf{n} = \bar{q}, \quad c_i^* = c_i \bar{q}, \quad \forall \mathbf{x} \in \Gamma_N \times t, \quad (5.35)$$

$$p = \bar{p}, \quad c_i = \bar{c}_i, \quad \forall \mathbf{x} \in \Gamma_D \times t. \quad (5.36)$$

Within this multi-phase approach an own set of boundary conditions for each physical field is chosen. Thus, the Neumann boundary  $\Gamma_N$  and the Dirichlet boundary  $\Gamma_D$  are set separately for the field of the concentrations of particle species with the primary variables  $c_i$  and for the pressure field with the primary variable  $p$ . Additionally, the following initial conditions are used at  $\mathcal{B}_0 \times t$

$$p = p_0, \quad c = c_0, \quad \phi = \phi_0, \quad \forall \mathbf{x} \in \mathcal{B}_0 \times t. \quad (5.37)$$

For the solution of the set of equations the standard mixed Galerkin finite element scheme is applied. To obtain the weak format, the previously described balance equations are multiplied by test functions and integrated in space

$$\int_{\mathcal{B}} \frac{k^s}{\eta^{fR}} \text{grad } p \cdot \text{grad } \delta p \, d\mathcal{B} = \int_{\Gamma_q} \delta p \mathbf{q} \cdot \mathbf{n} \, d\Gamma_q, \quad (5.38)$$

$$\int_{\mathcal{B}} \delta c_i [\partial_t(c_i)\phi - c_i \partial_t(n^s) - \hat{n}_i^\alpha] \, d\mathcal{B} - \int_{\mathcal{B}} c_i \frac{k^s}{\eta^{fR}} \text{grad}(\delta c_i) \cdot \text{grad } p \, d\mathcal{B} = \int_{\Gamma_{c_i^*}} \delta c_i c_i \mathbf{q} \cdot \mathbf{n} \, d\Gamma_{c_i^*}, \quad (5.39)$$

$$\partial_t(n_i^s) = -\hat{n}_i^\alpha. \quad (5.40)$$

Note that Eq. (5.40) is an Ordinary Differential Equation (ODE) integrated in time at each integration point of the finite element, parallel to the set of Partial Differential Equations (PDE), cf. Eqs. (5.38, 5.39). The Neumann boundary is depicted as  $\Gamma_{c_i^*}$  for the field of the concentrations of particle species  $c_i$  and as  $\Gamma_q$  for the pressure field. Furthermore, it has to be pointed out, that the right hand side (rhs) of Eqs. (5.38, 5.39) can be prescribed as a boundary condition in a finite element scheme. In this case, the rhs vanishes in the corresponding equations.

### 5.3.3 Analytical solution for a simplified hydraulic IBVP

In case of simplification of the IBVP described above, cf. section 5.3.2, an analytical solution can be found. For this, the physical dimension of the problem is reduced to 0-dim by neglecting the spatial dependencies of the field equations and also by using of no-flux or periodic boundary conditions for the species of concentrations  $c_i$ . This means numerically that the field equations are evaluated in one material point, which leads to a homogeneous problem.

For this, we can find an analytic solution for the previously described problem. Thus, considering a 0-dim IBVP, the equations given above are further simplified to

$$\partial_t(c_i\phi) = \hat{n}_i^a, \quad \text{with} \quad n_i^s = c_i\phi, \quad \rightsquigarrow \partial_t n_i^s - n_i^s q = 0, \quad (5.41)$$

$$\partial n_i^s = -\hat{n}_i^a. \quad (5.42)$$

Hereby, the PDE resulting from the balance of mass of the mixture, with the pressure  $p$  as primary variable is identically satisfied in the 0-dim case. To overcome this issue, the filter velocity is prescribed as a boundary condition. First, we assume a spatially homogeneous filter velocity  $q = q_0$ , with  $\text{div}\mathbf{q} = 0$ . The remaining two ODE describing the problem are solved analytically using standard methods. Using  $t_0 = 0$  for the initiation of the process the solution reads

$$n_i^s(t) = n_{i0}^s - n_{i0}^a (\exp(-q_0 t) - 1), \quad \text{with} \quad n_i^a(t) = n_{i0}^a \exp(-q_0 t). \quad (5.43)$$

The second part of Eq. (5.43) is the trivial solution of an evolution equation. In order to compare the analytical solution of the IBVP with the solution of the numerical approach, we reformulate the analytical problem avoiding the assumption of a constant filter velocity. This means the filter velocity is allowed to evolve in time  $q = q(t)$ . Thereby the filter velocity  $q$  is exported from the numerical calculation and used for the analytical approach. Following this procedure, both approaches become directly comparable with each other. To make use of this procedure the solution of the IBVP (Eqs. (5.41), (5.42)) has to be adapted. For an arbitrary filter velocity the solution resulting from the set of balances of the solid constituents with the primary variables  $n_i^a(t)$  is

$$n_i^a(t) = n_{i0}^a (e^{-Q(t)} - 1), \quad \text{with} \quad Q(t) = \int q(t) dt. \quad (5.44)$$

This is used to calculate the species of solid constituents

$$n_i^s(t) = n_{i0}^s - n_{i0}^a (e^{-Q(t)} - 1). \quad (5.45)$$

Note, that for this derivation the relation

$$\int_{\tilde{t}=t_0}^t \exp\left(-\int_{\tilde{t}=t_0}^{\tilde{t}} q(\tilde{t}) d\tilde{t}\right) q(\tilde{t}) d\tilde{t} = -\exp\left(-\int_{\tilde{t}=t_0}^{\tilde{t}} q(\tilde{t}) d\tilde{t}\right) \quad (5.46)$$

was used. The derivation of this relation is not straightforward, but its validity can be shown easily by considering the derivative of the second part which results in the first part.

Species of suspended fines	$n_1^a/n^a$	0.8	
Species of suspended fines	$n_2^a/n^a$	0.2	
Species of solid particles	$n_1^s/n^s$	0.6	
Species of solid particles	$n_2^s/n^s$	0.4	
Diameter of species 1	$d_1$	0.125	mm
Diameter of species 2	$d_2$	0.25	mm
Initial concentration	$c_0$	0.2	
Initial solid constituent	$n_0^s$	0.68	
Pressure at boundary	$p_0$	0.3	Pa
Pressure at boundary	$p_1$	100.3	Pa
Time step	$\Delta t$	60	s
Simulation time	$t_{\max}$	$3 \times 10^4$	s

Table 5.1: Material properties and used boundary conditions

### 5.3.4 Example: comparison of analytical and numerical solution

For the comparison of the analytical and numerical approach an IBVP was considered, cf. Figure 5.5. The parameters, used for the calculation, are summarized in Table 5.1. The numerical example was constructed using Dirichlet boundary conditions  $\bar{p}_1$  for the pressure on the left and  $\bar{p}_0$  on the right edge. According to Darcy's law (Eq. (5.27)) the filter velocity  $\mathbf{q}$  is defined. This filter velocity is used in the analytical and the numerically implemented approach to ensure comparability of both methods. Due to the spatial homogeneity of the problem, the numerical implementation is realized by a 1-element FEM calculation with periodic concentration boundary conditions  $\bar{c}$  on both boundaries.

For the comparison of both approaches the temporal evolution of the porosity  $\phi$  is depicted, cf. Figure 5.6. Both, the numerical and the analytical solution are in good agreement. Due to the assumption that from a geometrical point of view all particles of the suspension have to be attached to the skeleton, the porosity in the equilibrium state can be easily computed from the initial state to  $\phi_\infty = \phi_0(1 - c_0)$ . Both graphs match this equilibrium very well.

## 5.4 Evolution of morphologic properties

### 5.4.1 Numerical realization

After the description of the statistical approach to determine the CSD as well as the extension of the volume balances to describe  $f$  species of fine particles, both methods have to be combined to describe the infiltration behaviour of each single species.

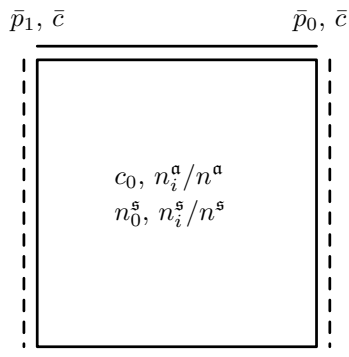


Figure 5.5: Illustration of the 0-dim IBVP and the used boundary and initial conditions.

From geometrical considerations, infiltration of fluidized particles takes place if the pore constriction is smaller or of the same size compared to the transported particle ( $d_{cs} \leq d$ ). Considering a non-uniform mixture of particles a probability of infiltration due to geometrical restrictions has to be considered and is written as

$$P_{\text{inf}}(d_i) = P_{cs}(d_{cs,i}). \quad (5.47)$$

To capture the evolution of hydraulic properties due to infiltration of fine particles in a suspension to a rigid porous skeleton, the CSD has to be evaluated for each time step and each RVE of the considered domain, which is very time consuming even with the efficient statistical calculation of the CSD. However, by plotting the CSD and GSD of particles dissolved in the fluid  $\varphi^a$  and particles of the skeleton  $\varphi^s$  using the same x-axis, the computational expensive vector of the size of the effective pore constriction is remaining constant during the calculation. Only the probability of the occurrence of single pore constrictions vary, but is easy to calculate, cf. Eq. (5.5).

In the part of the FE approach the statistical evaluation is considered by splitting the mass/volume balance with respect to the number of species existing in the fluidized fines  $\varphi^a$  and the solid constituent  $\varphi^s$ . Therefore, one mass exchange term for each species has to be defined.

$$\hat{n}_i^a = -\psi P_{\text{inf}} c_i \phi q. \quad (5.48)$$

Thereby,  $n^a = c \phi$  is the total amount of potentially infiltratable particles in the RVE during one time step and the range of the probability of infiltration of a single species is  $P_{\text{inf}} \in [0, 1]$ . Following, the condition  $0 \leq (\psi | \mathbf{q}|) \leq 1$  has to be fulfilled.

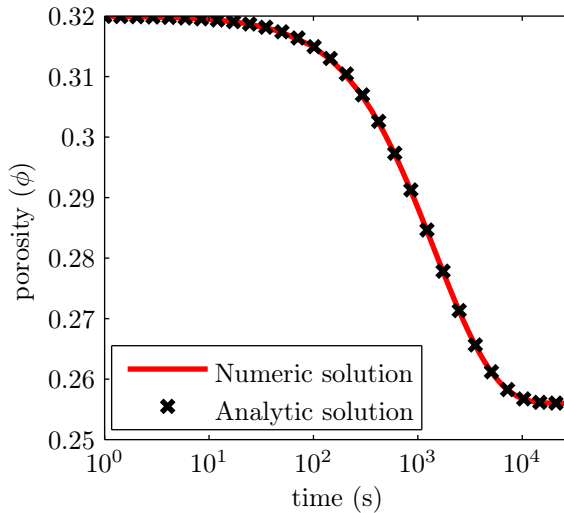


Figure 5.6: Comparison of the numerical and analytical solution for a 0-dim infiltration IBVP.

#### 5.4.2 Numerical example for evolution of morphological properties

In this section a numerical example is presented, combining all previous described capabilities of the developed model. Therefore, we extend the previous 0-dim example, cf. Figure 5.5, by the geometrical analysis of the morphology. In this example three different combinations of GSD in the skeleton and the suspension were used, cf. Table 5.2. The idea of those calculations is visualized in Figure 5.8. For all of them filter stability of the solid is assumed. This means only infiltration phenomena are studied and all kind of erosion is neglected:

- In *case A* particles of the suspension are mostly larger than the pore constrictions, which leads to clogging of the suspension in the skeleton.
- In *case B* particles of the suspension are partially larger than the pore constrictions. Some of the particles penetrate through the specimen, whereas others infiltrate in the solid domain.
- In *case C* the particles of the suspension are much smaller than the pore constrictions. Almost all particles penetrate through the solid domain.

The corresponding results are shown in Figure 5.9. The simulations of *case A* and *case C* are understood as limit cases for the evolution of hydraulic properties. In *case C*, the GSD of filter and suspension is chosen in a way, that no infiltration takes place due to geometrical considerations. The particles in the suspension are much smaller than the initial constriction sizes in the skeleton. Therefore, all particles of

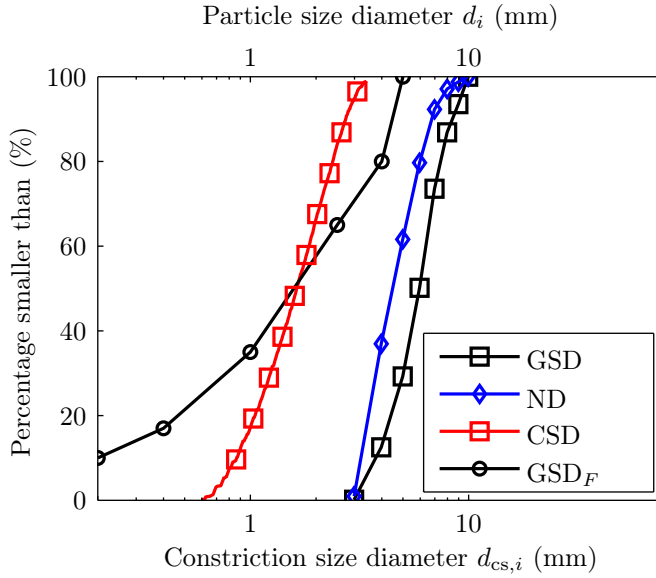


Figure 5.7: Definition of the probability of infiltration considering geometrical restrictions. ND represents the Number Distribution of the particles forming the skeleton, GSD<sub>F</sub> represents the Grain Size Distribution in the suspension.

	species $i$	1	2	3	4	5
case	particle size (mm)	0.125	0.25	0.5	1	2
A	$n_i^s/n^s$	0.6	0.4			
	$n_i^a/n^a$	0.8	0.2			
B	$n_i^s/n^s$				0.4	0.6
	$n_i^a/n^a$	0.2	0.3	0.4	0.1	
C	$n_i^s/n^s$				0.4	0.6
	$n_i^a/n^a$	0.7	0.3			

Table 5.2: Initial morphologic properties.

the suspension can pass the domain without infiltration. This means the porosity is not evolving in time and remains constant. Accordingly, *case A* is chosen that all particles in the suspension are of the same magnitude or larger than the initial pore constrictions. This means that geometrically all particles are filtered by the solid skeleton. In this case, the maximum reduction of the porosity in the solid skeleton is observed. Therefore, the equilibrium porosity is computed analytically, as shown in the previous example in section 5.3.4. The resulting porosity in *case A* matches the analytically computed porosity.

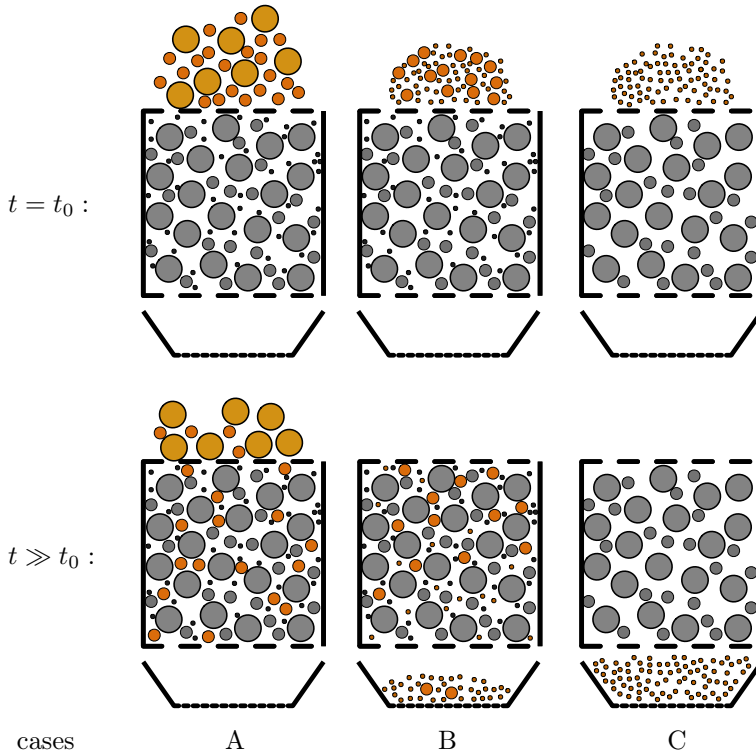


Figure 5.8: Defined cases in order to perform benchmark calculations. For all cases filter stability of the solid is assumed.

### 5.4.3 Numerical example of a 2-dim heterogeneous domain

Based on the previous chapters, this section presents a two dimensional example. Therefore, a 2-dim domain was created, consisting of different regions, cf. Figure 5.11. The initial and boundary conditions used for the calculation are summarized in Table 5.3. The convective transport of the suspension through the porous medium in the domain is driven by a pressure boundary condition on the left ( $\bar{p}_1$ ) and the right ( $\bar{p}_0$ ) edge. For the concentration of the suspended particles, a periodic boundary condition  $\bar{c}$  is used. This means the total amount of solid particles, consisting of sus-

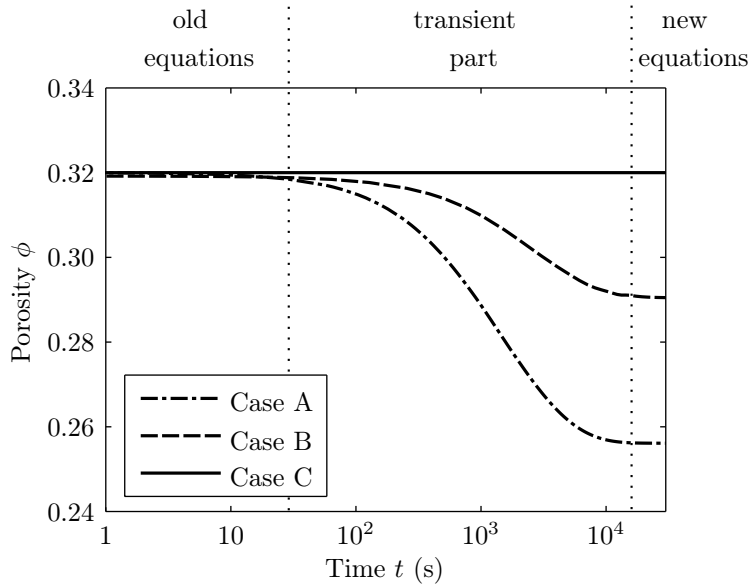


Figure 5.9: Evolution of porosity due to different micro structures. the description of the single cases is given in Figure 5.8.

pendent particles and particles forming the porous medium, remains constant during the calculation ( $n^s(t) + n^a(t) = \text{const}$ ).

In the sub-domain 1 (1a & 1b) the initial porosity  $\phi_{0,1} = 0.32$  was used, cf. Figure 5.11. Furthermore, the infiltration was neglected in this sub-domain by setting the material parameter  $\psi = 0$ . This material properties describe a porous material with large pore constrictions, e.g. mono-disperse packed spherical particles. In sub-domain 2 (2a & 2b) the initial porosity of  $\phi_{0,2} = 0.4$  and a GSD, consisting mostly of coarse particles, was used. This corresponds to a coarse sand material. In the center the sub-domain 3 is allocated, with an initial porosity of  $\phi_{0,3} = 0.45$ , but a finer graded sand than sub-domain 2.

The results of this calculation are summarized in Figures 5.10 and 5.12. In Figure 5.10 contour plots of the considered domain during different time steps are shown. The permeability decreases, driven by the infiltration process within time. This effect is not homogeneously distributed, but depends on the initial values of the permeability and GSD of each sub-domain. The evolution of hydraulic properties occur in horizontal and vertical direction. The permeability is initially homogeneously distributed within the sub-domains. Due to a higher permeability in sub-domain 2 a higher filter velocity arises, leading to a higher rate of infiltration. On the other hand the GSD of sub-domain 1 contains finer particles, compared to sub-domain 2, which results in smaller pore constrictions. Therefore, the probability of infiltration  $P_{\text{inf}}$  is higher. In the first phase of the calculation ( $t < 0.46$  h) this contrary effects are equilibrated, leading to a smaller difference in permeability between the sub-domains.

Length of domain 1	$L$	1	m
Pressure at boundary	$\bar{p}_1$	1.3	Pa
Pressure at boundary	$\bar{p}_0$	0.3	Pa
Concentration of fines	$c_0$	0.4	
Concentration of fines	$\bar{c}$	periodic b.c.	
Effective dynamic viscosity	$\eta_0^{\text{fR}}$	1	mPa s
Initial porosity	$\phi_{0,1}$	0.32	
Initial porosity	$\phi_{0,2}$	0.4	
Initial porosity	$\phi_{0,3}$	0.45	
material parameter	$\psi_1$	0	
material parameter	$\psi_2 = \psi_3$	1	
simulation time	$t_{\text{max}}$	242	h
Initial intrinsic permeability	$k_{0,2}^s$	$7.93 \times 10^{-6}$	$\text{m}^2$

Table 5.3: Material properties and used boundary conditions used for the 2-dim calculation.

In the following phase infiltration takes place more homogeneously reducing the permeability. In the last phase of the calculation ( $t = 242$  h) the permeability is almost homogeneously distributed. In Figure 5.12 the GSD and CSD in the beginning and the end of the calculation process is shown for two specific points, which are specified in Figure 5.11.

## 5.5 Discussion

In the first example in section 5.3.4 a 0-dim IBVP was created, allowing to capture the evolution of the hydraulic properties (e.g. porosity  $\phi$ , intrinsic permeability  $k^s$ ) for a homogeneous infiltration process. By the application of periodic boundary conditions for the concentration of fluidized particles and focussing on one material point by neglecting all spatial dependencies, the inherent heterogeneous infiltration process is transformed to be homogeneous. Therefore, the equilibrium state after all fluidized particles were attached to the solid skeleton can be easily computed. The evolution of the morphology and the evaluation of geometric quantities is neglected within this method. The reduced analytical approach was compared to a numerical simulation using the full approach on the 0-dim example. Both methods match the equilibrium state after infiltration very well and additionally they are in good agreement with each other.

The analytical 0-dim approach is on the one hand useful for academic purposes. On the other hand it is a very simple and fast approach for the estimation of the

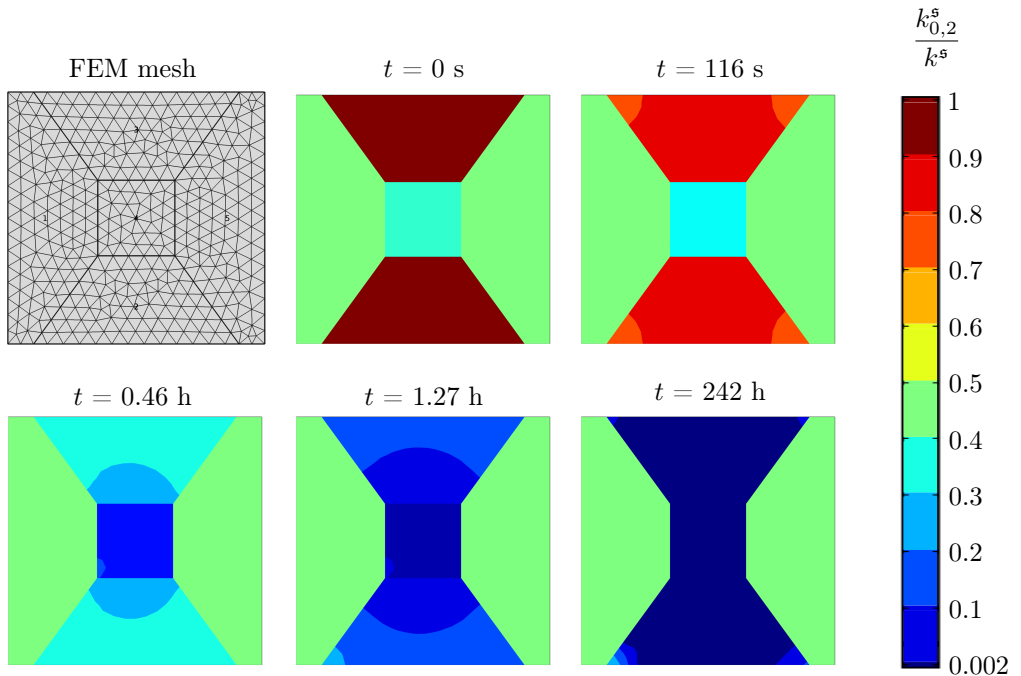


Figure 5.10: Evolution of the intrinsic permeability as a result of the 2-dim calculation for different times. The results were scaled with respect of the initial intrinsic permeability of sub-domain 2.

evolution of hydraulic properties. In a first step the distribution of the porosity within time is computed. In a second step this is linked to the evolution of intrinsic permeability using the equation of Kozeny Carman, cf. Eq. (5.29). The equations were formulated for a direct application of a prescribed filter velocity (Neumann b.c.). In case of a prescribed pressure gradient (Dirichlet b.c.) the Darcy relationship (cf. Eq. (5.27)) has to be used, additionally.

The numerical example in section 5.4.2 describes the evolution of hydraulic properties induced by the consideration of the morphology. The presented examples were implemented using the 2-dim formulation. Analogue to the previous example, the problem was constructed in a way that a 0-dim description of the results in the domain is sufficient.

This example shows the impact of the statistical consideration of geometry during the infiltration process on the hydraulic properties. This is illustrated by the calculation of 3 different cases, described above. Case C shows the result, which is occurring if the calculation is conducted so that the CSD of the solid is larger than the GSD of the fluid. Thus, this calculation is comparable to a classical transport formulation neglecting the impact of the geometry and infiltration in general. Comparing case B

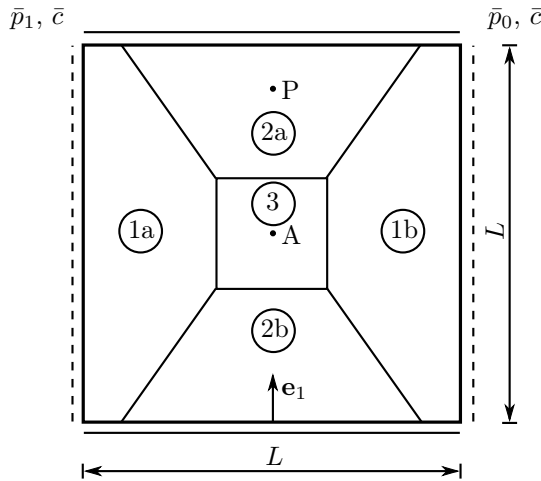


Figure 5.11: Visualization of the computed 2-dim IBVP.

to case A leads to the conclusion that in case B not all particles are attached to the solid skeleton but can also pass through the domain. This effect is in contrast to the filter rule of Terzaghi, cf. Eq. (5.1), which is fulfilled for case B. This means that no penetration of the suspension should occur. Summarizing it can be stated that the observation of two single points of the GSD of solid and suspension is not sufficient for predictions of infiltration phenomena. In case of uniformly distributed GSD of solid and fluid the filter rule leads to correct, although too restrictive results. In case of broadly distributed GSD it even might lead to wrong results. This is especially the case for gap graded materials. Case A shows the maximum possible change in the hydraulic properties. This occurs, because all particles are infiltrating in the porous domain or even before. Physically such a case is called the formation of an external filter-cake, which is a well-known and often unwanted phenomenon in geotechnical applications. In this case the final porosity can be computed straightforward as shown in section 5.3.4.

A 2-dim example was presented in section 5.4.3. This example exploits all capabilities of the method, described in this contribution. The presented problem can not be solved analytically. Therefore, the examples presented before are used as benchmarks to ensure correct results. Despite the simplicity of the conducted calculation, the results are quite complex and not easy to predict. Slightly different initial values in the GSD within sub-domains lead to different rates of infiltration. The process is driven by heterogeneities and the species of smallest particles in the system. The example shows that infiltration of fine particles in the porous domain varies the effective hydraulic properties significantly, leading to a more precise description of the multi-physical transport problem. This model is also applicable to more realistic and complex structures, but the computation time, especially resulting from the linking procedures of the continuum and micro-scale approach has to be optimized. Never-

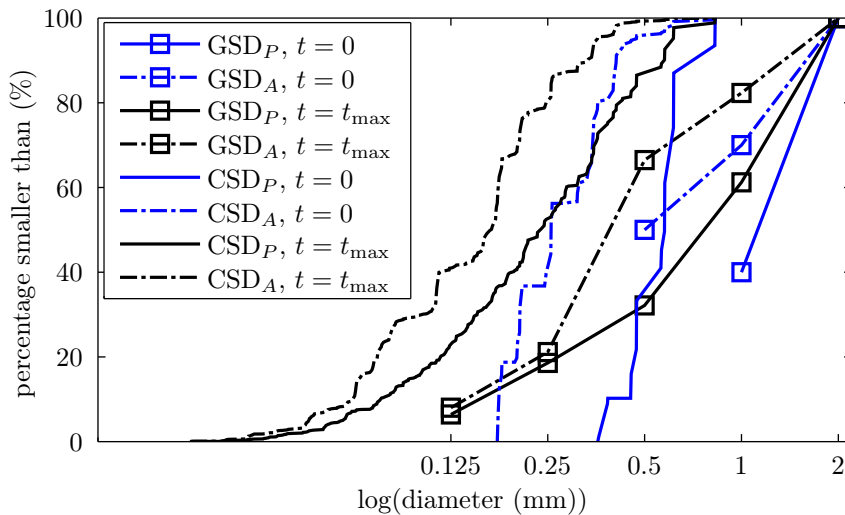


Figure 5.12: Evolution of the morphology, here described by the GSD and CSD, induced by infiltration of a suspension in two different points of the domain in Figure 5.11.

theless, a description of the morphology by considering the evolution of the GSD in each integration point was achieved.

The main drawback of the proposed model so far is its restriction on hydraulic properties. In classic poro-elastic formulations it could be shown that also the evolution of mechanical properties has an impact on the overall process. Due to deformations of the solid skeleton also the pore spaces are effected. Furthermore, it is expected that the infiltration of fine particles to the solid skeleton has an influence on the stiffness of the porous matrix and also on the final deformation-field of the process.

The combination of the statistical evaluation of the morphology properties with the TPM leads to the possibility of consideration of micro-scale effects together with the usage of a field equation on the mesoscopic continuum formulation. The proposed calculation approach removes the restriction of the consideration of effective material properties, only. Within the multi-physical approach different types of variables are used. The macro- and mesoscopic quantities are evolved due to micro-structural effects. The approach presented in this contribution adds the possibility of the description of an additional level of homogenization, capturing micro-scale effects additional to the use of conventional continuum formulation.

## 5.6 Summary

In this contribution a multi-phase modelling approach was presented, capturing the evolution of hydraulic properties of a porous medium on the continuum scale. To enrich the continuum scale with informations from the micro structure, a statistical method to calculate the CSD of a granular medium was derived and implemented at the material point of the coarse-grained continuum model. The statistical approach is a fast way to take into account the morphology of a granular material. Based on existing calculation methods, the statistical CSD analysis was performed and improved in crucial points. First, it was found that not every constellation is unique and therefore the calculation process can become a lot more efficient, by considering only the necessary constellations. Furthermore, it was pointed out that approaches taking into account the relative density of a granular material, which were often used so far, are not appropriate to capture the smallest and largest pore constriction at the same time. A new averaging technique was presented, which is in very good agreement with numerical results using a 3-dim pore network modelling approach. A simple way of coupling the single approaches was presented by a novel definition of the mass exchange terms, which is defined by the comparison of the probability of occurrence of a certain constriction size value  $P_{cs}$  with the probability of occurrence of a particle with a larger diameter than the pore constriction. It could be shown that the consideration of the whole GSD of solid matrix and the suspension leads to more accurate results concerning infiltration processes and filter stability, than conventional methods, cf. Eq. (5.1).

In the second part of the contribution, a continuum based approach was extended from the description of single constituents to the description of constituents subdivided into species. In this framework the species correspond to discrete grading ranges of particles, which could be a result of sieving tests, which is the standard method for characterization of granular materials. In the resulting simulation model, mass/volume balances of the partial constituents are numerically solved by the Galerkin finite element method. This allows to describe the evolution of the hydraulic properties of the mixture.

The link from the micro scale to the continuum model is realized with constitutive equations of the mass exchange terms  $\hat{n}_i^a$ , describing the probability for attachment of each species within the fluid to the solid skeleton. Therefore, considerations on the micro scale are the driving processes for the evolution of hydraulic properties. Thus, the discussed model combines, in an averaged sense, small-scale morphological constituents and transport process of fines with large-scale Darcy-type transport equations.

This combination of simulations using different methods and scales allows to set an IBVP and to solve it numerically. This fact makes the presented approach easy to implement and applicable to technical applications. Although different examples up to 2-dim were presented here, it has to be pointed out that the general numerical approach, especially the statistical method, is valid for 3-dim without any restrictions.

## Chapter 6

# Hydro-mechanical simulations of the annular gap grouting process in mechanized tunnelling

*In this chapter a hydro-mechanical coupled model is developed using the TPM. The approach is formulated on the continuum scale. The main feature of the proposed approach is the simulation of the evolution of hydraulic and mechanical properties during the convective transport of a suspension through a deformable porous medium. Within this approach infiltration, stiffening, consolidation and plastic deformations are considered. The numerical model is applied on an example in the field of mechanized tunnelling, simulating a tunnel cross-section during the gap grouting process. The main focus here is to study the evolution of the intrinsic permeability and the settlements. The latter are represented by the deformation of the porous solid structure at the interface of the soil and the grouting domain.*

## 6.1 Introduction

### 6.1.1 Suspension flow through porous media

The understanding of the ongoing processes during and especially after the backfilling of the annular gap is of crucial importance to reach an efficient, fast and secure bedding of the tunnel lining. Therefore, we propose a numerical modelling approach, capturing the main physics of the technical application. The proposed multi-phase continuum model is based on the concept of superimposed continua in the framework of the

TPM, cf. Ehlers and Bluhm [30]. Within this concept, the pore fluid is modelled as a suspension consisting of a tracer fluid and dissolved particles. As we restrict ourselves to small Re-number, i.e. creeping flow, non-Newtonian effects (non-linear shear stresses vs. shear strain rates) are not taken into account.

Considering this, infiltration is understood as the attachment of particles from the suspension into the pore spaces or pore constrictions of the solid porous medium. The driving process is the convective transport of the suspension and also the micro structure of the porous medium and the particles in the fluid. The attachment of fine solid particles to the solid skeleton leads on the one hand to an evolution of hydraulic properties by reduction of the pore spaces and the intrinsic permeability of the solid skeleton. On the other hand also the mechanical properties are varied, because the additionally attached particles lead to an increase in stiffness of the solid skeleton. From the modelling point of view, infiltration can be captured with a so called mass exchange term in the relevant mass balances as published by de Boer [13] or Steeb *et al.* [86].

Various aspects of the infiltration processes are taken into account within the proposed model. There are already many modelling approaches existing, which describe single effects. For the modelling of the hydraulics of particle transport through porous media an analytical model has been proposed by Locke *et al.* [57]. Kenney *et al.* proposed the idea to relate the particle transport to a so-called controlling constriction size [49]. The approach was extended by Kenney and Lau [50] to predict the internal filter stability of a granular filter. An explicit solution for the critical hydraulic gradient for the penetration of particles through a porous medium was provided by Indraratna [44]. A contribution focussed on the formation of an internal filter cake using the concepts of the evaluation of the grain packing is provided by Schwartz and Wilkinson [76].

Experimental studies of rearrangement effects are also crucial for a physical understanding and parameter identification. The transport of a suspension through a porous medium during infiltration and drainage was carried out by Zhuang *et al.* [110]. Furthermore, analytical solutions for many simplified and decoupled problems have been developed by Verrujt [102], some of them are presented and used for benchmarking purposes in this contribution. A model describing a similar effect of rearrangement modelling, i.e. the erosion process, has been proposed by Steeb *et al.* [81]. In addition to previously published approaches [70, 71, 73], also deformation of the solid porous medium is captured in order to be able to simulate settlements of the surface induced by the excavation process during the construction of a tunnel. The continuum-based formulation is described within the poro-elastic approach published by Biot [10].

The aim of this work is to develop a numerical continuum model for the simulation of the hydro-mechanically coupled grouting process in mechanized tunnelling. The evolution of hydraulic properties has been already discussed in previously published approaches [70, 71, 73]. It could be shown that an evolution of the morphology results from the infiltration process leading to significant variation of the hydraulic

properties. The quantification of this properties, especially represented by the intrinsic permeability, is the basis for the adequate design of the annular gap grouting mortar with respect to the dewatering process.

Apart from the hydraulic properties also the mechanical properties of the annular gap mortar have an important impact on the grouting procedure. Thus, the numerical model in this work is extended to capture the evolution of mechanical properties in addition to the hydraulic part. The deformation of the solid porous medium is captured in order to be able to simulate settlements of the surface induced by the excavation process during the construction of a tunnel.

A fast transition from the pumpable properties of the grout in the initial phase to a shear-stiffness of the grouting material, which allows to recover the primary stress state of the surrounding soil in the final phase is required. The evolution of mechanical properties is determined by different processes. Thus, stiffening, consolidation and plasticity have been identified and, therefore, modelled in the following of this work.

The consolidation process describes the development of the solid skeleton of the annular gap grout induced by dewatering. Thereby, a decrease of pore space results in a higher coordination number of the particles, which results in an increase of stiffness of the grouting material. The continuum-based formulation of consolidation is described within the poro-elastic approach published by Biot [10].

As described above, this contribution is focussed on cement-free annular gap grouting mortars. In order to reach the demanded shear-stiffness, the application of cement-free mortars in tunnelling is restricted to permeable granular soils. For cohesionless granular soils plasticity occurs also for small deformations. Thus, although this approach is restricted to small deformations of the solid, also a simple plastic constitutive assumption is considered to account for a more realistic simulation of the mechanical properties of the porous medium.

The plastic deformation is characterized by dislocations of single grains, which results in de-structuring of the solid skeleton. The solid skeleton becomes weaker during plastic deformations. The infiltration of fine particles increases the volume fraction of the solid skeleton, which leads to a stiffening process of the solid skeleton. Thus, plasticity and stiffening can be present simultaneous and have an contrary phenomenological effect. The numerical modelling approach is illustrated in Figure 6.1. In the upper part of the figure the rheological model for the simultaneous simulation of plasticity and stiffening is shown as a series connection of both elements. The rheological element on the left consists of in parallel connected spring elements describing the stiffening effect. Initially the stiffness of the solid skeleton is represented by the spring stiffness  $C_1$ . As a result of infiltration of fine particles to the solid skeleton its stiffness increases. This is illustrated with additional connections of the spring elements  $C_2-C_n$ . In the rheological illustration the stiffness is represented by  $n$  springs in a discrete way. In the following part of this work it will be shown that in the numerical model the increase of stiffness is not discrete but continuous. On the right hand side of the rheological model a friction element is shown, describing plastic deformations in the classical way.

In the lower part of Figure 6.1 exemplary stress-strain curves are shown, assuming plastic and stiffening material behaviour. Applying a load on the stiffening element, leads to an increase in stiffness of the solid skeleton, which is related to the infiltration process and therefore, to the hydraulic conditions. In case of an unloading the stiffness of solid material remains constant. This is accounted for by the slope of the unloading path in the stress-strain curve, which corresponds to the slope of the last loading path. In the middle of the figure the corresponding stress-strain curve of an well-known ideal plastic material behaviour is shown. Initially the material behaviour is elastic. As soon as the yielding stress is reached additional deformation does not lead to an increase of the solid stress, but to a plastic deformation. The unloading path of the material is parallel to the loading path, which means that the material stiffness after the loading cycle is the same as before the loading.

Furthermore, the behaviour of the suspension is captured by a mass balance and a constitutive assumption for the effective dynamic viscosity of a particle laden fluid.

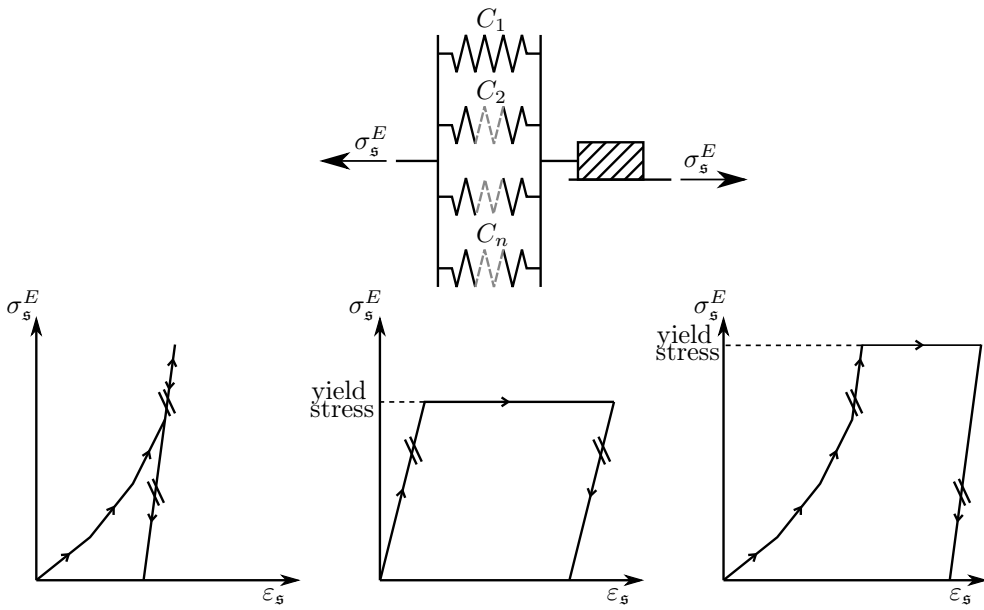


Figure 6.1: Details of numerical implementation of plastic behaviour of the solid skeleton and its stiffening due to infiltration. Upper part: rheological model capturing stiffening and plasticity simultaneously. The stiffening behaviour is represented by in parallel connected spring elements and the plastic deformation by the friction element. Lower part: stress-strain curves of a stiffening (left), plastic solid material (middle), and the superposition of both effects (right).

## 6.2 Continuum mechanical framework of modelling hydro-mechanical coupling in porous media

### 6.2.1 Kinematics

In this section, a method to capture the hydro-mechanical coupling of a fully saturated porous medium is presented. Hence, a brief introduction of the TPM is given.

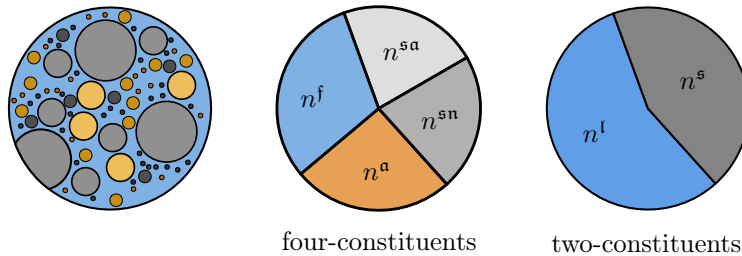


Figure 6.2: Fully saturated RVE representing a soil material (left), its homogenization within the TPM, according to Steeb [82], as a four-constituent approach, with  $\alpha = \{\mathfrak{s}\mathfrak{a}, \mathfrak{s}\mathfrak{n}, \mathfrak{a}, \mathfrak{f}\}$  (middle), and the two-constituent approach, with  $\beta = \{\mathfrak{l}, \mathfrak{s}\}$  (right).

In order to use the TPM for the description of the processes mentioned above, a homogenization technique is applied. The physics of a Representative Volume Element (RVE) is traced back on individual phases  $\varphi^\alpha$  of the constituent  $\alpha$ . The mixture  $\varphi$  is given as the superposition of all phases

$$\varphi = \sum_{\alpha} \varphi^{\alpha}. \quad (6.1)$$

Thus, the impact of a constituent  $\varphi^\alpha$  on the physical behaviour of the mixture is reduced on the volume fraction of a constituent  $\varphi^\alpha$ . The volume fraction with respect to a constituent  $\varphi^\alpha$  is defined as

$$n^\alpha = \frac{dv^\alpha}{dv}, \quad (6.2)$$

where  $dv^\alpha$  describes the volume of a constituent  $\alpha$  in a certain unit cell with the volume  $dv$ . The Representative Volume Element (RVE), illustrated in Figure 6.2 is divided into four or two constituents with respect to its volume fraction, depending on the application. In case of four constituents the following volume fractions are defined:  $n^f$  describes the volume fraction of the fluid,  $n^a$  the volume fraction of particles, which are suspended in the fluid,  $n^{sn}$  represents the particles forming a deformable porous matrix, which is not participating in rearrangement effects, and  $n^{sa}$  describes the volume fraction of particles which are attached to the skeleton due to infiltration from the constituent  $n^a$ .

A two-phase model is derived from the four-phase model by summing up certain volume fractions. Here, the liquid fraction consists of the pore fluid and the therein dissolved particles  $n^l = n^f + n^a$ . The solid constituent represents the solid particles

forming the porous skeleton and the attached particles  $n^s = n^{sn} + n^{sa}$ . In the following it will be shown that the two-phase model is used, describing the evolution of the dynamic viscosity of the suspension. For a formulation of the problem, which is easy to interpret from physical point of view, the following reformulation is presented

$$\phi = 1 - n^s, \quad (6.3)$$

$$c = \frac{n^a}{\phi}, \quad (6.4)$$

$$a = \frac{n^{sa}}{n^s}, \quad (6.5)$$

where  $c$  describes the concentration of suspended fine particles in the fluid,  $\phi$  the porosity of the medium, and  $a$  the amount of fine particles, that are attached to the solid matrix. Note, that this formulation is restricted to fully-saturated volumes, i.e. there is one liquid constituent, only. This allows to formulate the algebraic constraint for the mixture  $n^f + n^{sa} + n^{sn} + n^a = n^l + n^s = 1$ .

Furthermore, incompressibility of all constituents is assumed. Therefore, the effective densities of the constituents

$$\rho^{\alpha R} = \rho_0^{\alpha R} = \frac{dm^\alpha}{dv} = \text{const} \quad (6.6)$$

remain constant. Thereby  $dm^\alpha$  describes the mass of a constituent  $\varphi^\alpha$ . Assuming incompressibility of the constituent, gas phases, which are known to be compressible can not be captured. Additionally, also dynamic processes, e.g. the propagation of acoustic waves, can not be simulated.

Motivated by the numerical implementation of the proposed approach using a Galerkin-type finite element scheme, the motion of liquid constituents is described using a modified Eulerian approach. Thus, the seepage velocity  $\mathbf{w}$  is introduced as

$$\mathbf{w} = \mathbf{v}_l - \mathbf{v}_s, \quad (6.7)$$

with  $\mathbf{v}_l$  denoting the velocity of the liquid phase  $\varphi^l$  and  $\mathbf{v}_s$  the velocity of the solid skeleton  $\varphi^s$ . The filter or Darcy velocity is given as

$$\mathbf{q} = \phi \mathbf{w}. \quad (6.8)$$

## 6.2.2 Balance equations

Using the concepts of the TPM, we introduce partial local balance relations to derive the field equations. The partial local mass balance of a constituent  $\varphi^\alpha$  is given as

$$\partial_t(n^\alpha \rho^{\alpha R}) + \text{div}(n^\alpha \rho^{\alpha R} \mathbf{v}_\alpha) = \hat{\rho}^\alpha = \hat{n}^\alpha \rho^{\alpha R}, \quad (6.9)$$

with the velocity  $\mathbf{v}_\alpha$  of the constituent  $\varphi^\alpha$  and the volume production term  $\hat{n}^\alpha$ . With the assumptions of constant effective densities of the constituents, cf. Eq.(6.6) and

mass exchange between constituents with the same effective density, the partial local mass balance can be simplified to the partial local volume balance which reads

$$\partial_t(n^\alpha) + \operatorname{div}(n^\alpha \mathbf{v}_\alpha) = \hat{n}^\alpha. \quad (6.10)$$

According to Figure 6.2 the volume/mass exchange is restricted in this numerical model to the constituent of the suspended particle  $\varphi^a$  and the constituent of particles attached to the solid skeleton  $\varphi^{sa}$ , cf. Ehlers and Buhm [30]. This prescribes the direction of phase transition, which is represented in this work by the phenomenon of infiltration. Together with the constraint of mass/volume exchange for the mixture

$$\sum_\alpha \hat{n}^\alpha = 0, \quad (6.11)$$

it can be concluded that the production term is simplified to  $\hat{n}^{sa} = -\hat{n}^a$ .

For the description of the mechanical behaviour of the unit cell, the partial local balance of momentum of an individual constituent  $\varphi^\alpha$  is introduced as

$$\rho^\alpha \mathbf{a}_\alpha - \operatorname{div} \mathbf{T}^\alpha = \rho^\alpha \mathbf{b}^\alpha + \hat{\mathbf{s}}^\alpha - \hat{\rho}^\alpha \mathbf{v}_\alpha, \quad (6.12)$$

with the volume force  $\mathbf{b}^\alpha$ , the total momentum production  $\hat{\mathbf{s}}^\alpha$ . The direct momentum production  $\hat{\mathbf{p}}^\alpha$  is given as

$$\hat{\mathbf{p}}^\alpha = \hat{\mathbf{s}}^\alpha - \hat{\rho}^\alpha \mathbf{v}_\alpha. \quad (6.13)$$

Additionally, we can formulate the restriction of the total momentum production for the mixture as

$$\sum_\alpha \hat{\mathbf{s}}^\alpha = 0. \quad (6.14)$$

### 6.2.3 Constitutive formulation

The infiltration process is triggered by a mass exchange term  $\hat{n}^a$ . With this term the rate of particles which rearrange from the volume fraction  $n^a$  to  $n^{sa}$  is quantified. In order to close the set of equations a constitutive assumption for the mass exchange term  $\hat{n}^a$  is required. The thermodynamic consistency is ensured by the relation  $\hat{n}^a \propto q$  as derived by Steeb and Diebels [80]. Hence, this contribution is not focussed on the evolution of geometrical properties of the particle packing, but on its mechanical properties. A simplified expression for the mass exchange term

$$\hat{n}^a = -\psi c \phi q \quad (6.15)$$

is used, where  $\psi$  [m] describes a material parameter which depends on the morphology of the porous skeleton and the fluidized fines in the suspension. For a more sophisticated formulation details are given in [72].

The coupling of the mechanical properties between the solid structure and the pore fluid is realized via the concept of effective stresses of Terzaghi [25, 92]. This is formulated as

$$\mathbf{T}^\alpha = \mathbf{T}_E^\alpha - n^\alpha p \mathbf{I}, \quad (6.16)$$

where  $\mathbf{T}_E^\alpha$  is the extra stress tensor and  $\mathbf{T}^\alpha$  the partial Cauchy stress tensor of a constituent  $\varphi^\alpha$ . The pore pressure is depicted as  $p$ . This concept is applied on the mixture, i.e. the sum of all constituents. Therefore, the concept of effective stresses is written as  $\mathbf{T} = \mathbf{T}_E^s - p \mathbf{I}$ .

For the derivation of a linear-elastic constitutive equation for the extra stress tensor  $\mathbf{T}_E^s$  of the solid constituent  $\varphi^s$ , we follow the idea of Steeb *et al.* [86] to interpret the volume fraction of the solid particles attached to the skeleton  $n^{s\alpha}$  as a process variable in terms of the constitutive formulation using the framework of the entropy principle published by Coleman and Noll [21]. Thus, the free Helmholtz energy  $\Psi^s$  of the solid constituent  $\varphi^s$  is assumed as

$$\Psi^s(a, \boldsymbol{\varepsilon}_s) = (1 + a) \left( \frac{1}{2} \lambda (\text{tr}(\boldsymbol{\varepsilon}_s))^2 + \mu \text{tr}(\boldsymbol{\varepsilon}_s^2) \right), \quad \text{with} \quad \mathbf{T}_E^s = \frac{\partial \Psi^s}{\partial \boldsymbol{\varepsilon}_s}. \quad (6.17)$$

The strain of the solid skeleton is denoted as  $\boldsymbol{\varepsilon}_s$ ,  $\lambda$  and  $\mu$  are the well known Lamé parameter, which are obtained from various sets of other elasticity parameters. The elastic fourth order stiffness tensor  $\overset{4}{\mathbf{C}}(\lambda, \mu)$  can also be used equivalently. The amount of attached particles is denoted as  $a$  and results by the reformulation used in Eq. (6.5) from the volume fraction  $n^{s\alpha}$ . Then the elastic constitutive assumption for the solid skeleton reads

$$\mathbf{T}_E^s = (\lambda \text{tr}(\boldsymbol{\varepsilon}_s) \mathbf{I} + 2 \mu \boldsymbol{\varepsilon}_s) (1 + a). \quad (6.18)$$

For  $a = 0$ , which physically means that no particles were infiltrated to the solid skeleton yet, Eq. (6.18) represents linear-elastic behaviour. Therefore,  $a$  acts as a stiffening parameter, in terms of an inverse-damage formulation in this case and accounts for the evolution in the stiffness of the solid skeleton due to attachment of additional particles to it. This is an assumption, which has to be validated experimentally. Especially linearity of Eq. (6.18) has to be questioned. It is interesting to note here, that, according to Steeb *et al.* [81] this parameter is not an additional unknown, but can directly be calculated by integrating the volume balance of the stable part of the solid skeleton  $\varphi^{s\text{st}}$  to

$$a = 1 - \frac{(1 - a_0)(1 - \phi_0)(1 - \text{div} \mathbf{u}_s)}{1 - \phi}. \quad (6.19)$$

The deformations of the solid phase is expressed as  $\mathbf{u}_s$  and the initial amount of attached particles is  $a_0$ . Neglecting erosion processes and considering infiltration only, the initial amount of attached particles is not present ( $a_0 = 0$ ). Note, that this type of constitutive formulation might lead to non physical results of increasing stresses if an numerical experiment with constant strain value and increasing number of attached

particles  $a$  is considered. This can be overcome by an incremental implementation of Eq. (6.18).

For the numerical implementation of the stiffening behaviour the elastic constants are modified and are given as

$$\lambda^* = \lambda(1 + a), \quad \mu^* = \mu(1 + a). \quad (6.20)$$

Therefore, also a modified stiffness tensor is defined as

$$\mathbf{C}^*(\lambda^*, \mu^*) = (1 + a) \mathbf{C}(\lambda, \mu), \quad (6.21)$$

using the corresponding elastic constants.

In case of modelling infiltration phenomena as presented within this approach, an evolution of the dynamic viscosity of the liquid phase, i.e. the mixture of the fluid and suspended particles is observed. In order to account for this, evolution equations for the effective dynamic viscosity  $\eta^{fR}$  of the suspension were formulated. For dilute suspensions (small concentration  $c$ ) Einstein proposed a linear dependency of the effective dynamic viscosity  $\eta^{fR}$  and the concentration of suspended particles  $c$ , which is given as

$$\eta^{fR} = \eta^{lR} (1 + 2.5c). \quad (6.22)$$

Following Einstein, this equation is limited to dilute suspensions and is valid for  $c \leq 0.05$ . Later, Eilers [31, 32] proposed a non-linear dependency, which is valid for dilute and dense suspensions. The equation derived by Eilers reads

$$\eta^{fR} = \eta^{lR} \left( 1 + \frac{2.5c}{2(1 - \kappa c)} \right)^2, \quad (6.23)$$

with the material parameter  $\kappa$ . The material parameter depends on the grading of the GSD. For mono-disperse particle distributions  $\kappa = 1.28$  and in case of narrow graded material  $\kappa = 1.30$  is proposed. For broadly graded material  $\kappa = 1.35$  can be used. The following examples were conducted using  $\kappa = 1.30$ . In general, Eq. (6.23) collapses to Eq. (6.22) for small values of the concentration  $c \leq 0.05$ . Eq. (6.23) is valid for concentrations of  $c < 0.74$ . This value represents the most densest packing of mono-disperse spherical particles.

Additionally, Darcy's law [30] was used, which establishes a dependency of the pressure gradient  $\text{grad } p$  to the filter velocity  $\mathbf{q}$ . For the quasi static case ( $\mathbf{a}_f = \mathbf{0}$ ) it can be written as

$$\mathbf{q} = -\frac{k^s}{\eta^{fR}} \text{grad } p. \quad (6.24)$$

As it will be shown later, the porosity  $\phi$  is one of the primary variables within the multi-physical approach. For the evaluation of the hydraulic conductivity, the intrinsic permeability  $k^s$ , which is purely dependent on the porous material and is not affected by the penetrating fluid, is calculated. Thus, a link of the porosity  $\phi$  and

the intrinsic permeability  $k^s$  is given by the Kozeny-Carman equation [18] as

$$k^s = \frac{1}{C_{\text{KC}}} \frac{1}{S_0^2} \left[ \frac{\phi^3}{(1-\phi^2)} \right], \quad (6.25)$$

with the Kozeny-Carman parameter  $C_{\text{KC}}$  which is in the range  $4.8 \pm 0.3$ , but usually 5 is used. The parameter  $S_0$  describes the specific surface of the porous medium per unit volume. In case of a granular porous medium  $S_0$  reads

$$S_0 = \frac{6}{D_{\text{eff}}}, \quad \text{with} \quad D_{\text{eff}} = \frac{1}{\sum_{i=1}^f \frac{n_i^s/n^s}{d_i}}, \quad (6.26)$$

$D_{\text{eff}}$  being the effective particle diameter of the considered GSD of the solid skeleton. If the GSD consists of  $f$  discrete grading ranges, then one certain grading with the index  $i$  is described by its mean diameter  $d_i$  and the corresponding species  $n_i^s$ .

#### 6.2.4 Extension to soil-plasticity

After the formulation of the hydro-mechanical coupling using an extended linear-elastic constitutive formulation, the constitutive relation of the mechanical part of the approach is extended to capture plastic deformations of the solid skeleton. This is necessary to capture a realistic stress state of granular porous material. In the following section, the definitions given in section 3.5.3 are used to implement plastic deformations of the solid skeleton in addition to the hydro-mechanical coupling and the stiffening effect caused by infiltration of the fines. Therefore, the most important definitions are repeated and applied on the modelling approach, which is created in this chapter of the thesis.

Again, the additive decomposition of the solid strain  $\boldsymbol{\varepsilon}_s$  and the corresponding rate  $\dot{\boldsymbol{\varepsilon}}_s$  into the elastic  $\boldsymbol{\varepsilon}_s^{\text{el}}$  and the plastic part  $\boldsymbol{\varepsilon}_s^{\text{pl}}$  is performed as

$$\boldsymbol{\varepsilon}_s = \boldsymbol{\varepsilon}_s^{\text{el}} + \boldsymbol{\varepsilon}_s^{\text{pl}}, \quad \dot{\boldsymbol{\varepsilon}}_s = \dot{\boldsymbol{\varepsilon}}_s^{\text{el}} + \dot{\boldsymbol{\varepsilon}}_s^{\text{pl}}. \quad (6.27)$$

According to Figure 6.1 stiffening and plastic deformations have contrary effects on the solid skeleton but can be simultaneously present. To account for this the constitutive equation for the elastic deformation is modified to

$$\mathbf{T}_E^s = \mathbf{C}^* : \boldsymbol{\varepsilon}_s^{\text{el}}. \quad (6.28)$$

This leads also to a modified definition of the stress increment  $\dot{\mathbf{T}}_E^s$ , which is given as

$$\dot{\mathbf{T}}_E^s = \mathbf{C}^* : \dot{\boldsymbol{\varepsilon}}_s - \dot{\lambda} \mathbf{C}^* : \frac{\partial F}{\partial \mathbf{T}_E^s} \quad (6.29)$$

with the function of the yield surface  $F$ . The increment of the plastic multiplier  $\dot{\lambda}$  becomes

$$\dot{\lambda} = \frac{\left(\frac{\partial F}{\partial \mathbf{T}_E^s}\right)^T : \mathbf{C}^* : \dot{\boldsymbol{\varepsilon}}_s}{\left(\frac{\partial F}{\partial \mathbf{T}_E^s}\right)^T : \mathbf{C}^* : \frac{\partial F}{\partial \mathbf{T}_E^s}}. \quad (6.30)$$

Finally, the constitutive relation of elasto-plastic material behaviour including stiffening effects is written as

$$\dot{\mathbf{T}}_E^s = \left( \mathbf{C}^* - \frac{\mathbf{C}^* : \frac{\partial F}{\partial \mathbf{T}_E^s} \otimes \left(\frac{\partial F}{\partial \mathbf{T}_E^s}\right)^T : \mathbf{C}^*}{\left(\frac{\partial F}{\partial \mathbf{T}_E^s}\right)^T : \mathbf{C}^* : \frac{\partial F}{\partial \mathbf{T}_E^s}} \right) : \dot{\boldsymbol{\varepsilon}}_s. \quad (6.31)$$

This chapter of the thesis is focussed on the hydro-mechanical coupling and the impact of single coupling phenomena. Therefore, the most simple yielding function representing perfect plastic material behaviour is used in the following. In order to obtain this the constant in the criterion of Drucker-Prager, cf. Eq. (3.101) is zero ( $\alpha_{DP} = 0$ ), which leads to the yielding function defined as

$$F = \sqrt{J_2} - k_{DP}. \quad (6.32)$$

Note, that the focus of the model presented in this chapter is to describe the interaction of infiltration and plasticity. In order to capture realistic soil behaviour it can be extended by more sophisticated yielding-criteria.

## 6.2.5 Boundary Value Problem considering infiltration and deformation of the solid skeleton

Summing up all above described relationships an Initial Boundary Value Problem (IBVP) is created consisting of four coupled Partial Differential Equations (PDE's):

$$\operatorname{div} \mathbf{v}_s + \operatorname{div} \mathbf{q} = 0, \quad \forall \mathbf{x} \in \mathcal{B} \times t, \quad (6.33)$$

$$\partial_t(c\phi) + \operatorname{div}(c\phi \mathbf{v}_s) + \operatorname{div}(c\mathbf{q}) = \hat{n}^a, \quad \forall \mathbf{x} \in \mathcal{B} \times t, \quad (6.34)$$

$$\partial_t(\phi) - \operatorname{div}(\mathbf{v}_s) + \operatorname{div}(\phi \mathbf{v}_s) = \hat{n}^a, \quad \forall \mathbf{x} \in \mathcal{B} \times t, \quad (6.35)$$

$$\operatorname{div} \mathbf{T} = \frac{\hat{n}^a \rho^{sR}}{\phi} \mathbf{q}, \quad \forall \mathbf{x} \in \mathcal{B} \times t. \quad (6.36)$$

The Eqs. (6.33-6.35) are obtained using the definition of the partial local mass balance of a constituent  $\varphi^\alpha$  (cf. Eq.(6.10)) as well as the definitions of the reformulated primary variables (cf. Eqs.(6.3-6.4)), the seepage velocity (cf. Eq. (6.7)), the filter velocity (cf. Eq. (6.8)), and Darcy's law (cf. Eq. (6.24)). Due to the concept of superimposed continua, the local partial mass balance is also valid for an arbitrary

subdivision of the unit-cell. To obtain Eq. (6.33) the local mass balance is evaluated for the mixture. For the derivation of Eq. (6.34) the constituent of the suspended particles  $\varphi^a$  and for Eq. (6.35) the constituent of the solid skeleton  $\varphi^s = \varphi^{sa} + \varphi^n$  is considered. Following Steeb *et al.* [81] we obtain Eq. (6.36) by evaluation of the local balance of momentum, cf. Eq. (6.12) for the mixture.

Furthermore, boundary conditions (b.c.'s) are prescribed to close the problem. The Neumann boundary is defined as  $\Gamma_N$  and the Dirichlet boundary as  $\Gamma_D$

$$q = \mathbf{q} \cdot \mathbf{n} = \bar{q}, \quad c \mathbf{q} \cdot \mathbf{n} = \bar{c} q, \quad \mathbf{T} \cdot \mathbf{n} = \bar{\mathbf{t}} \quad \forall \mathbf{x} \in \Gamma_N \times t, \quad (6.37)$$

$$p = \bar{p}, \quad c = \bar{c}, \quad \mathbf{u}_s = \bar{\mathbf{u}}_s \quad \forall \mathbf{x} \in \Gamma_D \times t. \quad (6.38)$$

Note, that only one of both boundary conditions can be applied on the same corresponding boundary. The motivation for the choice of boundary conditions results from the physical interpretation. Prescribing  $q$  and  $c$  on a boundary leads also to a fixed value of  $c \mathbf{q} \cdot \mathbf{n}$ . This approach (Eqs. (6.33-6.36)) captures the solid deformation in the framework of elasto-plastic as also the evolution of hydraulic properties due to infiltration. In addition, initial conditions are prescribed within the calculation domain

$$p = p_0, \quad c = c_0, \quad \phi = \phi_0, \quad \mathbf{u}_s = \mathbf{u}_{s,0} \quad \forall \mathbf{x} \in \mathcal{B}_0 \times T. \quad (6.39)$$

## 6.2.6 Numerical implementation

To obtain a numerical solution of the IBVP described above, Eqs. (6.33-6.39) were implemented in a commercial finite element software (Comsol Multiphysics). To this aim, a weak formulation is derived from the local balance equations. The strong forms (Eqs. (6.33-6.36)) are multiplied by test functions and integrated in space, thus

$$\int_{\mathcal{B}} \delta \phi \operatorname{div}(\phi \mathbf{v}_s) \, d\mathcal{B} = \int_{\mathcal{B}} \delta \phi \hat{n}^a \, d\mathcal{B} \quad (6.40)$$

$$\int_{\mathcal{B}} \frac{k^s}{\eta^{fR}} \operatorname{grad} p \cdot (\delta \operatorname{grad} p) \, d\mathcal{B} + \int_{\mathcal{B}} \delta p \operatorname{div}(\mathbf{v}_s) \, d\mathcal{B} = \int_{\Gamma_q} (\delta p \mathbf{q}) \cdot \mathbf{n} \, d\Gamma_q, \quad (6.41)$$

$$\int_{\mathcal{B}} c \frac{k^s}{\eta^{fR}} \operatorname{grad}(\delta c) \cdot \operatorname{grad}(p) \, d\mathcal{B} + \int_{\mathcal{B}} \delta c [\partial_t(c)\phi + c \partial_t(\phi) - \hat{n}^a] \, d\mathcal{B} \quad (6.42)$$

$$+ \operatorname{grad}(c) \phi \mathbf{v}_s + c \operatorname{grad}(\phi) \mathbf{v}_s + c \phi \operatorname{div}(\mathbf{v}_s)] \, d\mathcal{B} = \int_{\Gamma_c} \delta c \mathbf{q} \cdot \mathbf{n} \, d\Gamma_c,$$

$$\int_{\mathcal{B}} \mathbf{T} : \delta \varepsilon_s \, d\mathcal{B} - \int_{\mathcal{B}} \frac{\hat{n}^a \rho^{sR}}{\phi} \frac{k^s}{\eta^{fR}} \operatorname{grad}(p) \cdot \delta \mathbf{u}_s \, d\mathcal{B} = \int_{\Gamma_{\mathbf{u}_s}} \mathbf{t} \cdot \delta \mathbf{u}_s \, d\Gamma_{\mathbf{u}_s}. \quad (6.43)$$

Intrinsic permeability	$k^s$	$1.02 \times 10^{-12}$	$\text{m}^2$
Effective dyn. viscosity	$\eta^{IR}$	80	$\text{Pa s}$
Dimension of domain	$H$	1	$\text{m}$
Elastic modulus	$E$	1.44	$\text{MPa}$
Poisson's ratio	$\nu$	0.2	
Boundary loading	$\mathbf{t}$	10	$\text{kPa}$

Table 6.1: Material properties and boundary conditions used for the consolidation problem.

Note, that the right hand side (rhs) of Eqs. (6.41-6.43) can be also replaced by boundary conditions, introduced above, cf. Eqs. (6.37, 6.38). In case of homogeneous Neumann boundary conditions the corresponding rhs vanishes. Additionally the weak formulations have to be discretized in time and a numerical solution scheme, e.g. the Newton-Raphson algorithm is used in order to obtain the numerical solution. The plastic equations are solved with an additional Newton-Raphson algorithm.

## 6.3 Validation of the numerical model

### 6.3.1 Mechanical part: validation of the approach using Terzaghi's problem

In this section a validation of the hydro-mechanical infiltration model is presented. In a first step the approach is reduced to capture consolidation and its outcome is compared with the well known Terzaghi's problem.

For the validation of the consolidation modelling presented here, a physical 1-dim numerical example is used and a fully-saturated porous media is considered, cf. Figure 6.3. On three of the four edges of the domain undrained boundary conditions are chosen and displacement of the solid is additionally prescribed to zero. On the remaining edge a drained boundary condition ( $p = 0$ ) is used and additionally a distributed load  $\mathbf{t}$  is applied on the mixture.

This problem is described by the 1-dim pressure diffusion equation proposed by Terzaghi [93], which reads

$$\frac{\partial p}{\partial t} = c_v \frac{\partial^2 p}{\partial z^2}, \quad (6.44)$$

Assuming rigid solid grains ( $\alpha = 1$ ) and incompressible fluid constituent ( $S_p = 0$ ) the consolidation coefficient  $c_v$  is defined as

$$c_v = \frac{k^s(2\mu_s + \lambda_s)}{\eta^{IR}}, \quad (6.45)$$

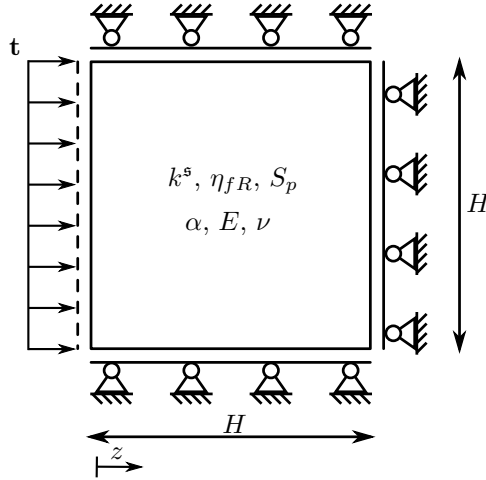


Figure 6.3: Illustration of the 1-dim IBVP and used boundary and initial conditions.

where  $\lambda_s$  and  $\mu_s$  are the Lamé parameters of the solid skeleton, which are directly calculated from  $E$  and  $\nu$ . For this problem, an analytical solution has been developed [19, 102]. Thus, the pressure distribution  $p(t, z)$  in spatial position  $z$  and time  $t$  is written as a infinite series which reads

$$\frac{p(t, z)}{p_0} = \frac{4}{\pi} \sum_{j=1}^{\infty} \left( \frac{(-1)^{j-1}}{2j-1} \cos \left[ (2j-1) \frac{\pi}{2} \left( \frac{H-z}{H} \right) \right] \exp \left[ -(2j-1)^2 \frac{\pi^2}{4} \frac{c_v t}{H^2} \right] \right). \quad (6.46)$$

Additional to the definitions used in Table 6.1,  $p_0$  is the initial pore pressure and corresponds to the boundary load ( $p_0 = \mathbf{t} \cdot \mathbf{n}$ ), in case of the considered Terzaghi's problem. Following Verrujt [102] the consolidation process is assumed to be finished if

$$\frac{c_v t}{H^2} \approx 2. \quad (6.47)$$

when solving the analytical expression in Eq. (6.46) the first 100 terms of the infinite series were considered.

For the numerical calculation, the approach described in the previous part of the contribution was used in a simplified version, to adapt to the analytical calculation. First, the intrinsic permeability is assumed constant during the calculation and is not evolving in time ( $k^s = k_0^s$ ). Therefore, equation (6.25) is neglected. The infiltration process is not accounted for within the Terzaghi's consolidation problem. Thus, the mass exchange is neglected for this problem. To validate the coupling and numerical implementation the mass exchange term is not removed completely, but is set in a range where mass exchange between constituents is neglected  $\hat{n}^a \approx 0$ . The simulation time was limited by Eq. (6.47) to  $t_{\max} = 2H^2/c_v$ .

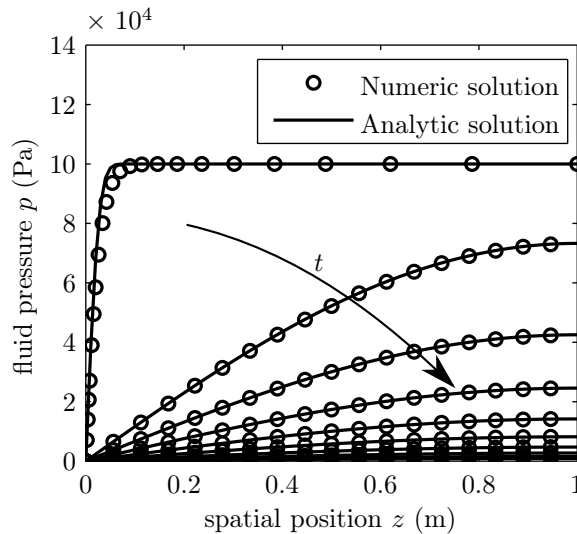


Figure 6.4: Comparison of the analytical and the numerical solution of Terzaghi's consolidation problem. The results of the pressure distribution of both approaches is plotted for the same times. The time step is determined based on the consolidation time  $\Delta t = 0.1 \times t_{\max}$ .

The corresponding results of both approaches are presented in Figure 6.4. There, the pressure distribution is plotted for a cross section along the coordinate  $z$  through the domain, cf. Fig. 6.3. As a result of consolidation the pressure decreases within time, starting from the drained boundary. Both approaches are in good agreement with each other.

### 6.3.2 Hydraulic part: validation with a 0-dim example for infiltration

In this section the hydraulic part of the numerical model is validated with a 0-dim numerical example. The 0-dim calculations are conducted as shown in Figure 6.5. For the numerical approach it is realized as a 1-element FEM implementation. The mechanical part is simulated with restriction of the displacement on all boundaries and a very stiff porous matrix, cf. Table 6.2. For the hydraulic part the upper and lower boundaries are undrained, whereas the other boundaries are drained. Additionally, a material transport is enhanced by prescribing a pressure gradient between the edge on the left and the right edge. To ensure a constant amount of fine particles in the system, periodic boundary conditions for the concentration of fines are used.

However, to match the numerical problem to the analytical one some additional assumptions are required. The mechanical behaviour was validated in the previous example and is therefore of minor interest. Hence, the stiffness of the porous material  $E$  was chosen so high, that deformation of the solid is neglected. Furthermore,

the evolution of the microstructure is not considered in the mass exchange term. Therefore, the mass exchange term reads

$$\hat{n}^a = -c \phi q. \tag{6.48}$$

The analytical solution for the evolution of porosity  $\phi$  in 0-dim is written as

$$n^s(t) = n_0^s - n_0^a (\exp(-Q(t)) - 1), \quad \text{with} \quad Q(t) = \int_{\bar{T}=T_0}^t q(\bar{t}) d\bar{t}. \tag{6.49}$$

In case of a constant filter velocity, e.g. for an infiltration problem driven by Neumann b.c. for  $q$ , this equation is used directly. Here, the filter velocity  $q$  is a result of the hydraulic properties of the medium and the corresponding Dirichlet b.c. for the pressure  $p$ . Hence here, the evolution of the filter velocity can not be derived analytically, it is taken from the numerical solution.

Pressure at boundary	$p_1$	10	k Pa
Pressure at boundary	$p_0$	0	k Pa
Initial concentration	$c$	0.2	
Initial porosity	$\phi$	0.4	
Effective particle size	$D_{\text{eff}}$	0.05	cm
Effective dyn. viscosity	$\eta^{IR}$	80	Pa s
Dimension of domain	$H$	1	m
Elastic modulus	$E$	1.44	G Pa

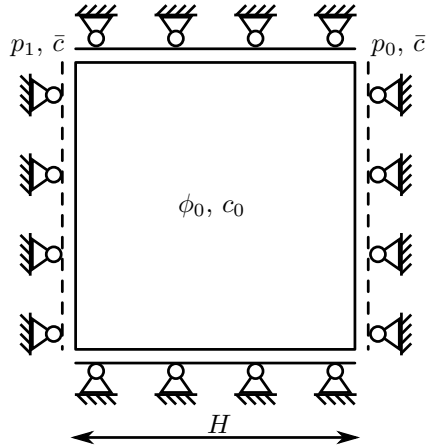


Table 6.2: Material properties and boundary conditions used for the analytical solution of infiltration and the corresponding numerical simulation.

Figure 6.5: IBVP containing initial and boundary conditions for the simulation of 0-dim infiltration.

The results obtained from both approaches are shown in Figure 6.6. The porosity evolves from the initial value  $\phi_0$  to an equilibrium value. As a result of the fact that the amount of fine particles remains constant for all time steps, the final porosity  $\phi_\infty$  is computed to  $\phi_\infty = \phi_0(1 - c_0) = 0.32$ . The evolution of porosity resulting from both approaches match very well to each other and to the final porosity.

### 6.3.3 Validation of the plastic formulation

In this section an analytical solution for a simple Boundary Value Problem (BVP) is presented. After this the numerical approach is adopted and the corresponding results are compared with each other.

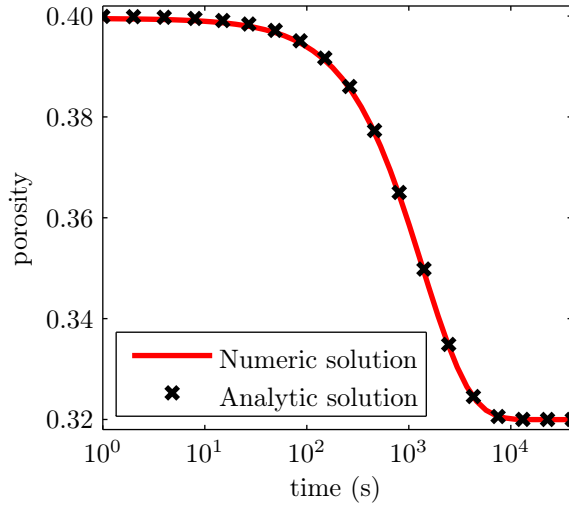


Figure 6.6: Numerical and analytical solution for the time depended evolution of porosity of the 0-dim infiltration approach.

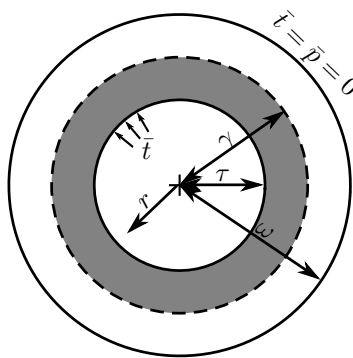


Figure 6.7: Boundary Value Problem (expansion of a cylindrical tube) to compare the numerical approach with an analytical solution in case of ideal plastic yield function using Tresca criterion.

The BVP, which is solved analytically describes an expansion of a cylindrical tube, assuming ideal plasticity, cf. Figure 6.7. A cross-section of a cylindrical tube is characterized by its inner radius  $\tau$  and the outer radius  $\omega$ . Furthermore, a loading  $\bar{t}$  is applied on the inner border, whereas the outer border remains stress free. If the loading  $\bar{t}$  is high enough, the material starts yielding at the point of highest stress, i.e. the inner border of the tube. Therefore, a plastic zone develops starting from the inner border, which is represented by the variable  $\gamma$ . Due to the geometry of the problem, the stress state is described in polar coordinates. The transformation of the corresponding entries of the Cauchy stress tensor  $\mathbf{T}$  is traced back to simple geometrical considerations. Without derivation, following Altenbach *et al.* [1] the components of the Cauchy stress tensor are written as

$$T_{rr} = T_{11} \cos^2 \theta + T_{22} \sin^2 \theta + T_{12} \sin 2\theta, \quad (6.50)$$

$$T_{\theta\theta} = T_{11} \sin^2 \theta + T_{22} \cos^2 \theta - T_{12} \sin 2\theta, \quad (6.51)$$

$$T_{r\theta} = (T_{22} - T_{11}) \sin \theta \cos \theta + T_{12} \cos 2\theta. \quad (6.52)$$

Here, the radius  $r$  and the angle  $\theta$  describe the 2-dim polar coordinate system. The analytical solution that is used here was documented by Hill [40] and partly also by Turner in 1909 [100]. There, ideal plasticity applying the yield criterion of Tresca is employed, as an associated flow rule. In polar coordinates it reads

$$F = T_{\theta\theta} - T_{rr} = \text{const.} \quad (6.53)$$

In this case and using the abbreviation  $Y = T_{\theta\theta} - T_{rr}$ , the stress distribution along the  $r$ -axis is derived. It is distinguished between the plastic and the elastic zone of the material. In the elastic zone the stress distribution ( $\gamma \leq r \leq \omega$ ) is given as

$$\frac{T_{rr}}{Y} = -\frac{\gamma^2}{2\omega^2} \left( \frac{\omega^2}{r^2} - 1 \right), \quad (6.54)$$

$$\frac{T_{\theta\theta}}{Y} = \frac{\gamma^2}{2\omega^2} \left( \frac{\omega^2}{r^2} + 1 \right). \quad (6.55)$$

$$(6.56)$$

In the plastic zone ( $\tau \leq r \leq \gamma$ ) the following formulation is used

$$\frac{T_{rr}}{Y} = -\frac{1}{2} - \ln \left( \frac{\gamma}{r} \right) + \frac{\gamma^2}{2\omega^2}, \quad (6.57)$$

$$\frac{T_{\theta\theta}}{Y} = \frac{1}{2} - \ln \left( \frac{\gamma}{r} \right) + \frac{\gamma^2}{2\omega^2}. \quad (6.58)$$

In order to adapt the numerical results to the analytical solution, a similar BVP was created, cf. Figure 6.7. Additionally to the aforementioned boundary values the fluid pressure of the outer boundary ( $r = \gamma$ ) was set to zero, which represents a drained boundary condition. Furthermore, infiltration was inhibited by choosing

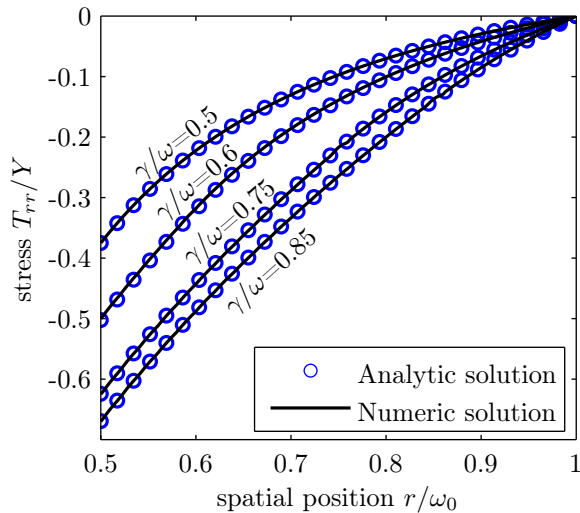


Figure 6.8: Distribution of the radial stress component  $T_{rr}$  in case of different loading conditions for the numerical and the analytical approach.

the corresponding material parameter to be almost zero  $\psi \approx 0$  and the same yielding function, as for the analytical solution was used, cf. Eq. (6.53).

The results of the stress distributions of both, the numerical and analytical approaches, are plotted in the Figures 6.8 and 6.9. Both figures consist of dimensionless graphs. To obtain the stress distribution curves, the parameter  $Y$  was kept constant. In the numerical case the loading  $\bar{t}$  was varied. Hence, the plastic zone  $\gamma$  could be identified as a maximum of the graphs in Figure 6.9. Knowing the size of the plastic zone, it was used to obtain the analytical solution.

In Figure 6.8 the radial stress component  $T_{rr}$  is plotted for the same loading conditions. Here, the development of the plastic zone is visualized as a kink in the stress distribution. However, both, the analytical and the proposed numerical approach, lead to very similar results in the circumferential and the radial stress distribution.

In Figure 6.9 the distribution of the circumferential stress  $T_{\theta\theta}$  is shown for different loading conditions. With increasing load  $\bar{t}$  the size of the plastic zone is increased. Despite yielding of the material takes place, the absolute value of the circumferential stress is also increasing with a higher loading. At the outer boundary,  $r = \omega$ , the equilibrium condition of  $T_{\theta\theta} = 0$  is fulfilled for all times.

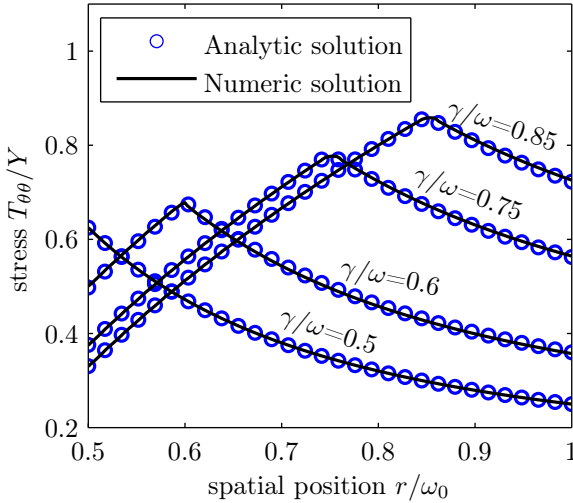


Figure 6.9: Distribution of the circumferential stress component  $T_{\theta\theta}$  in case of different loading conditions for the numerical and the analytical approach.

## 6.4 Numerical results

### 6.4.1 Evolution of mechanical and hydraulic properties in a cross section of a tunnel lining

The following example shows the application of the developed model and all its capabilities in the field of mechanized tunnelling. Therefore, a cross section of a tunnel lining is considered during the grouting process of the annular gap (Figure 6.10). Furthermore, it is illustrated how to transform the physical domain, consisting of the lining, the filled annular gap and the surrounding soil into a numerical simulation model. The lining is not modelled, but is replaced by boundary conditions instead, i.e. a flux is prescribed on the corresponding border. Resulting from the chosen filter velocity, displacements arise that would lead to traction on the boundary of the lining, which means that the tunnel lining is not supporting the material in this case. Since the filling process itself is not captured in this approach, the border of the tunnel lining is chosen to be traction free. The same boundary condition was also chosen for the outer radial border. Furthermore, drained boundary conditions for the convective transport of the suspension, i.e.  $\bar{q}$  and  $\bar{c}$  were chosen. On the other borders symmetry boundary conditions were applied, i.e. undrained conditions and displacements in the tangential directions, only.

To analyse the grouting process, different phenomena of the model were investigated. In general those are:

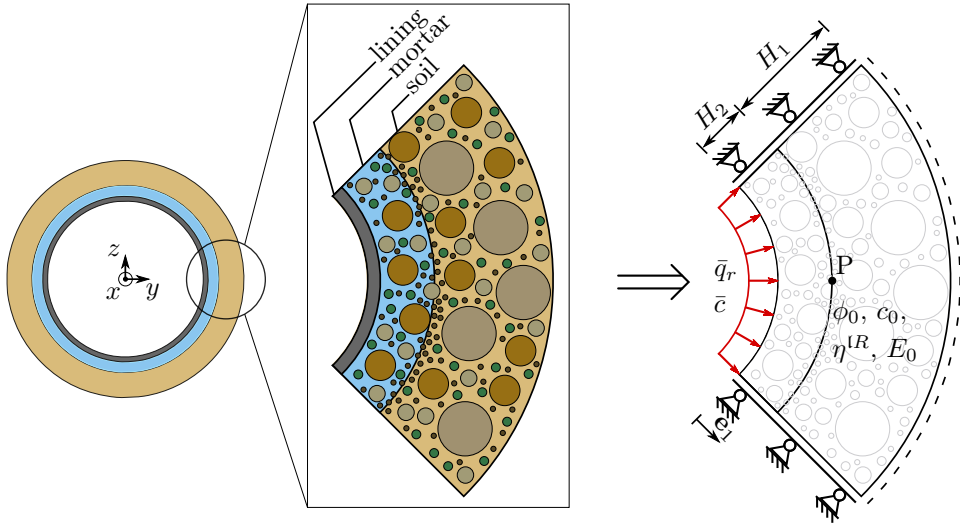


Figure 6.10: From the application (left) to a numerical IBVP (right). Homogenization and boundary conditions for the IBVP.

- *Infiltration*: captures the attachment of fine particles from the suspension to the porous medium.
- *Stiffening*: due to infiltration the volume fraction of the solid constituent increases. This leads to an increase of the stiffness of the porous medium.
- *Plasticity*: captures permanent plastic deformations of the solid skeleton.
- *Consolidation*: poro-elastic approach, simulating the deformation of the solid skeleton resulting from the loading of the grouting process.

Each physical combination of those phenomena has been carried out and is presented in the following. For this, different combinations of aforementioned phenomena were created and are summarized as six different *cases* in Table 6.3.

For the analysis of the mechanical properties of the domain, the radial displacement in point  $P$  was chosen, cf. Figure 6.10. To describe the evolution of the hydraulic properties, the intrinsic permeability along radial direction of the domain was plotted for the last time step at  $t_{pr}$ .

Case	Infiltration	Stiffening	Plasticity	Consolidation
1	X			
2	X	X		X
3	X		X	
4	X	X	X	
5			X	
6	X			X

Table 6.3: Different cases, created to analyse the coupling of different effects and their impact on the evolution of hydraulic and mechanical properties.

### Hydraulic properties:

In Figure 6.11 the evolution of the hydraulic properties, represented by the intrinsic permeability  $k^s$  is plotted. In case 5 no infiltration is considered. Therefore, also stiffening of the material can not be captured and the permeability is not evolving in a broad range. Nevertheless, resulting from the solid-fluid interaction, the permeability decreases due to the pure deformation of the solid. The deformation depends on the local pressure gradient, which is a linear decreasing function evaluated in the radial direction. This is the reason why also the intrinsic permeability is not constant, but a linearly decreasing function. In case 1 the distribution of the intrinsic permeability due to infiltration only is plotted. This means, that all kind of mechanical interaction is neglected. The intrinsic permeability decreases most in the region of the grouting edge, followed by a transition zone of  $\approx 0.3$  m. After that the characteristics is almost constant. The full approach including infiltration, stiffening, and plasticity is represented by case 4. There, the evolution of the intrinsic permeability is similar to case 1, but slightly smaller. This is explained by the deformable solid skeleton and the non constant distribution of tensile stresses. However, the impact of the mechanical properties and its modelling on the hydraulic properties is rather small. Therefore, case 4 represents also the permeability distribution of cases 2, 3, and 6.

### Mechanical properties:

The radial displacement was evaluated at a chosen point  $P$  on the interface between grouting and surrounding soil domain, cf. Figure 6.10. The radial displacement is plotted for all time steps and chosen cases in Figure 6.12. The characteristics of the curve representing case 5 are driven by the consolidation process. As a result of the solid-fluid interaction, the prescribed filter velocity on the inner edge leads to a time depended deformation of the soil. After the porous medium is consolidated the displacement remains constant for all further time steps. In case 3 and case 6, in addition to the consolidation process, infiltration was simulated. In both cases this leads to

higher deformations, which is an result of the infiltration process. Resulting from the decreasing intrinsic permeability, the effective stresses of the solid constituent are increasing, leading to larger deformations. The highest deformations are obtained using an elastic material behaviour (case 6). Considering plasticity (case 3), the increase for the last part of the simulation is smaller, compared to consolidation. If stiffening is considered, it additionally leads to a relativization of the deformations (case 2, case 4). On the one hand infiltration is considered, which enhances the deformations. On the other hand deformations are diminished by stiffening of the solid constituent. Therefore, the combined effect of infiltration and stiffening provides deformations in between of pure consolidation and additional infiltration. The aforementioned impact of plasticity differs the characterizations of the functions of case 2 and case 4.

Initial concentration	$c_0$	0.1	-
Initial porosity	$\phi_0$	0.55	-
Effective particle size	$D_{\text{eff},01}$	0.005	m
Effective dyn. viscosity	$\eta^{IR}$	80	Pa s
Density of solid constituent	$\rho^s$	2000	kg/m <sup>3</sup>
Density of fluid constituent	$\rho^f$	1000	kg/m <sup>3</sup>
Infiltration parameter	$\psi$	30	m
Dimension of domain	$H_1$	0.85	m
Dimension of domain	$H_2$	0.15	m
Elastic modulus of the skeleton	$E_0$	5	MPa
Poisson's ratio of the skeleton	$\nu$	0.2	-
Grouting time	$t_{\text{pr}}$	18000	s
Grout injection flux	$\bar{q}_r$	$3 \times 10^{-5}$	m/s
Kozeny-Carman constant	$C_{\text{KC}}$	5	-
Constant for Eilers equation	$\kappa$	1.3	-
Drucker-Prager constant	$\alpha_{\text{DP}}$	0	-
Drucker-Prager constant	$k_{\text{DP}}$	0.15	MPa

Table 6.4: Material properties and used boundary conditions used for the simulation of the cross section of a tunnel lining illustrated in Figure 6.10.

### Heterogeneous inclusions in the surrounding soil

Extending the numerical example of section 6.4.1, the impact of heterogeneous inclusions in the surrounding soil of the tunnel cross section is demonstrated. For the

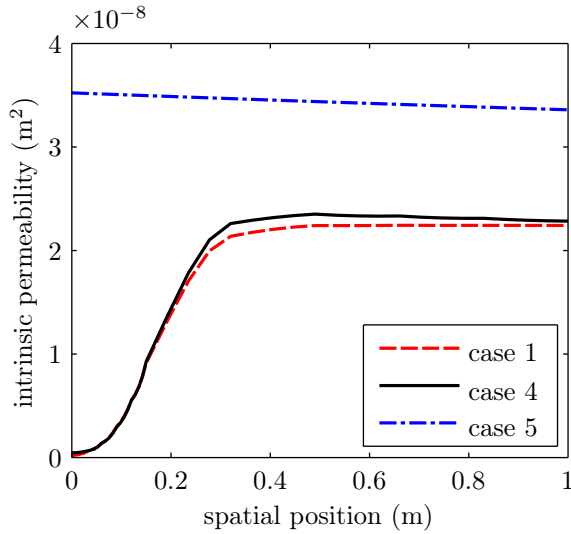


Figure 6.11: Distribution of the intrinsic permeability for the last time step of the simulation along the  $\mathbf{e}_1$  direction, cf. Figure 6.10. The definition of the corresponding cases is given in Table 6.3.

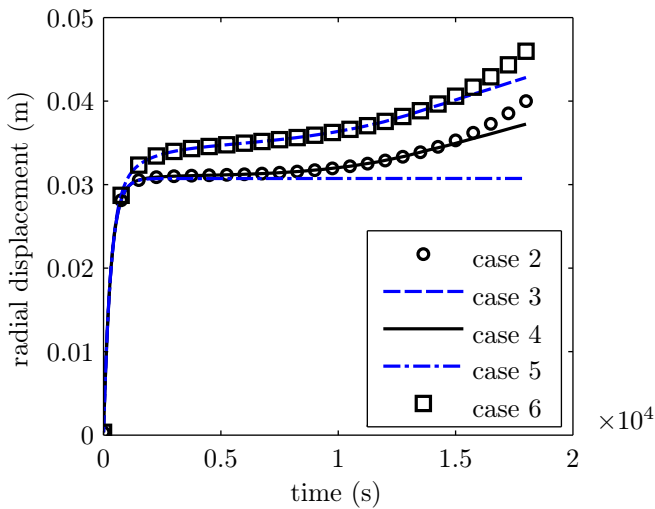


Figure 6.12: Distribution of the displacement of the porous skeleton at a point on the interface of the grout and solid domain for different cases defined in Table 6.3.

conducted numerical example all given definitions in Figure 6.10 and Table 6.4 were used. Additionally arbitrary sized, spherical, and impermeable inclusions were implemented in the calculation domain. Physically, it corresponds to coarse grained material, which are too large for homogenization within the TPM. The numerical implementation was performed by removing the area of the inclusions from the considered domain and replacing it as a spring foundation boundary condition, with the stiffness  $E_{inc} = 10E_0$ , acting normal to the surface boundary of the inclusions. For all other fields no-flux boundary conditions were used.

In Figure 6.13 the results of the calculation are shown by contour plots for the shear modulus of the solid skeleton  $\mu_s$  and the intrinsic permeability  $k_s$  for three different time frames. Initially a lower shear-modulus of the mortar domain compared with the soil domain was chosen. After  $t = 0.41$  h already a first evolution in the shear-modulus is visible. In the grout domain the shear-modulus is increasing homogeneously. In the soil domain the shear-modulus is evolving heterogeneously, as a consequence of the impermeable inclusions. After  $t = 5$  h also in the mortar domain the shear-modulus has a non-constant distribution and its value corresponds at least to the initial shear-modulus in the soil domain. In the soil domain a significant increase of the shear-modulus is observed, especially localized at the interface of the soil and mortar domain.

For the intrinsic permeability a constant distribution in the grout and the soil domain is initially assumed. During the simulation process, a highly non-uniform distribution arises which is characterized on the one hand by the infiltration process and on the other hand by the heterogeneous inclusions.

## 6.5 Discussion

The process of annular gap grouting in context of a tunnel lining is very complex and depends on many coupled effects. For its simulation a simplified IBVP was created in section 6.2.5. As driving quantity of the grouting process the material flux of the suspension was prescribed. It is pointed out that, in practical applications several possibilities for the realization of the grouting process exist. For a deeper understanding of the practical gap grouting it is referred to the publication of Thewes *et al.* [95]. In general, grouting can be continuous or discontinuous. Furthermore, it is distinguished between pressure or flux-driven grouting. Practically, also the experience of the responsible project engineer is of crucial importance, to adjust the pressure and/or flux within the process. Concluding, the here presented example of the grouting process represents only one of many possibilities of annular gap grouting. This means that the findings can be only transferred to similar problems. However, all aforementioned cases of grouting are simulated within the proposed numerical model, by appropriately choosing corresponding boundary conditions.

The results of the numerical example (Figures 6.11, 6.12) show, that the hydraulic properties are not strongly depending on the way of simulating mechanical quantities. The major part of the evolution of the intrinsic permeability is traced back to the

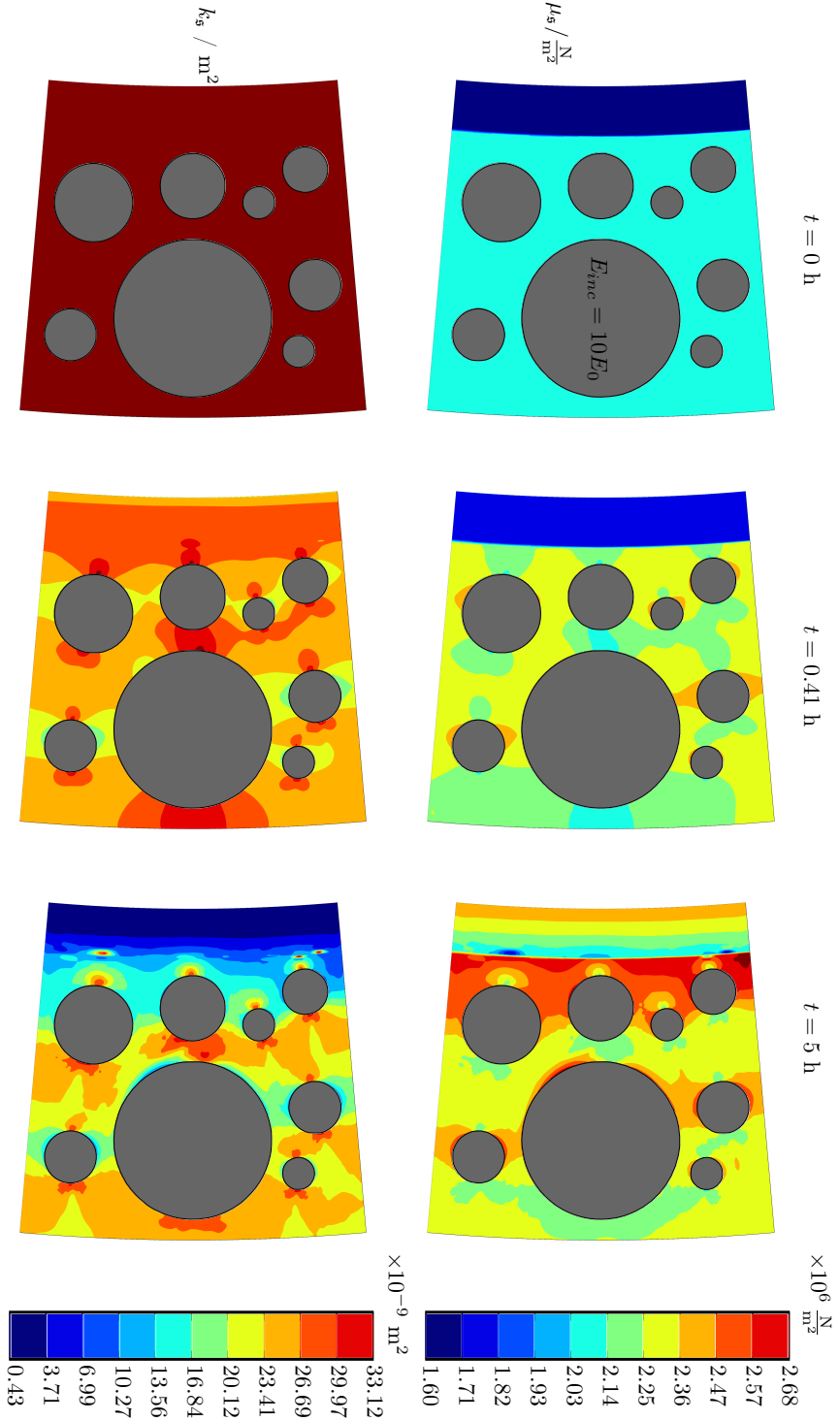


Figure 6.13: Evolution of the shear-modulus (top) and the intrinsic permeability (bottom) during backfilling of the annular gap in heterogeneous domain with impermeable inclusions.

infiltration process. Though, also the deformation of the porous medium, resulting in a variation of the porosity, has an impact on the intrinsic permeability, which is captured within the proposed approach. Considering the numerical simulation of the infiltration, the evolution of the intrinsic permeability mainly depends on the time duration of the grouting process and the microstructure of the mortar/soil system. In this example, the evolution of the intrinsic permeability is localized on the grouting domain and a small part of the soil domain. Overall the formation of a filter cake is observed.

The evolution of mechanical properties results from a more complex coupling of single effects. As soon as the porous medium is considered not to be rigid, where naturally no deformations are possible (case 1), an impact of all described physical effects is observed. In general, simulations neglecting the infiltration process provide the quantitative smallest deformations on the interface of soil and mortar. If infiltration is considered, the largest deformations are observed in simulations neglecting stiffening. Additional consideration of material stiffening leads to a slightly weaker development of the deformation field. If importance of all physically described effects is postulated, the smallest deformations arise (case 5). This is explained by the missing hydro-mechanical coupling. Neglecting the stiffening effect, the prediction of displacements becomes to conservative. Although it is counter-intuitive implementation of a plastic material model leads to smaller deformations at the evaluated interface compared to an elastic model. The proposed model, as implemented with an ideal plastic material behaviour, is surely not suitable for modelling of a realistic soil behaviour. However, using perfect plasticity leads to the lower limit of the material strength, whereas the upper limit is achieved by using an elastic model. Considering the difference in soil deformation between both approaches, e.g. case 2 and case 4, the expected impact of a realistic, more complex soil plasticity model is of minor interest. In principle the usage of such an approach within the here presented model is straightforward.

In case of the simulation represented by Figure 6.13 the impact of impermeable inclusions with a higher stiffness than the surrounding soil were studied. The evolution of the shear-modulus can be traced back on two different phenomena. In the beginning phase the process is dominated by consolidation, which leads to a almost constant distribution of the shear-modulus in the grout domain. After  $t = 5$  h the process is dominated by the infiltration leading to a almost linear distributed shear-modulus in the grout domain and a highly non-uniform distribution in the soil domain. The impact of the impermeable inclusions takes mostly place perpendicular to the flow direction. The evolution of the shear-modulus can be interpreted taking the evolution in the intrinsic permeability into account. The effective cross section is decreased by the impermeable inclusions and thus the filter velocity is increased, which leads to a higher infiltration rate. In the direction of the flow in the region of the inclusions the smallest infiltration rate is observed. Concluding, it can be stated that the demanded shear-modulus in the grout domain is reached by consideration of the consolidation and infiltration process.

## 6.6 Conclusion

A multi-physical numerical approach was presented in this contribution. By use of the continuum-based TPM, the evolution of mechanical and hydraulic properties during the flow of a suspension through a deformable porous medium was described numerically. The proposed approach considered several physical phenomena, which were benchmarked one after the other using broadly used or self developed analytical solutions for unique phenomena. The numerical solutions for individual phenomena are in very good agreement with the corresponding analytical solutions.

Subsequently, a numerical example in the field of mechanized tunnelling was created considering a part of a cross section of a tunnel lining. Neglecting volume forces, rotational symmetry was exploited. Hence, the soil deformation, which corresponds to the settlements, was evaluated at a point on the interface of the soil and grout domain and visualized for all time steps. Furthermore, the intrinsic permeability was evaluated along a cut line through both domains in radial direction for the last time step of the grouting process. By comparing of simulations capturing different combination of the physical phenomena, the coupling and the impact of single modelling features on the overall process was obtained. Furthermore, the practical use of the derived approach was demonstrated by a numerical example with heterogeneous impermeable inclusions. It could be shown that the demanded mechanical properties can be reached with cement-free grouting mortar by a de-watering process induced by a flux driven backfilling of the annular gap.

# Chapter 7

## Concluding remarks

*In this last chapter of the work, the results obtained in the previous chapters are discussed and concluded. The main findings are related to the annular gap grouting procedure, which was described in the introduction of Chapter 2. After this, the work is summarized and possible fields for further investigations and open questions are presented.*

### 7.1 Discussion and conclusion

The scope of this work, presented in Chapter 1, was to develop numerical models for the simulation of the annular gap grouting process in mechanized tunnelling. After that, Chapter 2 was focussed on the technical details of the annular gap grouting process in engineering practise. The theoretical framework of the TPM for the development of the numerical models capturing the grouting process was presented in Chapter 3. The most important physical properties have been identified and simulated using an extended approach of the TPM. This allows to simulate infiltration during the hydro-mechanically coupled gap-grouting procedure. The developed approach is formulated on the continuum scale including the evolution of the morphology on the micro scale.

Chapter 4 of this thesis was focussed on the infiltration process discussing the evolution of hydraulic properties from a mesoscopic perspective. The performed numerical investigations have an 1-dim character, although numerically implemented in 2-dim. In order to capture infiltration phenomena, a thermodynamically-consistent production term was introduced, containing one material parameter  $k$ , which remains constant within the ongoing infiltration process in the whole calculation domain. For the conducted numerical example an equilibrium concentration was observed, induced by this material parameter  $k$ . This concentration is not evolving in time although hydraulic properties of the domain were varied. For small values of the material parameter for infiltration  $k < 0.02$ , a linear behaviour of the equilibrium concentration was found, which could be described by means of a master curve.

The convection dominated characteristic of the infiltration process was identified where a steep gradient of concentration within the numerical example was observed. This was supported by the assumption that the suspended particles penetrate the porous domain with fluid velocity  $\mathbf{v}_f$ . This means, that the relative velocity between the constituent of suspended particles  $\varphi^a$  and the fluid constituent  $\varphi^f$  was neglected.

In Chapter 5 a more sophisticated approach to evaluate the mass/volume exchange, in order to determine the infiltration behaviour, was developed. Thus, the four-phase approach developed in Chapter 4 was extended to a  $(2f + 1)$  field formulation by introducing a further homogenization level with the concept of species. Three phases were considered, where two of those are subdivided into  $f$  species, which correspond to the discrete grading ranges obtained from sieving analysis of the solid skeleton and the suspended particles. Hence, these species have a physical interpretation and can be extracted straightforward from geotechnical standard characterization methods. This leads to  $f$  different production terms  $\hat{n}_i^a$ , which are not constant values but evolve in time. For the numerical realization, a statistical approach was used, comparing the suspended particle grading ranges with the constriction sizes of the porous skeleton. The infiltration behaviour was simulated using this geometrical approach. The GSD of the suspended particles and the GSD of the solid skeleton vary in time and space, due to the infiltration process. This means that the heterogeneous characteristics of infiltration phenomena can be simulated with that methodology. Furthermore, an analytical approach to capture infiltration phenomena for simplified problems was carried out. For its application, the heterogeneous infiltration problem was simplified to obtain a physical but spatial homogeneous numerical domain.

In Chapter 6 the multi-field approach was extended by the consideration of the balance of momentum of the mixture. In addition, the concept of effective stress was taken into account, which allows to describe the deformations of the solid skeleton. Therefore, infiltration and consolidation were captured by the modelling approach described in Chapter 6, leading to a more realistic simulation of the gap grouting process in mechanized tunnelling. To account for the mechanical properties of the annular gap and of the surrounding soil, a stiffening parameter  $a$  was introduced. This parameter is not an additional unknown, but prescribed within the multi-field formulation as the amount of particles attached to the solid skeleton. A linear correlation between the material stiffness and the amount of attached particles was assumed, which led to a qualitative description of the process. The performed numerical investigations were focussed on the gap grouting process in mechanized tunnelling. Numerically, simulations have been carried out observing the mechanical and hydraulic properties of cement-free mortar during the dewatering process. It was shown numerically that the central requirement for achieving a material stiffness of the grouting mortar, which corresponds to the material stiffness of the surrounding soil in the primary stress state, was fulfilled by the dewatering process. Although the requirements on the grouting mortar are generally formulated with respect to mechanical properties, it has been shown that the simulation of mechanical properties alone is not sufficient to correctly capture the physics. In fact, the hydro-mechanical coupling is crucial

and can not be neglected. The mechanical properties are significantly evolved by the evolution of the hydraulic properties. Infiltration and formation of a filter cake at the interface of soil and grout lead to a substantial impact on the material stiffness of the annular gap grouting mortar.

For a numerical experiment induced by a pressure gradient, a local decrease of hydraulic conductivity, which is traced back to infiltration, induces a higher filter velocity in the remaining part of the cross section (Chapter 4). The proportionality of the production term  $\hat{n}^a$  to the absolute value of the filter velocity  $|\mathbf{q}|$  leads to a higher infiltration rate and a faster decrease in the hydraulic conductivity. In the approach conducted in Chapter 5 this effect was enhanced by the evolution of the production term with respect to the spatial position and the time of the calculation process. Hence, the decrease in hydraulic conductivity even enhances infiltration, which is motivated by the smaller pore constrictions. This leads to a more realistic simulation of clogging phenomena, as for example the formation of a filter cake.

Furthermore, a more realistic description of the suspension was obtained in the approaches of Chapters 5 and 6 by the consideration of Eilers equation, cf. Eqs.(5.30, 6.23), which is valid not only for dilute but also for dense suspensions, instead of the evolution equation proposed by Einstein, cf. Eq. (4.24). The higher accuracy of the Eilers equation is a result of the highly non-linear evolution of the effective dynamic viscosity of the suspension  $\eta^{\text{IR}}$  with respect to the concentration  $c$ , especially for larger values of the concentration.

Next, different possibilities for the interpretation of the Kozeny-Carman equation are discussed within the single modelling approaches. In the calculations in Chapters 4 and 6 the material parameter of the Kozeny-Carman equation, the effective particle diameter, was assumed to be constant. In Chapter 5 the effective particle diameter was not understood as an input parameter, which has to be prescribed, but it was calculated directly from the GSD of the solid skeleton. Due to the evolution of the GSD of the solid skeleton, the effective particle diameter was recalculated for each integration point in each time step.

Comparing the here proposed modelling approach of infiltration phenomena to investigations capturing erosion using the TPM, cf. Bonelli and Marot [14] or Steeb *et al.* [85], it can be stated that the obtained field equations are similar. This means the differentiation, between infiltration or erosion is captured with a particular numerical approach, is determined by the constitutive formulation, e.g. for the mass exchange term  $\hat{n}^a$ . In case of modelling clogging effects, as described in this thesis, this differentiation is straightforward. In other research fields, e.g. dam construction, both phenomena, i.e. infiltration and erosion, are observed at different locations at the same time. Hence, it is not obvious whether infiltration, erosion, or both phenomena occur if a convective transport of a suspension through a porous domain is considered. This point could be a potential field of further research activities. A numerical approach could be created, which does not a priori differentiate between erosion and infiltration. Instead, this could be a result of the local morphology of

the considered domain. For this, the filter stability in each material point could be evaluated, e.g. using methods proposed by Kenney and Lau [50].

As described in Chapter 2, the numerical models developed in this work are suited to capture the continuous grouting process. For discontinuous grouting, the numerical model has to be adapted. Despite the fact that the continuous grouting procedure leads to the best bedding of the tunnel lining and to the smallest surface settlements above the tunnel, discontinuous grouting is still used in engineering practise. Thus, this process could be investigated numerically in further research activities. In case of continuous grouting it is convenient to assume a (weakly) developed solid skeleton of the grouting mortar in the annular gap in the initial phase of the grouting process. Therefore, the grouting mortar and the solid domain can be described as a porous medium using the TPM during the entire simulation. For the discontinuous grouting procedure this assumption is not valid. Initially, the characteristics of the mortar are dominated by a low shear-modulus, and therefore, by a fluid like behaviour. During the grouting process the properties of the mortar change due to the development of grain to grain contacts and dewatering. From this point on, simulation of the grouting process can be realized with the numerical models presented in this work. Before the development of the grain to grain contacts, a flow simulation is required that captures the filling process of the discontinuous grouting. For this, the evolution of a free surface boundary of the domain representing the mortar has to be considered.

The numerical approaches presented in this work were focussed on the application of cement-free grouting mortar. Also standard (cement-containing) mortars or 2-component mortars are of industrial importance for tunnelling projects in granular soil. Therefore, further research with focus on those materials could lead to a comprehensive numerical toolbox for engineering practise.

Concluding, the presented numerical models lead to a deeper physical understanding of the grouting process in mechanized tunnelling. The proposed simulation models can be understood as basic research with a special focus on the industrial application. Although further investigations, especially in the experimental field, are required, the proposed numerical approaches capture the physical phenomena of the grouting process in mechanized tunnelling. The proposed models lead to a more accurate simulation of the applicability of cement-free mortars for particular tunnelling projects.

# Bibliography

- [1] H. Altenbach, J. Altenbach, and K. Naumenko. *Ebene Flächentragwerke: Grundlagen der Modellierung und Berechnung von Scheiben und Platten*. Springer Berlin Heidelberg, 1998.
- [2] S. Babendererde. Grouting the shield tail gap behind a tunnelling machine with segmental lining. *Tunnels & Tunneling International*, 11:48–49, 1999.
- [3] L. Bennethum and J. Cushman. Multicomponent, multiphase thermodynamics of swelling porous media with electroquasistatics: I. Macroscale field equations. *Transport in porous media*, 47:309–336, 2001.
- [4] L. Bennethum and J. Cushman. Multicomponent, multiphase thermodynamics of swelling porous media with electroquasistatics: II. constitutive theory. *Transport in Porous Media*, 47:337–362, 2001.
- [5] A. Bertram. *Elasticity and plasticity of large deformations: An introduction*. Springer Berlin Heidelberg, 2005.
- [6] J. Betten. *Kontinuumsmechanik*. Springer Vieweg, 2001.
- [7] A. Bezuijen. Foam used during EPB tunnelling in saturated sand, parameters determining foam consumption. In *World Tunnel Congress*, pages 267–269, 2011.
- [8] A. Bezuijen and A. M. Talmon. Processes around a TBM. In *Geotechnical Aspects of Underground Construction in Soft Ground*, pages 3–13, 2009.
- [9] A. Bezuijen and A. Talmon. Grout pressures around a tunnel lining, influence of grout consolidation and loading on lining. In *Tunnelling. A Decade of Progress. GeoDelft 1995-2005*, pages 109–114. Taylor & Francis, 2005.
- [10] M. A. Biot. General theory of three-dimensional consolidation. *Journal of Applied Physics*, 12:155–164, 1941.
- [11] M. A. Biot and D. Willis. The Elastic Coefficients of the Theory of Consolidation. *Journal of Applied Mechanics for December*, pages 594–601, 1957.

- 
- [12] J. Bluhm, R. de Boer, and J. Skolnik. Allgemeine Plastizitätstheorie für poröse Medien. In *Forschungsbericht aus dem Fachbereich Bauwesen 73*. 1996.
- [13] R. D. Boer. *Trends in continuum mechanics of porous media. Theory and Applications of Transport in Porous Media*. Springer Netherlands, 2006.
- [14] S. Bonelli and D. Marot. On the modelling of internal soil erosion. In *International Association for Computer Methods and Advances in Geomechanics*, pages 2544–2550, 2008.
- [15] D. F. Boutt, B. K. Cook, and J. R. Williams. A coupled fluid - solid model for problems in geomechanics: Application to sand production. *International Journal for Numerical and Analytical Methods in Geomechanics*, 35:997–1018, 2011.
- [16] R. M. Bowen. Incompressible porous media models by use of the theory of mixtures. *International Journal of Engineering Science*, 18:1129–1148, 1980.
- [17] R. M. Bowen. Compressible porous media models by use of the theory of mixtures. *International Journal of Engineering Science*, 20:697–735, 1982.
- [18] W. D. Carrier. Goodbye, Hazen; Hello, Kozeny-Carman. *Journal of Geotechnical and Geoenvironmental Engineering*, 129:1054–1056, 2003.
- [19] H. Carslaw and J. Jaeger. *Conduction of heat in solids*. Oxford Science Publications, 1986.
- [20] M. A. Carter, K. M. Green, M. A. Wilson, and W. D. Hoff. Measurement of the water retentivity of cement mortars. *Advances in Cement Research*, 15:155–159, 2003.
- [21] B. D. Coleman and W. Noll. The thermodynamics of elastic materials with heat conduction and viscosity. *Archive for Rational Mechanics and Analysis*, 13:167–178, 1963.
- [22] O. Coussy. *Poromechanics*. John Wiley & Sons, Ltd, 2005.
- [23] L. Cui, V. Kaliakin, Y. Abousleiman, and A.-D. Cheng. Finite element formulation and application of poroelastic generalized plane strain problems. *International Journal of Rock Mechanics and Mining Sciences*, 34:953–962, 1997.
- [24] R. de Boer. *Theory of Porous Media: Highlights in Historical Development and Current State*. Springer Springer Berlin Heidelberg, 2000.
- [25] R. de Boer and W. Ehlers. The Development of the Concept of effective stresses. *Acta Mechanica*, 83:77–92, 1990.
- [26] D. A. Drew and S. L. Passman. *Theory of multicomponent fluids*. Springer-Verlag, Berlin, 1999.

- [27] D. C. Drucker and W. Prager. Soil mechanics and plastic analysis for limit design. *Quarterly of Applied Mathematics*, 10:157–165, 1952.
- [28] W. Ehlers. Grundlegende Konzepte in der Theorie Poröser Medien. *Technische Mechanik*, 16:63–76, 1996.
- [29] W. Ehlers. Foundations of multiphase and porous materials. In *Porous Media*, pages 3–86. Springer Berlin Heidelberg, 2002.
- [30] W. Ehlers and J. Bluhm. *Porous media: theory, experiments, and numerical applications*. Springer, 2002.
- [31] H. Eilers. Die Viskosität von Emulsionen hochviskoser Stoffe als Funktion der Konzentration. *Kolloid-Zeitschrift*, 97:313–321, 1941.
- [32] H. Eilers. Die Viskositäts- Konzentrationsabhängigkeit kolloider Systeme in organischen Lösungsmitteln. *Kolloid-Zeitschrift*, 102:154–169, 1943.
- [33] A. Einstein. Eine neue Bestimmung der Moleküldimensionen. *Annalen der Physik*, 324:1–22, 1906.
- [34] S. Ergun and A. Orning. Fluid flow through randomly packed columns and fluidized beds. *Industrial & Engineering Chemistry*, 41:1179–1184, 1949.
- [35] J. Fillibeck. Prognose von Oberflächensetzungen beim Tunnelvortrieb - Teil II: Möglichkeiten und Grenzen der Finite-Element-Berechnung. *Geotechnik*, 36: 104–112, 2013.
- [36] J.-J. Fry, T. Julínek, and J. Ríha. Internal Erosion in Embankment Dams and their Foundations. In *Papers from the conference and workshop on Internal Erosion in Embankment Dams and Their Foundation, Brno, Czech Republic, April 26th to 29th 2011*, 2011.
- [37] R. Glantz and U. Schuler. Construction of a pore network on the basis of three dimensional Nuclear Magnetic Resonance (NMR) images. In *Proceedings 2nd Int. Conf. Geofilters '96*, Montreal, 1996.
- [38] M. Goltz, T. Etzer, M. Aufleger, and P. Muckenthaler. Assessing the critical seepage velocity causing transport of fine particles in embankment dams and their foundation. In *Modern Technologies and Long Term Behavior of Dams*, pages 466–471, 2011.
- [39] T. Hashimoto, J. Brinkman, T. Konda, and A. Feddema. Simultaneous backfill grouting, pressure development in construction phase and in the long-term. In *Tunnelling. A Decade of Progress. GeoDelft 1995-2005*, pages 101–107. Taylor & Francis, 2006.
- [40] R. Hill. *The mathematical theory of Plasticity*. Oxford University Press, 1967.

- [41] U. Homberg, D. Baum, S. Prohaska, U. Kalbe, and K. J. Witt. Automatic extraction and analysis of realistic pore structures from  $\mu$ CT Data for pore space characterization of graded soil. In *International Conference on Scour and Erosion*, pages 345–352, 2012.
- [42] T. J. R. Hughes. *The Finite Element Method, Linear Static and Dynamic Finite Element Analysis*. Dover, 2000.
- [43] B. Indraratna and A. K. Raut. Enhanced criterion for base soil retention in embankment dam filters. *Journal of Geotechnical and Geoenvironmental Engineering*, 132:1621–1627, 2006.
- [44] B. Indraratna and S. Radampola. Analysis of critical hydraulic gradient for particle movement in filtration. *Journal of Geotechnical and Geoenvironmental Engineering*, 128:347–350, 2002.
- [45] B. Indraratna and A. K. Raut. Mathematical modelling of granular filters in embankment dams. In *International Conference on Filters and Drainage in Geotechnical and Environmental Engineering*, pages 95–106, 2004.
- [46] S. Irmay. On the theoretical derivation of Darcy and Forchheimer formulars. *Trans. Am. Geophysical Union*, 39:702–707, 1958.
- [47] M. Jung and U. Langer. *Methode der finiten Elemente für Ingenieure*. 2013.
- [48] T. Kasper and G. Meschke. A numerical study of the effect of soil and grout material properties and cover depth in shield tunnelling. *Computers and Geotechnics*, 33:234–247, 2006.
- [49] T. C. Kenney, R. Chahal, E. Chiu, G. I. Ofoegbu, G. N. Omenge, and C. A. Ume. Controlling constriction sizes of granular filters. *Canadian Geotechnical Journal*, 22:32–43, 1985.
- [50] T. Kenney and D. Lau. Internal stability of granular filters. *Canadian Geotechnical Journal*, 22:215–225, 1985.
- [51] B. Klein. *FEM, Grundlagen und Anwendungen der Finite-Element-Methode im Maschinen- und Fahrzeugbau*. Springer Vieweg, 2015.
- [52] H. W. Kuhn and A. W. Tucker. Nonlinear programming. In *Proceedings of the Second Berkeley Symposium on Mathematical Statistics and Probability*, pages 481–492. University of California Press, 1951.
- [53] J. F. Labuz and A. Zang. Mohr-Coulomb failure criterion. *Rock Mechanics and Rock Engineering*, 45:975–979, 2012.
- [54] E. Leca and B. New. Settlements induced by tunneling in soft ground. *Tunnelling and Underground Space Technology*, 22:119–149, 2007.

- [55] T. Lehmann. *Elemente der Mechanik II: Elastostatik*. Vieweg+Teubner Verlag, 1975.
- [56] M. Link. *Finite Elemente in der Statik und Dynamik*. Springer Vieweg, 2014.
- [57] M. Locke, B. Indraratna, and G. Adikari. Time-Dependent Particle Transport through Granular Filters. *Journal of Geotechnical and Geoenvironmental Engineering*, 127:521–529, 2001.
- [58] B. Maidl, M. Herrenknecht, U. Maidl, and W. G. *Maschinelles Tunnelbau im Schildvortrieb*. Ernst & Sohn, 2011.
- [59] M. Merkel and A. Öchsner. *Eindimensionale Finite Elemente, Ein Einstieg in die Methode*. Springer-Verlag Berlin Heidelberg, 2014.
- [60] G. Meschke. Consideration of aging of shotcrete in the context of a 3D viscoplastic material model. *International Journal for Numerical in Engineering*, 39:3123–3143, 1996.
- [61] G. Meschke, C. Kropik, and H. Mang. Numerical analyses of tunnel linings by means of a viscoplastic material model for shotcrete. *International Journal for Numerical Methods in Engineering*, 39:3145–3162, 1996.
- [62] J. Ninić and G. Meschke. Model update and real-time steering of tunnel boring machines using simulation-based meta models. *Tunnelling and Underground Space Technology*, 45:138–152, 2015.
- [63] E. Papamichos, I. Vardoulakis, J. Tronvoll, and A. Skjirstein. Volumetric sand production model and experiment. *International Journal for Numerical and Analytical Methods in Geomechanics*, 25:789–808, 2001.
- [64] H. Pfletschinger, I. Engelhardt, M. Piepenbrink, F. Königer, R. Schuhmann, A. Kallioras, and C. Schüth. Soil column experiments to quantify vadose zone water fluxes in arid settings. *Environmental Earth Sciences*, 65:1523–1533, 2012.
- [65] M. Ramoni, N. Lavdas, and G. Anagnostou. Squeezing loading of segmental linings and the effect of backfilling. *Tunnelling and Underground Space Technology*, 26:692–717, 2011.
- [66] N. Reboul, E. Vincens, and B. Cambou. A computational procedure to assess the distribution of constriction sizes for an assembly of spheres. *Computers and Geotechnics*, 37:195–206, 2010.
- [67] N. Reboul, E. Vincens, and B. Cambou. Analytical model for constriction size distributions of granular materials. In *Modern Technologies and Long-term Behavior of Dams*, pages 264–269, 2011.

- [68] N. Reboul, E. Vincens, and B. Cambou. A statistical analysis of void size distribution in a simulated narrowly graded packing of spheres. *Granular Matter*, 10:457–468, 2008.
- [69] J. C. Santamarina and J. Jang. Energy geotechnology: Implications of mixed fluid conditions. In *Proceedings of the 5th International Conference on Unsaturated Soils*, pages 33–50, 2011.
- [70] A. Schaufler, C. Becker, H. Steeb, and A. Scheuermann. A continuum model for infiltration problems. In *International Conference on Scour and Erosion*, pages 663–670, 2012.
- [71] A. Schaufler, C. Becker, and H. Steeb. Infiltration processes in cohesionless soils. *ZAMM - Journal of Applied Mathematics and Mechanics*, 93:138–146, 2013.
- [72] A. Schaufler and H. Steeb. Transport and infiltration of suspensions through porous media. *International Journal for Numerical and Analytical Methods in Geomechanics*, (under review), 2015.
- [73] A. Schaufler, C. Becker, H. Steeb, and A. Scheuermann. Simulation of the backfilling process with annular gap grouting mortar. In *Proceedings of the Third International Conference on Computational and Subsurface Engineering*, pages 587–597, 2013.
- [74] J. Schröder. *Plasticity and beyond*. Springer, 2014.
- [75] U. Schuler. *Bemessung von Erdstoff-Filtern unter besonderer Berücksichtigung der Parameterstreuung*. Dissertation, Universität Fridericiana in Karlsruhe, 1997.
- [76] L. Schwartz, D. Wilkinson, M. Bolsterli, and P. Hammond. Particle filtration in consolidated granular systems. *Physical Review B*, 47:4953–4960, 1993.
- [77] J. N. Shirlaw, D. P. Richards, P. Ramond, and P. Longchamp. Recent experience in automatic tail void grouting with soft ground tunnel boring machines. In *ITA-AITES World Tunnel Congress Singapore*, pages 446–453, 2004.
- [78] A. Silveira. An analysis of the problem of washing through in protective filters. In *6th International Conference on Soil Mechanics and Foundation Engineering*, volume 3, pages 551–555, 1965.
- [79] J. Simo and T. Hughes. *Computational Inelasticity*. Springer New York, 1998.
- [80] H. Steeb and S. Diebels. A thermodynamic-consistent model describing growth and remodeling phenomena. *Computational Materials Science*, 28:597–607, 2003.

- [81] H. Steeb, S. Diebels, and I. Vardoulakis. Sand production: A microscopically motivated multi-phase model. In *Proceedings of Powder & Grains 2005, University of Stuttgart*, pages 723–726, 2005.
- [82] H. Steeb. *Non-Equilibrium Processes in Porous Media*. Habilitation, Saarland University, 2008.
- [83] H. Steeb. Internal erosion in gas-flow weak conditions. In J. Goddard, P. Giovine, and J. T. Jenkins, editors, *AIP Conference Proceedings*, volume 1227, pages 115–134, 2010.
- [84] H. Steeb and J. Renner. Modeling of Fluid Transport in Geothermal Research. In *Handbook of Geomathematics*, pages 1–55. Springer Berlin Heidelberg, 2014.
- [85] H. Steeb, S. Diebels, and I. Vardoulakis. A multiphase continuum-based model capturing erosion and deposition. In *Proceedings of: International Symposium on Trends in Applications of Mathematics to Mechanics*, 2004.
- [86] H. Steeb, S. Diebels, and I. Vardoulakis. Modeling Internal Erosion in Porous Media. In *Geo-Denver 2007: New Peaks in Geotechnics*, pages 1–10, 2007.
- [87] H. Steeb, P. S. Kurzeja, and S. M. Schmalholz. Wave propagation in unsaturated porous media. *Acta Mechanica*, 225:2435–2448, 2014.
- [88] E. Stehlik, D. Cyron, P. Hybsky, and P. Rennkamp. EPBM two component grouting - problems and solutions. In *Proceedings of the ITA-AITES World Tunnel Congress*, 2012.
- [89] G. Swoboda. Three-Dimensional Numerical Modelling for TBM Tunnelling in Consolidated Clay. *Tunneling and Underground Space Technology*, 14:327–333, 1999.
- [90] A. Talmon and A. Bezuijen. Simulating the consolidation of TBM grout at Noordplaspolder. *Tunnelling and Underground Space Technology*, 24:493–499, 2009.
- [91] A. Talmon, L. Aaanen, A. Bezuijen, and W. van der Zon. Grout pressures around a tunnel lining. In *Modern Tunneling Science and Technology*, pages 817–821. Swets & Zeitlinger, 2001.
- [92] K. Terzaghi and R. Jelinek. *Theoretische Bodenmechanik*. Springer Berlin Heidelberg, 1954.
- [93] K. Terzaghi. *Erdbaumechanik auf bodenphysikalischer Grundlage*. Deuticke, Wien, 1925.
- [94] K. Terzaghi and R. B. Peck. *Soil mechanics in engineering practice*. John Wiley & Sons, Inc., 1948.

- [95] M. Thewes and C. Budach. Mörtel im Tunnelbau. *BauPortal*, 12:706–711, 2009.
- [96] M. Thewes and C. Budach. Grouting of the annular gap in shield tunnelling - an important factor for minimisation of settlements and production performance. In *Proceedings of the 35th ITA World Tunnel Congress, Budapest*, pages 1–9, 2009.
- [97] C. Thienert. *Zementfreie Mörtel für die Ringspaltverpressung beim Schildvortrieb mit flüssigkeitsgestützter Ortsbrust*. Dissertation, Bergische Universität Wuppertal, 2011.
- [98] C. Truesdell. *Rational Thermodynamics*. Springer-Verlag, 1985.
- [99] C. A. Truesdell. *Sulle basi della termomeccanica I & II*. translated into english in: C. Truesdell (Editor), *Continuum Mechanics II-IV*, Gordon & Breach, New York, 1966. *Atti Accad Naz. Lincei. Rend. Cl. Sci. Fis. Mat. Nat.* 22, pp. 33-38 and pp. 158-166, 1957.
- [100] L. Turner. The stresses in a thick hollow cylinder subjected to internal pressure. *Trans. Camb. Phil. Soc.*, 21:377–396, 1909.
- [101] I. Vardoulakis, P. Papanastasiou, and M. Stavropoulou. Sand erosion in axial flow conditions. *Transport in Porous Media*, 45:267–281, 2001.
- [102] A. Verrujt. *An Introduction to Soil Dynamics*. Springer Dordrecht Heidelberg London New York, 2010.
- [103] E. Vincens, K. Witt, and U. Homberg. Approaches to Determine the Constriction Size Distribution for Understanding Filtration Phenomena in Granular Materials. *Acta Geotechnica*, 1:1–13, 2014.
- [104] R. Von Mises. Mechanik der festen Körper im plastisch-deformablen Zustand. *Göttin. Nachr. Math. Phys.*, 1:582–592, 1913.
- [105] K. J. Witt. *Filtrationsverhalten und Bemessung von Erdstoff-Filtern*. Dissertation, Universität Fridericiana in Karlsruhe, 1986.
- [106] W. Wittke. Besonderheiten bei schildvorgetriebenen Tunneln im Sedimentgestein. In *Felsmechanik und Tunnelbau*, pages 634–638, 2012.
- [107] L. Wu, B. N. Nzouapet, E. Vincens, and S. Bernat-Minana. Laboratory experiments for the determination of the constriction size distribution of granular filters. In *International Conference on Scour and Erosion*, pages 233–240, 2012.
- [108] H. S. Yu. *Plasticity and Geotechnics*. Advances in Mechanics and Mathematics. Springer US, 2007.
- [109] Y. Zheng, R. Burridge, and D. Burns. Reservoir Simulation with the Finite Element Method Using Biot Poroelastic Approach. *Technology*, 1:1–20, 2003.

- 
- [110] J. Zhuang, J. S. Tyner, and E. Perfect. Colloid transport and remobilization in porous media during infiltration and drainage. *Journal of Hydrology*, 377: 112–119, 2009.
- [111] J. Ziems. *Beitrag zur Kontakterosion nichtbindiger Erdstoffe*. Dissertation, Technische Universität Dresden, 1968.



## Curriculum Vitae

### Work experience

- 04/2011 – 06/2015    **Research associate**  
**Chair of continuum mechanics**  
**Ruhr-University Bochum**  
**PhD-topic:** *Multi-physical simulations: transport and infiltration of suspensions in granular porous media*
- 06/2008 – 03/2011    **Undergraduate research associate**  
**Chair of continuum mechanics**  
**Ruhr-University Bochum**  
Numerical simulation of fracture propagation (fracture mechanics)

### National and international practical experience

- 10/2012 – 11/2012    **The University of Queensland, Brisbane, Australia**  
& 10/2011 – 11/2011    **Occupational trainee**  
Numerical simulations and material tests of flow processes in heterogeneous media
- 04/2010 – 07/2010    **MAN Diesel & Turbo SE, Oberhausen, Germany**  
**Internship**  
Development of numerical tools for process automation  
**Student research project:** *Calculation of axial thrust for industrial radial compressors*  
**Grade: 1,1**
- 02/2008-04/2008    **Buchwald GmbH Steelworks, Bochum, Germany**  
**Internship**

### Education

- 10/2006 – 03/2011    **Mechanical Engineering (Dipl.) | Ruhr-University Bochum**  
**Major field of study:** Applied mechanics  
**Diploma thesis:** *Theoretical and experimental investigations of thermo-mechanical properties of polymers under large deformations*  
**Grade: 1,0**  
**Final grade: 1,2 (Graduated with distinction)**
- 1997 – 2005    **School | Märkische Schule**  
Städtisches Gymnasium für Jungen und Mädchen  
**A-levels: 2,3**

### Community service

- 09/2005 – 05/2006    **German Red Cross**  
Mobile social services

**Mitteilungen aus dem Institut für Mechanik  
RUHR-UNIVERSITÄT BOCHUM  
Nr. 164**

**ISBN 978-3-935892-42-1**